Low-thrust propulsion technologies for space mission applications

Department of Mechanics, Mathematics and Management
AEROSPACE SCIENCE AND ENGINEERING
Ph.D. Program
SSD: IIND-01/G – SPACE PROPULSION

Final Dissertation

Low-Thrust Propulsion Technologies for Space Mission Applications

---

by
Elena Ancona

Supervisors:
Prof. Savino Longo
Prof. Roman Ya. Kezerashvili
Dr. Luca Vialetto

Coordinator of Ph.D. Program:
Prof. Marco D. de Tullio

Course XXXVI, 01/11/2020 - 31/10/2024

Politecnico di Bari

Department of Mechanics, Mathematics and Management
AEROSPACE SCIENCE AND ENGINEERING
Ph.D. Program
SSD: IIND-01/G – SPACE PROPULSION

Final Dissertation

Low-Thrust Propulsion Technologies for Space Mission Applications

by
Elena Ancona

Referees:

Prof. Matteo Ceriotti

Dr. Kelvin F. Long

Supervisors:

Prof. Savino Longo

Prof. Roman Ya. Kezerashvili

Dr. Luca Vialetto

Coordinator of Ph.D. Program:
Prof. Marco D. de Tullio

Course XXXVI, 01/11/2020 - 31/10/2024

POLITECNICO DI BARI

DEPARTMENT OF MECHANICS, MATHEMATICS & MANAGEMENT

Ph.D. in Aerospace Science and Engineering

SSD: IIND-01/G - Space Propulsion

Final Dissertation

Low-Thrust Propulsion Technologies for Space Mission Applications

---

by

Elena Ancona

Supervisors

Prof. Savino Longo

Prof. Roman Ya. Kezerashvili

Dr. Luca Vialetto

Coordinator of the Ph.D. Program: Prof. Marco De Tullio

Course XXXVI, 01/11/2020 - 31/10/2024

"It pays to keep an open mind,
but not so open your brains fall out"

— James Oberg,
quoted by Carl Sagan

Acknowledgements

Questa tesi è dedicata all'amicizia:
dove l'amore per gli altri diventa
amore per se stessi, e viceversa.

— ai miei amici

Ten years ago, I applied for an internship at NASA's Jet Propulsion Laboratory. In the final years of my master's degree, I had focused intensely on making my CV as compelling as possible, with each success bringing me closer to the objective. But after the initial selection process, none of the supervisors chose me, shattering that dream.

I was deeply disappointed. Yet, the people close to me encouraged me not to give up. I reached out to all my professors, asking if they had any connections at universities in the U.S. or colleagues who might help. Prof. Genta kindly agreed to chat. We talked for hours, and by the end of our conversation, he said, "I'll message a professor I know in New York."

At that moment, I had mixed emotions. On one hand, I was thrilled by the prospect of a new opportunity; on the other, I was afraid to get my hopes up only to be disappointed again.

Fast forward to today. I've just returned home, where I can finally work from the place I love most, indulging in taralli and focaccia and savoring early morning swims during a six-month-long summer in my own little corner of paradise, close to family and old friends. Over these past ten years, I've worked with several companies, taken on incredibly fulfilling roles, and lived in five different states. I've sent commands to a spacecraft orbiting Mars, supported numerous satellite launches, collaborated with talented professionals on interplanetary missions, GEO satellites, and LEO constellations, and even planned late-night maneuvers to avoid collisions in space. All of this started with a failure. Working in space operations, I've learned that failure is inevitable and contingency procedures exist for a reason. The true lesson I've gained is learning to embrace failure as an option, to expect it, and always to have a plan B.

That professor who first believed in me is now the supervisor for this thesis. Our collaboration began with six unforgettable months in New York City. I met people who have become my chosen family, and those few months shaped me in ways words can't fully express.

What am I trying to convey? What have I realized? Looking back, I think the main takeaway is that life is a sequence of events largely beyond our control. Just as in orbital mechanics, where the spheres of influence dictate movement, there are only some things we can truly change. But one thing we can always control is our response. We can take action, make choices. Life is a series of decisions, a journey filled with opportunities—not a single path, but multiple routes to reach our goals. And sometimes, those paths are difficult. The power of mobility, of embracing change, is transformative. It brings healing, fresh experiences, and the warmth of new connections.

I am profoundly grateful to Prof. Kezerashvili for his guidance over the past eight years. Roman, your passion and dedication are truly remarkable. It's been an honor to earn your trust. Thank you for believing in me, for pushing me beyond my comfort zone, for keeping my mind sharp and my curiosity alive. Thank you for leading by example and for demanding much because you give so much more. I'll stop here. Thank you.

A warm thanks to Prof. Longo. Grazie Prof, per l'energia positiva che mi hai sempre trasmesso, per la disponibilità, per farmi sentire a mio agio nei dubbi, e nell'unica consapevolezza che si fa sempre più grande dentro di me, con il tempo che passa: che ne so davvero poco, però mi piace imparare e ascoltare le persone come te, che in una serata all'osservatorio intrattengono il pubblico grazie alla forza della passione. Grazie per aver creduto in me e per aver reso questo percorso più umano con la tua simpatia.

Grazie, Luca, per l'enorme contributo con lo sviluppo del codice e le simulazioni; è stato un piacere poter lavorare con te.

Grazie alla mia famiglia. A chi c'è e mi supporta da vicino, a chi lo ha fatto e non c'è più.

Grazie a JJ. Una vita insieme, sei nel mio cuore sempre, tu e la tua zampetta sul braccio. Mi manchi moltissimo.

E grazie a tutti voi, i miei amici. A chi mi ha scritto "ce la farai", a chi mi ha portata al cinema, chi mi ha fatto la spesa, chi mi ha mandato una cartolina (incredibile, nel 2024!), chi mi ha dato una mano, in ogni modo. Mi sento fortunata e sono convinta che ognuno di voi sappia quanto sono felice di avervi nella mia vita. Penso a tutte le persone, molte delle quali sparse nel mondo, che sento vicine. Vi voglio bene.

And thank you to all my friends. To everyone who texted, "You'll make it," took me to the movies, picked up groceries for me, sent a postcard (amazing, in 2024!), or lent a helping hand in so many ways. I feel incredibly lucky, and I hope each of you knows how grateful I am to have you in my life. I think of all the people, many scattered around the world, whom I feel close to. I love you.

I recently watched an interview with Simon Sinek, where he said, "Friendship is the cure to all diseases." I am incredibly fortunate.

To friendship.

E

"Space Rocketing through Trulli"

Declarations

This thesis is submitted to the Politecnico di Bari as part of my application for the Ph.D. degree in Aerospace Science and Engineering.

Besides my own research, it contains the work from collaborative projects with my supervisors: Savino Longo (Università di Bari), Roman Ya. Kezerashvili (CUNY New York City of Technology, USA) and Luca Vialetto (Stanford University, USA).

Publications

The research work discussed in this thesis is supported by the following publications:

- E. Ancona and R. Ya. Kezerashvili, "Temperature Restrictions for Materials used in Aerospace Industry for the Near-Sun Orbits". *Acta Astronautica* **140** (2017), pp. 565–569.

- E. Ancona and R. Ya. Kezerashvili, "Extrasolar Space Exploration by a Solar Sail accelerated via Thermal Desorption of Coating", *Advances in Space Research* **63** (2019), pp. 2021–2034.

- E. Ancona, R. Ya. Kezerashvili and G. L. Matloff, "Exploring the Kuiper Belt with sun-diving solar sails", *Acta Astronautica* **160** (2019), pp. 601–605.

- E. Ancona, R. Ya. Kezerashvili and S. Longo, “Feasibility Study of a Mission to Sedna - Nuclear Propulsion and Advanced Solar Sailing Concepts”

Proceedings of 75th International Astronautical Congress (IAC2023), Milan, Italy, 14-18 October 2024. Paper *IAC-24,C4,9,6,x85994* (2024), submitted to *Aerotecnica Missili & Spazio*.

- L. Vialetto, E. Ancona and S. Longo, "A Variance Reduction Technique for Monte Carlo Simulations of Electrons and Ions in Electric and Magnetic Fields", *Physics of Plasmas* **32** (2025), pp. 013903.

- E. Ancona and R. Ya. Kezerashvili, "Recent Advances in Space Sailing Missions and Technology: Review of the 6th International Symposium on Space Sailing (ISSS 2023)", *ArXiv id:5993134 (2024)*, *Aeron Aero Open Access J.* **9**(1) (2025), pp. 62–73.

I declare that the work presented in this thesis is my own, except where otherwise indicated or acknowledged.

Elena Ancona, 2nd November 2024

Abstract

This thesis explores advanced propulsion technologies for deep space exploration, focusing on their potential to enable ambitious missions beyond the current limits of space travel. The research encompasses a broad analysis of historical advancements, contemporary developments, and future prospects in space propulsion.

Research of other planetary systems like our Solar system and stars is a century-old dream of humankind and the greatest challenge for the world scientific community. The vast interstellar distances and limited speed of modern spacecraft are the main obstacles on this path. Exploration missions targeting the Kuiper Belt, the Oort Cloud, the gravitational focal point of the Sun, and even extending to the Alpha-Centauri system represent the next frontier in space exploration. Due to the limitations of traditional methods, innovative propulsion systems are crucial to reach distant targets. Chemical propulsion, while providing high thrust for launches, suffers from low efficiency and high fuel mass requirements for long-duration missions: the *Voyager 1* spacecraft, launched in 1977, travelled with a cruise speed of 17 km/s (3.57 AU per year). Electric propulsion, including ion and Hall-effect thrusters, offers much higher efficiency and finds many applications nowadays but produces insufficient thrust for rapid deep space travel. Despite not much can be done with respect to the distances involved, some progress in science development could significantly change the situation to overcome the existing speed limitations. In this research we focus on low-thrust propulsion technologies that could fill the gap and finally make deep space missions accessible.

Chapter 1 gives an overview of deep space exploration, tracing key milestones that have shaped our understanding of the solar system and identifying promising targets for future missions. Chapter 2 provides a review of space propulsion, outlining the evolution of chemical and electric propulsion and introducing nuclear and propellantless systems as potential game-changers for deep space travel.

Chapters 3 and 4 are devoted to presenting the propulsion technologies and their characteristics. We compare and analyze two very different approaches: on one side, solar sails, the most promising propellantless system, making use of the momentum transfer provided by photons to accelerate large surfaces up to very high speeds; on the other, we dive deep into the mechanisms of the Direct Fusion Drive (DFD), a nuclear fusion engine prototyped at Princeton Plasma Propulsion Laboratory (PPPL). The DFD is based on the PPPL's Princeton Field Reversed Configuration (PFRC) machine that employs a unique plasma heating system to produce nuclear fusion power in the range of 1 to 10 MW [1]. This breakthrough technology has the potential to revolutionize space exploration and enable a whole set of new missions. The DFD could make safe and affordable mobility through the solar system a reality in the near future [2]. Near term research and development aim to move the technology of the D-^{3}He-fueled DFD rocket engine to operational status by 2030.

For both systems, we describe their main characteristics, as well as advantages and disadvantages, main challenges and most suitable missions. We also consider and address in detail all the critical technical challenges associated with both methods of interstellar travel, from the physical processes in creating jet propulsion and analyzing optimal trajectories of spacecraft to considering degradation processes in structural elements and equipment from the radiation of external and internal sources. A detailed examination of solar sail technology is presented in Chapter 3, from fundamental concepts to state-of-the-art advancements. The study highlights

recent innovations in materials, deployment mechanisms, and alternative thrust-enhancement methods such as thermal desorption. On the other hand, Chapter 4 introduces the DFD, a fusion-based propulsion concept that promises high efficiency and extended mission capabilities. The research delves into the fundamental principles of DFD, exploring its applications, advantages, and technical challenges.

For the DFD, particle kinetics and transport in scenarios relevant to the nuclear fusion propulsion engine are investigated. Chapter 5 focuses on particle transport processes essential to DFD operation. Advanced Monte Carlo (MC) simulation techniques, including the Monte Carlo Flux (MCF) method, are employed to model electron and ion transport within the DFD environment. These simulations provide insights into transport phenomena and validate the applicability of MCF in complex plasma scenarios. This includes the development of tailored simulation methods to analyze the behavior of charged particles in hydrogen and deuterium, which are relevant for the design of propulsion systems based on thermonuclear fusion reactions. After running some initial MC simulations of electrons in an ideal gas model, validated against analytical solutions, an additional technique is used for variance reduction of MC simulations, to quicken the calculations: the MCF method. The MCF provides a partition of the velocity space to describe the free electrons' kinetics by means of a probability balance equation, in which the transition frequencies are calculated with a large number of short-time Monte Carlo simulations. This method provides a reduction of the computational time up to a factor of 100 compared to conventional MC simulations. Detailed and accurate databases of cross-sections of elementary processes for electrons in molecular deuterium gas are used. The effects of combined electric and magnetic fields on the electron distribution function are also investigated. The analysis is extended to study ion transport in gases under the effect of electric and magnetic fields. The thesis presents the first application of MCF to H^+ ions in H_2 gas. The results shared are of relevant interest for primary systems support technologies, in particular for

ion sources and for plasma diagnostics in fusion reactor prototypes.

Regarding the solar sail, we explore the potential of an innovative solution to enhance its conventional performance: coating the membrane with heat-sensitive materials that undergo thermal desorption, providing additional acceleration alongside the standard propulsion from solar electromagnetic radiation [3, 4, 5]. The concept is quantitatively detailed using chemical-physical considerations, providing a model that can be integrated into a mission scenario. This is further elaborated in Chapter 6 where the contribution of thermal desorption is shown and it results in a velocity gain of hundreds of km/s for sail deployed at heliocentric distances of about 0.1 AU.

Chapter 6 focuses on mission analysis and design. It examines achievable low-thrust missions using the DFD and a solar sail enhanced by coating material desorption for acceleration, targeting the outer solar system and beyond. An analysis of these missions is provided, including payload delivery capabilities and mission duration. Results and concluding remarks are presented to finalize the analysis. The findings contribute to the broader discourse on space propulsion, providing a framework for selecting optimal propulsion strategies based on mission requirements.

By integrating theoretical models, computational simulations, and mission analysis, this thesis advances the understanding of emerging propulsion technologies and their role in future deep-space exploration.

Nomenclature

Physical Constants

σ_{SB}	Stefan-Boltzmann constant, 5.67×10^{-8} W/m^2·K^4
c	speed of light, 3×10^8 m/s
G	universal gravitational constant, 6.674×10^{-11} m^3/kg·s^2
g_0	standard gravitational acceleration, 9.81 m/s^2
h_P	Planck's constant, 6.626×10^{-34} J·s
k_B	Boltzmann constant, 1.38×10^{-23} J/K
L_S	solar luminosity, 3.828×10^{26} W
M_S	mass of the Sun, 1.989×10^{30} kg
R	universal gas constant, 8.314 J/mol·K
R_E	Sun-Earth distance (1 AU), 1.496×10^{11} m
e	elementary charge, 1.602×10^{-19} C
m_e	electron mass, 9.109×10^{-31} kg

Generic symbols

β	sail lightness number (Ch.3) / Hall parameter (Ch.5)

Δm difference in mass between initial and final states

Δt time interval

$\dot{m}_p$ mass flow rate of propellant

η efficiency parameter

$\mathbf{p}$ momentum vector

$\mathbf{r}$ position vector

$\mathbf{v}$ velocity vector

ν frequency

ϕ energy flux / solar irradiance

ψ flux / angular flux (transport theory)

σ sail loading factor (Ch.3) / cross-sectional area for collisions (Ch.5)

A area

B magnetic field

D areal density

E energy but also electric field intensity

m mass

p momentum

Space Propulsion and Sails

$\mathbf{e}'_r$ unit vector directed as the reflected radiation

$\mathbf{e}_r$ unit vector directed as the incident radiation

$\mathbf{e}_t$ unit vector tangent to the trajectory

$\mathbf{n}$ solar sail normal vector

R_h heating rate

$\mathfrak{a}$ semimajor axis

a acceleration

a_0 characteristic acceleration

a_D acceleration due to desorption

a_P acceleration due to photon pressure

E_A activation energy

E_g specific mechanical energy

$\mathbf{F}$ force

H sail thickness

H_c sail coating thickness

I_{sp} specific impulse

λ wavelength

M_c coating mass of the desorption

m_{pl} payload mass

m_s sail mass

N total number of particles

N_A surface concentration of adsorbed species

$\mathfrak{p}$ probability distribution

P solar radiation pressure

P_{sail} total pressure acting on sail

q kinetic order of desorption

R_d rate of desorption

ρ reflectivity

$\mathcal{T}$ temperature

$\mathcal{T}_{md}$ temperature for maximum desorption

T thrust

t_{sr} surface residence time

ϑ angle of incidence, sail pitch angle

$\overline{v}$ mean speed

v_c circular velocity

v_{esc} escape velocity

v_e exhaust velocity

v_{th} thermal speed

W power

ζ emissivity

Nuclear Propulsion and DFD

Q energy released in fusion reaction

B/n_g reduced magnetic field (magnetic field to gas density)

E/n_g reduced electric field (electric field to gas density)

ϵ electron kinetic energy

$\boldsymbol{f}(t)$ velocity distribution function at time t

$\boldsymbol{M}(\Delta t)$ transport matrix for time step Δt

Ω solid angle in momentum space

τ_α reaction rate per unit volume

ϕ azimuthal angle in cylindrical coordinates

ψ flux in transport theory

Σ macroscopic cross section

θ angle between velocity and z-direction

List of Figures

List of Tables

Contents

Introduction

Context and Background

The exploration of deep space has long been driven by humanity's quest to understand our place in the universe and to uncover the potential for life beyond Earth. Studying distant planetary systems, stars, and regions within our own solar system, such as the Kuiper Belt and Oort Cloud, offers unique opportunities to learn about planetary formation, the evolution of solar systems, and the broader mechanics of the cosmos. Each mission beyond the familiar confines of the inner solar system provides invaluable data on the behavior of celestial bodies and the interactions within interstellar space, enhancing our understanding of astrophysical processes. Moreover, with the discovery of exoplanets and potentially habitable environments around distant stars, the scientific community is increasingly motivated to explore these frontiers for signs of extraterrestrial life and conditions suitable for future human exploration or habitation.

In addition to the fundamental knowledge gained, the technological and scientific advancements required for deep space exploration often have applications that benefit life on Earth, such as advancements in materials science, energy systems, and artificial intelligence. However, one of the most significant obstacles in reaching distant celestial targets is the vast distances involved. The closest star system, Alpha Centauri, lies approximately 4.37 light-years away, a distance that is currently insurmountable with conventional propulsion methods. Even within

our solar system, targets like the Kuiper Belt and Oort Cloud require years or even decades of travel with traditional propulsion systems. Therefore, there is a pressing need for breakthroughs in propulsion technology that can sustain higher speeds over extended periods, making such missions feasible within a human lifetime.

Conventional propulsion systems face significant limitations when it comes to interstellar travel and even prolonged solar system exploration. Chemical propulsion, which is the foundation of most current space missions, operates by expelling propellant at high velocity to produce thrust. While this method generates considerable thrust, it is highly inefficient for long-duration missions because it requires an impractical amount of fuel to sustain acceleration over vast distances. For instance, *Voyager 1*, launched in 1977, relies on chemical propulsion and travels at a cruise speed of 17 km/s (3.57 AU per year), which is insufficient for rapid interstellar exploration. Chemical propulsion systems are particularly unsuited for deep space missions due to their high fuel mass requirements and the associated cost and logistical challenges of carrying such quantities on spacecraft.

Electric propulsion systems, such as ion and Hall-effect thrusters, offer a more efficient alternative by using electric fields to accelerate ions, which produces a gentler but continuous thrust. This approach is widely used in modern space missions for tasks such as orbital adjustments and prolonged station-keeping. However, while electric propulsion can sustain a mission for a longer period, its thrust levels are relatively low, making it insufficient for reaching high speeds needed for interstellar distances within a practical timeframe. For deep space missions, the speed limitations of electric propulsion still mean that targets like the Kuiper Belt and Oort Cloud remain challenging to reach in reasonable mission durations. As a result, there is a significant gap between the propulsion capabilities of current systems and the requirements of interstellar exploration, highlighting the urgent need for innovative solutions that can provide sustained, high-velocity propulsion. This research focuses on addressing these challenges by investigating advanced, low-thrust

propulsion systems that could potentially overcome the limitations of traditional methods and make deep space exploration more accessible.

Purpose of Research

This research addresses the need for advanced, low-thrust propulsion technologies capable of supporting deep space exploration. It compares two promising, innovative approaches: the solar sail and the Direct Fusion Drive (DFD). Solar sails, which operate without fuel by harnessing momentum from photons, offer a potential solution for long-duration missions by achieving high speeds with large sail surfaces. The DFD, on the other hand, represents a breakthrough in nuclear fusion propulsion. Developed at the Princeton Plasma Propulsion Laboratory, the DFD uses the Princeton Field Reversed Configuration (PFRC) for plasma heating to achieve controlled nuclear fusion, generating thrust with power levels of 1 to 10 MW. This research investigates the capabilities, technical challenges, and mission suitability of both systems, highlighting their advantages and limitations in the context of interstellar and deep space missions. Through comprehensive analysis, the study seeks to assess how both technologies could make deep space missions more feasible, offering valid alternatives depending on the mission objectives and constraints.

Thesis Structure Overview

This thesis is organized to systematically explore the foundations, advancements, and mission applications of two innovative propulsion technologies: solar sails and the DFD, with a focus on enabling deep space exploration.

The introductory chapter discusses the motivations for deep space exploration and the scientific interest in potential destinations like icy moons, as well as the

Kuiper Belt, Oort Cloud, and Alpha Centauri. Chapter 2 provides a broad overview of space propulsion, tracing its evolution from chemical and electric propulsion to the development of nuclear and propellantless systems, highlighting the limitations of conventional methods and the need for breakthroughs in propulsion technology. Chapter 3 then focuses specifically on solar sail technology, covering its conceptual foundations, initial studies, and recent innovations such as thermal desorption coatings, which enhance propulsion efficiency. This chapter also outlines the state of the art in solar sail development, existing challenges, and promising applications for interstellar travel.

Chapter 4 introduces the DFD, a pioneering fusion-based propulsion system developed at Princeton Plasma Propulsion Laboratory. The chapter examines the DFD's design and operating principles, emphasizing its potential to provide sustainable, high-powered thrust suitable for extended missions within and beyond our solar system. It explores the main advantages of the DFD, possible mission applications, and technical challenges, setting the context for the detailed particle transport studies that follow.

Chapter 5 delves into particle transport processes, which are essential for the effective operation of the DFD. This chapter provides an overview of transport methodologies, focusing on the Monte Carlo (MC) and Monte Carlo Flux (MCF) methods as tools to model particle behavior and optimize system performance. Simulation results, including applications to electron and ion transport in magnetized environments, are presented to illustrate the behavior of particles within the DFD and the implications for propulsion efficiency.

Chapter 6 presents a mission analysis and design study, examining scenarios for low-thrust missions using both solar sails and the DFD. It begins with an overview of proposed mission concepts in the literature, followed by detailed simulation results for both propulsion methods, evaluating mission feasibility, payload capacity, and duration. This chapter concludes with a comparative analysis, synthesizing

findings to identify the strengths and limitations of each technology for various mission profiles.

The thesis concludes with a summary of findings, implications for future space exploration, and recommendations for further research to enhance these propulsion systems for practical interstellar missions.

Chapter 1

Deep Space Exploration

This chapter provides an overview of deep space exploration, beginning with key milestones and achievements that have expanded our understanding of the solar system and beyond. It then identifies promising targets for future missions, exploring scientifically rich destinations such as the icy moons Enceladus and Europa, the Kuiper Belt region, and the distant trans-Neptunian object Sedna. The chapter also discusses the potential of exploring the Oort Cloud and the nearby Alpha Centauri system, highlighting these targets as the next frontiers in the pursuit of uncovering the mysteries of deep space. Finally, some of the main challenges for deep space missions are presented.

Deep space exploration has dramatically expanded our understanding of the solar system and beyond, thanks to a series of groundbreaking missions over the past few decades. From the journeys of *Pioneer* [6] and *Voyager* [7] to planned missions targeting Europa and Titan, these efforts mark significant milestones in the quest to explore our cosmic neighborhood. This section provides an overview of successful deep space missions and outlines upcoming missions that promise to push the frontiers of space exploration even further.

1.1 Milestones and Achievements

The first successful deep space missions were *Pioneer 10* and *Pioneer 11*, launched in 1972 and 1973, respectively. Both spacecraft traversed the asteroid belt and provided the first direct observations of Jupiter and Saturn before setting out on trajectories that would eventually lead them beyond the solar system. Originally designed for a 21-month mission to fly by Jupiter, *Pioneer 10* operated for over 30 years, sending its final signal to Earth in January 2003 from a distance of more than 12 billion km. *Pioneer 11*, which was the first spacecraft to study Saturn up close, last communicated with NASA's Ames Research Center in 1995.

In 1977, *Voyager 1* and *Voyager 2* began their journeys, capturing detailed data on the outer planets. *Voyager 1* became the first human-made object to reach interstellar space in 2012, with *Voyager 2* following in 2018 [8]. As of Aug. 21, 2024, *Voyager 1* - the farthest object in space created by humans - was at more than 164 AU from Earth travelling at 17 km/s relative to the Sun.

Later missions focused on specific regions within the solar system. *New Horizons*, launched in 2006, achieved a historic flyby of Pluto in 2015, delivering detailed images of the dwarf planet's surface [9]. After its Pluto encounter, *New Horizons* continued into the Kuiper Belt, where it explored the object Arrokoth (formerly 2014 MU69) in 2019 [10]. The *Cassini-Huygens* mission, launched in 1997, spent over a decade studying Saturn and its moons [11, 12]. Notably, the *Huygens* probe performed the first landing on Titan, Saturn's largest moon. *Juno*, launched in 2011, provided detailed observations of Jupiter, offering insights into the planet's internal structure and magnetic field [13]. The *Rosetta* mission from the European Space Agency (ESA) was another landmark mission, successfully orbiting and landing a probe, *Philae*, on the comet 67P/Churyumov–Gerasimenko, which enabled unprecedented studies of comet composition [14]. After launching in 2004 and encountering the comet a decade later, the *Rosetta* mission concluded with a

successful, controlled impact on the comet on September 30, 2016 [15]. At that moment, the author of this thesis had just joined the Interplanetary Missions Division at the European Space Operations Center (ESOC), and the memory of that day remains vivid.

1.2 Promising Targets for Future Missions

Since the inception of space exploration, celestial bodies such as the Moon, Mars, Venus, and Jupiter have attracted significant interest due to their accessibility, size, and Earth-like characteristics. However, as technology advances, there has been a growing fascination with more distant objects like comets, asteroids, and icy moons, driven by the ongoing pursuit of understanding planetary formation and the potential for extraterrestrial life. Building on the successes mentioned in the previous section, several upcoming endeavors are set to expand upon this legacy.

The *Europa Clipper* mission, just launched on Oct. 14, 2024 - a few weeks before the time of writing this thesis -, will explore Jupiter's icy moon Europa, which is believed to have a subsurface ocean that might be conducive to life [16]. *Dragonfly*, set for a 2027 launch, will be the first rotorcraft to land on Titan, where it will analyze surface composition and atmospheric conditions, focusing on Titan's methane lakes [17]. ESA's *Jupiter Icy Moons Explorer (JUICE)*, launched in 2023 and arriving at Jupiter in 2031, is designed to investigate the habitability of Jupiter's icy moons, including Ganymede, Callisto, and Europa [18].

NASA's planned *Interstellar Probe* (ISP) concept aims to reach the interstellar medium, potentially launching in the late 2030s, to study the environment beyond the influence of the solar wind [19]. Ralph McNutt, the chief scientist for space science at the Johns Hopkins University Applied Physics Laboratory, is among several experts who passionately support the mission, potentially set to launch in 2036. The probe would embark on a direct hyperbolic trajectory to reach Jupiter

in approximately six to seven months. Following this encounter, it will travel at a speed of about 6 to 7 AU per year, exiting the heliosphere in just 16 years. If the mission is approved, it will continue the exploration of the galaxy initiated by the Voyager mission in 1977 [20].

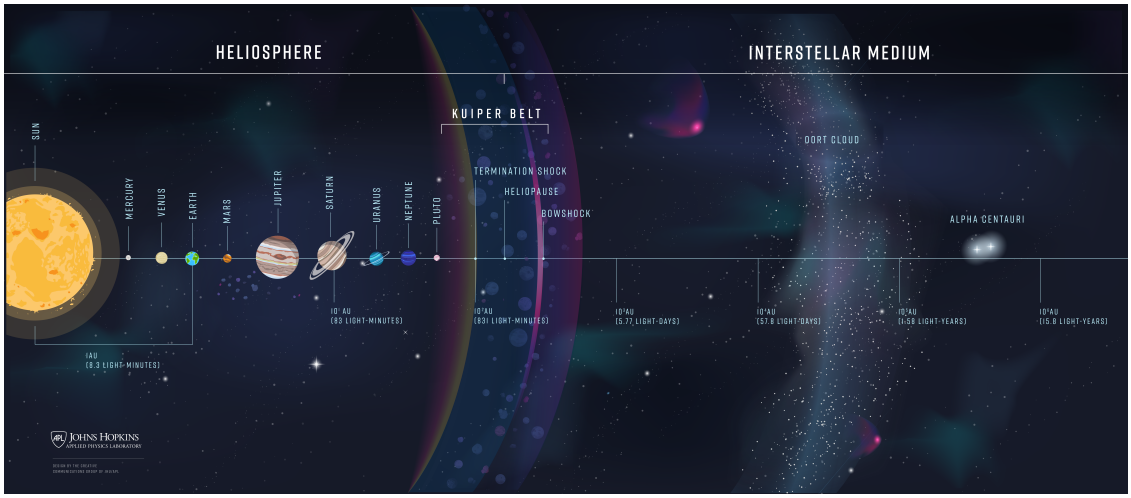

Figure 1.1: The Interstellar Medium. Credit: Johns Hopkins APL.

In addition to the proposals discussed, this thesis focuses specifically on deep space exploration, particularly targeting regions in the outer solar system. The scientific curiosity driving intensified research in these distant areas is closely linked to recent developments in astrobiology and studies on the origin of life. While Mars remains a highly intriguing environment with the potential for unexpected discoveries, there has been a growing consensus in recent years that the most promising exo-environments for studying the origins of life are cold, water-rich bodies rich in organic molecules, situated far from the Sun [21, 22]. At the same time, advances in direct imaging and spectral analysis of exoplanets are revealing a diversity of environments that show considerable potential for exobiological and astrobiological studies — offering possibilities far beyond what our solar system alone could provide. The scientific community is calling for exploration of new destinations such as the Kuiper Belt, the Oort Cloud, the gravitational focal point of the Sun, and even the Alpha Centauri system, marking the next frontier in space exploration.

Each of these targets presents unique scientific motivations, and below, we outline the primary drivers behind this renewed interest in these diverse bodies.

Enceladus and Europa Enceladus and Europa are icy satellites, that is, fundamentally rocky bodies but with an external layer made up of water which in their external part is necessarily in its solid phase [23]. The first aspect of astrobiological interest is the large amount of complex organic matter, found on the ice surfaces of these bodies in the form of Tholins, nitrogen-rich polymers normally with a deep red colour, evidently formed spontaneously from monomers with the activating energy provided by ultraviolet light from the sun. Another aspect that has emerged in recent years is the presence, now certain in both cases, of a vast and deep ocean of liquid water beneath the icy crust: the water is kept liquid by the effect of the pressure of the solid ice and by the thermal energy coming from the important tidal effects due in turn to the orbits of these bodies around giant planets. The prospect of such an extended environment, potentially a biosphere, is extremely interesting and can lead to essential conclusions about the nature of the original processes of life and their probability: this is true both in the case that current forms of life exist and are found in these oceans of liquid water and in the case that they are not found.

The Kuiper Belt Region The Kuiper Belt region and beyond - extending from Neptune's orbit to the Sun's gravitational focus at approximately 550 AU - presents compelling scientific interest, particularly in the outermost reaches of the heliosphere [21, 22]. Objects in the distant Kuiper Belt, exposed to minimal solar radiation, hold unique astrochemical and prebiotic significance. Recent findings, such as the discovery of complex chemical interactions on Pluto's surface by the *New Horizons* mission, underscore this interest. Unlike the highly altered bodies in the inner solar system, these distant objects likely reflect chemistry shaped by origins in the interstellar medium, offering a relatively pristine record of materials

and processes from the broader interstellar environment.

The TNO Sedna Among potential destinations, there's a growing focus within the scientific community on the trans-Neptunian object (TNO) Sedna (90377). With its highly eccentric orbit around the Sun, Sedna is currently approaching its perihelion at around 76 AU, offering an exceptional opportunity for deep space exploration. Its aphelion, situated approximately 936 AU away, makes Sedna an intriguing target for further study. Together with Saturn's moon Enceladus [24] and Jupiter's moon Europa [25], Sedna, in the inner Oort Cloud, is considered one of the most promising destinations for several reasons. Sedna's orbit takes it far beyond the Kuiper Belt, with its perihelion at around 76 AU and its aphelion at nearly 936 AU (31 times farther than Neptune's aphelion). Sedna could provide the first direct observations of this distant and unexplored region, which is crucial for understanding the outer solar system and its boundaries. Its highly elongated orbit takes it well beyond the heliopause, the boundary beyond which the influence of the Sun is negligible with respect to that of the particles from interstellar space. This would have allowed Sedna to interact differently with other elements that could offer clues about the early history of the solar system, particularly the processes that shaped the orbits of such distant objects. Moreover, the fact that Sedna spends so little time in the proximity of the Sun, protects its surface from solar radiation and heat. In fact, spectroscopic observations suggest that it could contain organic compounds, water ice, and possibly methane ice. Analysing its composition could reveal much about the original "building blocks" of planets and other bodies. In particular, detailed analysis of any organic matter present on the surface of Sedna could provide specific information about the role of photochemical processes in the synthesis of organic matter versus alternative processes induced by fast electrons or other causes. This information, complementary to that which can be obtained from the analysis of Tholins for example on Europa or Titan, where photochemical

processes are certainly more relevant, is of extreme interest in the current debate regarding the primary chemical reactions at the origin of life [23, 26]. In summary, a mission to Sedna offers the opportunity to study a pristine, distant object that could shed light on the solar system's formation, the early history of planetary orbits, and the nature of the farthest reaches of our cosmic neighbourhood.

The Oort Cloud The Oort cloud is a region of distances ranging from 2,000 to 200,000 AU. A mission to this area of interstellar space has not yet been carried out, and we would be able to obtain new results suitable for the preliminary design of new spacecraft. As is well known, the Oort cloud is the material source of long-period comets, objects that take more than 200 years to orbit the sun. The probable consistency of this belt is over a trillion objects made of ice-covered rock. This material is in many ways more representative of the interstellar medium (ISM) than of the solar system, and represents a treasure trove of primordial chemistry only slightly influenced by the Sun. Its direct chemical analysis could provide first-hand information on the chemistry of deep space. Because it is volatile, direct access is not comparable to the analysis of cometary material that nevertheless derives from this environment. There is also interest in learning much more about the chemistry of carbon, polycyclic aromatic hydrocarbons (PAHs), graphite, graphene, fullerites, in contact with solid water in these systems, for a better understanding of the origin of the mid-infrared opacity of the ISM.

Alpha Centauri System The Alpha-Proxima Centauri system is evidently the most accessible among the exo-systems properly speaking. Reaching it corresponds to a leap in the distance scale of a thousand to ten thousand times compared to those considered in the previous cases, and it is therefore a mission scenario that is at the very least extreme. On the other hand, it is evident that sooner or later we will have to consider the prospect of being able to directly access the chemistry and the potential biochemistry, perhaps primordial, of an authentic system of exoplanets,

of its minor bodies and of its interplanetary medium. Several exoplanets have already been identified for this system. It also presents a great peculiarity given that it is a double system, triple with Proxima. Furthermore, while both stars in the Alpha Centauri double system are main-sequence stars, Proxima is a red dwarf, a type of object that has recently been studied for its intrinsic characteristics as an energy source for the possibility of extraterrestrial life. Numerous studies in the past have considered the possibility of an origin of life on planets that orbit in binary star systems and there are different types of long-term orbital stability that have been classified, respectively P-type and S-type: they lead to significantly different astrobiological scenarios. All this is obviously without confirmation in the case of the solar system and the prospects and results that can come from a direct exploration of this system can be of the utmost interest. The ambitious *Breakthrough Starshot* project aims to demonstrate proof of concept for ultra-fast light-driven nanocrafts, and lay the foundations for a first mission to Alpha Centauri within the next generation [27, 28, 29, 30].

1.3 Main Challenges in Deep Space Exploration

Designing a deep space mission presents substantial difficulties related to the extreme distance involved, long mission duration, limited propulsion and energy options, and complex navigation required. In this study, we focus on the propulsion system aspects and evaluate options to drastically reduce the time required to reach such a distant target, however when assessing the feasibility of a mission the following challenges must be also taken into account:

- Communication Delays: as an example, the one-way-light-time (OWLT) for a spacecraft near Sedna would be up to 13 hours at its farthest point from the Sun; for comparison, the OWLT for us to communicate with a satellite orbiting Mars is around 20 minutes. Such a delay would completely exclude the

possibility of operating the spacecraft in real-time. Communication systems would need to be designed to handle long delays and autonomous systems would be required to execute maneuvers, data collection, and problem-solving with minimal input from Earth.

- Navigation and Course Corrections: navigating to a distant and moving target is highly complex. Given the vast distances, small errors in trajectory can result in large deviations by the time the spacecraft reaches the body. If the mission concept is taking advantage of gravity assists from other planets, the effect of those has to be carefully evaluated and corrected to adjust the spacecraft's trajectory on the way.

- Timing Constraints: when targeting closer objects with orbits similar to Earth's, for a missed launch window opportunity a new one can be identified within months or, in the worst case, a few years. This is clearly not the case for other bodies: considering again Sedna, its highly elliptical orbit brings it relatively "close" to the Sun (and thus, us) for a small portion of its 11400 years orbit period.

In July 2024, the University of Oxford's Physics Department hosted the Breakthrough Discuss Conference, with the theme "A Cosmic Tapestry for Exploration: Weaving Novel Threads in Artificial Intelligence, Astrobiology, and Space Missions" [31]. The conference gathered scientists and researchers from around the world to discuss the transformative role of artificial intelligence (AI) in data science, which is fundamentally reshaping the design and conceptualization of space missions [32], addressing some of those concerns mentioned above. The roadmap for space applications is clear: the ultimate goal is for satellites to manage the majority of tasks autonomously. Achieving this level of autonomy, however, will require the completion of several intermediate milestones. Various organizations, industries, and space agencies are actively working toward this objective [33]. For example,

projects like CAPSTONE are advancing technologies that allow spacecraft to autonomously perform optimal maneuvers, ensuring both reliability and operational integrity, even in challenging regions like cislunar space [34].

Advances in AI and Machine Learning (ML) are poised to greatly expand the potential of future space missions. Autonomous science agents, for instance, are being developed to allow onboard systems to independently analyze samples, update scientific priorities in real time, and manage data collection without continuous ground-based communication [35]. This capability is especially valuable for planetary missions where communication may be limited or delayed. AI and ML integration will not only reduce reliance on ground control but also unlock new possibilities for exploring distant, hard-to-reach celestial bodies. Such technologies have been identified as crucial for upcoming planned missions to Uranus or Enceladus, enabling precise maneuver planning and execution in challenging environments [36].

In addition to these advancements, other constraints will need to be addressed. Scientific payloads must be carefully selected to ensure onboard instruments are reliable and capable of operating in cold, dark regions far from the Sun. A deep space spacecraft also needs to navigate hazardous areas of space, with elevated risks from cosmic rays and micrometeoroids, necessitating proper shielding to protect against impacts and radiation exposure. These are just a few of the major challenges that such missions would face. This work focuses on propulsion technologies and mission concepts; however, the aim of this section was to highlight that any proposed solutions would require design-phase iterations to effectively overcome these obstacles.

Chapter 2

Space Propulsion: an Overview

This chapter presents a brief overview of space propulsion, tracing its development from early technologies to modern innovations. It begins by exploring the history of chemical and electric propulsion, foundational methods that have enabled space exploration. Recognizing the need for advanced concepts, the chapter introduces nuclear propulsion and propellantless systems, which promise greater efficiency for deep space missions. Following a review of current research and emerging technologies, the chapter concludes with final observations on the future of space propulsion and the ongoing quest for efficient - and possibly sustainable - space travel solutions.

2.1 Early Technologies and Recent Advances

Early space propulsion technologies trace their roots to the late 19th and early 20th centuries when scientists and visionaries began to imagine and experiment with the means to reach beyond Earth's atmosphere. Konstantin Tsiolkovsky, the Russian scientist often regarded as the "father of astronautics," made foundational contributions to rocket science in the early 1900s. His groundbreaking work, including the Tsiolkovsky rocket equation (see section 2.1.2), outlined the principles for reaching space with multi-stage rockets.

The advent of World War II accelerated rocketry research due to their relevance also for military applications. In 1944, Germany's *V-2* rocket, developed by Wernher von Braun and his team, became the first human-made object to reach the so called "edge of space", crossing the Karman line. Afterwards, the Cold War competition between the United States and the Soviet Union fostered further advances in space propulsion, setting the stage for the Space Race.

In 1957, the Soviet Union launched *Sputnik 1*, the world's first artificial satellite, a milestone that demonstrated the potential of rocket-based propulsion for space exploration. This achievement led to the rapid development of space programs in both countries. By 1961, Yuri Gagarin, aboard the *Vostok 1*, became the first human to orbit Earth. In the United States, the subsequent Apollo program marked significant advancements in propulsion, with the *Saturn V* rocket, designed by von Braun, carrying astronauts to the Moon in 1969.

Technological evolution continued throughout the 20th century, with both superpowers developing increasingly sophisticated propulsion systems, leading to innovations like liquid hydrogen-fueled engines and solid-propellant boosters. Today, space propulsion remains a dynamic field, with ongoing research into nuclear thermal propulsion, ion thrusters, and other cutting-edge technologies for interplanetary exploration. The shift from traditional, government-led space programs to the "New Space" economy is marked by the significant involvement of private companies, driven by the demand for commercial and sustainable access to space. This new model is led by companies like SpaceX and Blue Origin which have developed cost-effective launch solutions, reusable rockets, and advanced spacecraft. SpaceX, in particular, has achieved major milestones, including the first privately developed craft to dock with the International Space Station (*Dragon, 2012*) and the *Falcon Heavy*'s launch in 2018, the most powerful rocket in operation. On October 13, 2024, SpaceX made history (again), catching the *Starship's Super Heavy* booster with "chopstick" arms of the launch tower. SpaceX's *Starship* project aims to

make Mars exploration possible, representing a groundbreaking step in deep-space exploration and commercialization.

2.1.1 Fundamentals: Thrust and the Rocket Equation

Equation (2.1) links the thrust T [N] to the mass flow rate of the propellant, $\dot{m}_p$ [kg/s], through the gas exhaust velocity v_e [m/s]. The specific impulse I_{sp} [s] is a measure of a rocket engine's efficiency: it represents the momentum change per unit weight of propellant and it's defined as the ratio of the exhaust velocity v_e to standard gravity g_0 (9.81 m/s^2):

$$T = \dot{m}_p \; v_e = \frac{\Delta m}{\Delta t} \; I_{sp} \; g_0. \tag{2.1}$$

Higher specific impulse indicates a more efficient engine, requiring less propellant for the same thrust. The equation can be understood as follows: thrust T is produced by expelling propellant at a mass flow rate $\dot{m}_p$ with exhaust velocity v_e. Alternatively, it can be expressed in terms of specific impulse I_{sp}, showing that thrust depends on both the rate of mass ejection and the efficiency of the rocket engine.

Starting from Newton's law of motion and Eq. 2.1, the change in velocity Δv [m/s] can be written as the integration over time of the magnitude of the acceleration produced:

$$\Delta v = \int_{t_i}^{t_f} \frac{T}{m}\, dt \; = \int_{t_i}^{t_f} \frac{\dot{m}_p \; v_e}{m}\, dt \; = -\int_{m_i}^{m_f} \frac{v_e}{m}\, dm \; = v_e \ln\left(\frac{m_i}{m_f}\right), \tag{2.2}$$

where m_i is the initial mass of the rocket, including the propellant mass m_p. The final mass m_f, after the propellant has been expended, is also referred to as "dry", whereas m_i is known as "wet" mass. This is the Tsiolkovsky Equation, also known as the Rocket Equation, which relates the change in velocity of a rocket to the

effective exhaust velocity of its propellant and the initial and final masses of the rocket. Eq. (2.2) can be rewritten as:

$$m_i = m_f e^{\Delta v / v_e}. \tag{2.3}$$

This equation is crucial for understanding the requirements of orbital mechanics, launch vehicles, and space mission design. As the initial mass is given by the dry mass and the propellant mass ($m_i = m_f + m_p$), Eq. (2.3) shows that - given the effective exhaust velocity (determined by the rocket motor's design), a target Δv, and the desired dry mass to put into orbit as input - the required propellant mass grows exponentially with the desired change in velocity.

2.1.2 Chemical Propulsion

The journey into space began when chemical propulsion (CP) became a viable technology. High-energy gas is produced through the reaction of a fuel and an oxidizer, which is then expelled through a nozzle to generate thrust. The thrust equation for a rocket describes the force T generated by the expulsion of mass at high velocity, allowing the rocket to propel itself forward. CP can use either solid or liquid propellants. Solid rocket motors use a single, pre-mixed propellant that burns upon ignition. Liquid rocket engines, by contrast, use separate tanks for the fuel and oxidizer, which mix and ignite in the combustion chamber. Each method has its advantages, and they can also be combined, as in the famous case of the *Space Shuttle*'s propulsion system that relied on a combination of a liquid-fueled main engine and two Solid Rocket Boosters (SRBs). The SRBs together provided 80% of the thrust during the first two minutes of flight; they operated alongside the main engines, which were fueled by the external tank (ET) containing liquid hydrogen and liquid oxygen. After two minutes, the SRBs were jettisoned, while the main engines continued to propel the shuttle toward orbit.

The key advantage of chemical propulsion is its high thrust (from several kN to over 1,000 kN), making it ideal for launch and achieving initial orbit insertion. This high thrust capability enables rapid acceleration, which is necessary to overcome Earth's gravity. Furthermore, chemical propulsion is a mature technology with decades of research and development, leading to a well-understood design and operational framework. However, chemical propulsion systems have limitations, primarily in their low specific impulse, which makes them less suitable for long-duration missions. They also require large amounts of fuel, contributing significantly to the spacecraft's launch mass, which can be a constraint on payload capacity. This limitation is highlighted by the Tsiolkovsky Equation, Eq. 2.2.

The I_{sp} of chemical propulsion is limited by the energy of chemical reactions, which bounds the maximum exhaust velocity achievable. For liquid bipropellant rockets, such as those using liquid oxygen and hydrogen, the specific impulse can reach around 450 s. Solid rockets typically reach lower values, around 250–300 s.

Staging is an effective workaround to overcome this limitation by addressing the exponential nature of the rocket equation. In a staged rocket, parts of the rocket (stages) are discarded sequentially as fuel is depleted, thus effectively reducing the mass of the rocket. By dropping empty tanks and engines, the remaining stages can accelerate more efficiently the rocket.

2.1.3 Electric Propulsion

For a long time, chemical thrusters were the only solution granting access to space, given the high thrust required by launches and initial orbit insertion. As research advanced in the field, though, different technologies were enabled. Electric propulsion (EP) represents a more efficient method of generating thrust in space, thanks to the high specific impulse that allows for long-duration missions and high flexibility with maneuvering. Common types of EP systems are ion thrusters and Hall-effect thrusters. The first electric propulsion test was in 1964 with the Soviet

Zond 1 and later with *Zond 2*, which used pulsed plasma thrusters for attitude control. NASA's *SERT-1* mission in July 1964 demonstrated a successful ion engine for about 30 minutes, followed by *SERT-2* in 1970 with thrusters operating for months. Though *Project Daedalus* explored nuclear-powered electric propulsion in 1973, it was deemed impractical due to low acceleration and heavy equipment. By the 2010s, EP became common for satellite attitude control and even orbit insertion. Some applications, like Hall-effect thrusters, have already been extensively used in space [37, 38, 39, 40, 41] and are nowadays firmly established technologies adopted by all sorts of missions [42]. Constellations like *OneWeb* and *Starlink* rely on EP thruster for all mission phases, from orbit raising to collision avoidance and station keeping maneuvers [43].

Through Tsiolkovsky's equation, the advantage in terms of propellant savings, when comparing EP to CP, is evident. This is due to an increase of an order of magnitude in the typical values of I_{sp} for EP, ranging from 1,000 to 10,000 s.

2.2 The Need for Innovative Propulsion Concepts

Due to the limitations of traditional methods, innovative propulsion systems are crucial to reach distant targets like those suggested in section 1.2 [44]. CP, while providing high thrust for launches, suffers from low efficiency and high fuel mass requirements for long-duration missions: the *Voyager 1* cruise speed of about 3 AU per year is clearly not sufficient for deep space exploration. EP offers much higher efficiency and finds many applications nowadays [42] but produces insufficient thrust (from mN to a few N) for rapid deep-space travel. NASA's ion-thrusters-equipped Dawn spacecraft, which explored the asteroid belt, highlighted the advantages of electric propulsion for deep-space maneuvers [45], however both Vesta and Ceres were relatively close (1.14 AU and 2.87 AU) when reached by Dawn in 2011 and 2015 respectively. It is evident that novel space propulsion mechanisms are essential

for enabling faster and more energy-efficient exploration of the outer solar system and beyond. In the book *Interstellar Travel* Matloff and Gerrish discuss physical challenges of interstellar flight from a propulsion and energy point of view [46]. Fig. 2.1 shows the significant influence of the I_{sp} on the feasibility of various missions (defined through the required Δv). New technologies are necessary to accomplish those objectives with more reasonable amounts of propellant mass.

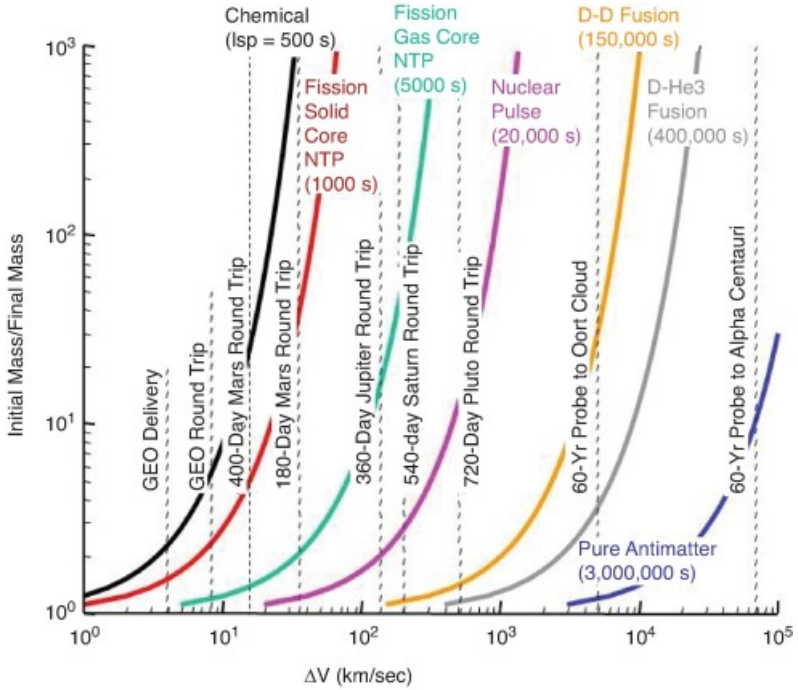

Figure 2.1: Spacecraft mass ratio as function of Δv (mission) for different propulsion specific impulses. Credit: NASA.

The grey line in Fig. 2.1 represents the D-^{3}He fusion reaction that the DFD would utilize to generate thrust.

In the following sections we discuss two alternatives to overcome the limitations of CP and EP: nuclear propulsion and propellantless systems.

2.2.1 Nuclear Propulsion

Space nuclear propulsion draws energy from fission or fusion reactions instead of traditional chemical reactions, thus providing comparatively unlimited energy. These

methods open the door for robust and enduring access throughout the solar system. The concept of using nuclear power for spacecraft propulsion stems from the high energy density of the fission or fusion reactions and the fast velocity of products that gain this energy. The onboard nuclear reactor generates heat, enabling a higher effective exhaust velocity, which in turn increases payload capacity. To produce thrust using nuclear fusion, it's essential to intensely heat a working fluid, resulting in an extremely hot plasma - a fully ionized gas composed of positive ions and free electrons. Compared to fission energy, fusion provides higher energy per nucleon and lower mass of the resulting "ash" of reaction products. The use of nuclear fusion for space propulsion has been an intriguing subject since the early days of nuclear energy systems (e.g., hydrogen bombs, see Refs. [47, 48]). In 1952 Shepherd was the first to consider the requirements for interstellar flight [49]. Today there are different approaches to utilizing nuclear fusion reactions for a fusion rocket; among these, i) the Inertial Confinement Fusion (ICF), that typically involves the impingement of an energy driver, such as a laser, onto the outer shell of an inertially confined thermonuclear material [50, 51, 48, 52], ii) the open-core Z-pinch fusion engine [53] and iii) the DFD [1] that we focused on in this work. The high temperatures required for this process present various engineering challenges, including the development of effective heating and confinement methods. Further details on nuclear propulsion are given in Chapter 4.

There are primarily two methods to harness this substantial energy for propulsive thrust: Nuclear Thermal Propulsion (NTP) and Nuclear Electric Propulsion (NEP). Additionally, hybrid NTP/NEP concepts and intriguing nuclear pulse rocket designs, such as those explored in the ORION project [54], leverage the energy from nuclear explosions. Nuclear Thermal Propulsion (NTP) and Nuclear Electric Propulsion (NEP) are both advanced space propulsion technologies that use nuclear reactions, but they operate on different principles and are suited for

different types of missions. In NTP, a nuclear reactor heats a working fluid (typically liquid hydrogen) to high temperatures. The heated fluid is then expelled through a nozzle, generating thrust. The reactor provides the heat directly to the fluid, which expands and accelerates, producing thrust. In NEP, instead, the heat generated by the nuclear reactor is converted into electrical energy (usually through a thermodynamic cycle). The electricity powers an electric propulsion system, such as an ion thruster or Hall-Effect thruster introduced in section 2.1.3, to generate thrust.

Given their operational concepts, also their performances are quite different. In fact, the NTP operates much like a conventional rocket, but with the heat from nuclear reactions instead of chemical reactions. This results in high thrust but relatively lower efficiency. The obtained I_{sp} is higher if compared to CP, typically in the range of 800–900 s in vacuum, however still much lower than that of NEP (corresponding to those of the EP).

2.2.2 Propellantless Systems

Propellantless propulsion systems in space leverage external forces or mechanisms, eliminating the need for spacecraft to carry conventional chemical or electric propellant onboard [55]. An example of a propellantless maneuver is the well-known gravity assist (or "fly-by"), using the pull of celestial bodies to change a spacecraft's speed and velocity direction. This technique, employed in missions such as *Voyager* and *Cassini* [56, 57], requires the spacecraft to follow specific trajectories and is analogous to a finite burn, despite not requiring propellant. Other environmental effects can also be used to propel a spacecraft. The primary advantage of these systems is the potential for virtually unlimited mission duration, as they are not constrained by fuel reserves, thus removing the concern of depleting propulsion resources during the mission. This makes them particularly attractive for long-duration space exploration. The Sun serves as the primary energy source within

the Solar System, emitting both electromagnetic radiation and charged particles. Electromagnetic radiation spans the entire spectrum, including ultraviolet (UV), visible, and infrared (IR) light, and carries momentum that can be transferred to objects upon reflection or absorption — this is the principle behind solar sails. Solar sails use the momentum transfer from photons to accelerate spacecraft [58]. Electromagnetic radiation hits the highly reflective surface of the sail, it imparts a small force that continuously pushes the craft forward. Over time, this force accumulates, enabling the spacecraft to reach high velocities. Additionally, the Sun produces the solar wind, a stream of charged particles (mainly protons and electrons) that continuously flows outward. Magnetic sails and electric sails harness the solar wind to generate thrust. Magnetic Sails ("mag-sails") utilize a large loop of superconducting wire to create a magnetic field that interacts with the solar wind [59, 60]. Electric sails ("e-sails"), instead, employ long charged tethers that repel solar wind protons (more advantageous than electrons due to their higher mass), to generate thrust [61, 62]. Similar to solar sails but powered by lasers, photon sails use directed energy (from lasers) to accelerate the sail [29, 63]. The idea is to build ground-based or space-based laser arrays that emit photons directly onto the sail. This concept is central to the *Breakthrough Starshot* initiative, which aims to send probes to nearby stars like Alpha Centauri [27]. Some research has also been done on trying to enhance also other radiation sources from stars, artificial sources, or other celestial phenomena [64, 65]. Besides large area structures like sails, a few other solutions have been proposed, such as electrodynamic tethers, that would interact with the magnetic field [66, 67, 68, 69, 70], however this technology would be limited in its application by the presence (and intensity) of the field. Each of these methods avoids the need for onboard propellant, relying instead on external forces like sunlight, solar wind, magnetic fields, or gravity. When examining forces within the Solar System, solar radiation is significantly more influential in deep space than others.

Table 2.1 illustrates that both at 1 AU and 5 AU (near Earth and Jupiter, respectively), the effects of solar wind, drag, and magnetic fields are comparatively less dominant [71, 72]. The values provided correspond to distances of 10 planetary radii from the respective planets. This explains why solar sails have always been considered the most promising propellantless propulsion mechanisms. Note that the forces fall off with distance significantly, showing that past a certain distance, also solar sails have limited application because the solar pressure is so low. Laser-sails might be a valid alternative after a certain distance, otherwise the traditional solar sail should start very close to the Sun for a large push.

Source	**Near Earth**	**Near Jupiter**
Solar radiation	9×10^{-5}	3.3×10^{-6}
Solar wind	3.1×10^{-8}	1.1×10^{-9}
Newtonian drag	7.9×10^{-11}	5.7×10^{-7}
Magnetic field	1.9×10^{-13}	1.6×10^{-9}

Table 2.1: Environmental forces in space at 1 and 5 AU - values in [N]. Ref: [72].

2.3 Propulsion: Final Remarks

In the final analysis of space propulsion systems, it's clear that both chemical and electric propulsion have played crucial roles in enabling human access to space and near-Earth operations [44]. Chemical propulsion, while delivering the high thrust needed for launch and rapid maneuvering, suffers from limitations in efficiency and fuel demands for extended missions. Electric propulsion, with its higher specific impulse, offers greater fuel efficiency suited to prolonged, deep space operations, even if with low thrust, limiting its use to specific applications. Advanced concepts such as nuclear propulsion and propellantless systems, including solar sails, offer promising alternatives for deep space exploration, potentially overcoming the limitations of chemical and electric thrusters in terms of fuel mass and mission duration. Hybrid solutions are also valid options to consider based on mission goals

[73]. As the space industry evolves, integrating these advanced technologies could enable more sustainable and far-reaching space travel, driving humankind closer to interstellar exploration. The future of propulsion hinges on these innovations to make ambitious missions feasible, from rapid interplanetary journeys to, one day, interstellar travel.

Chapter 3

Solar Sails

This chapter provides an in-depth overview of solar sail technology, from foundational concepts to the latest advancements. It begins with the early studies that shaped the concept of solar sails and the development of force models that explain their acceleration mechanism. Following a review of the first technology demonstrations, the chapter examines the state of the art, highlighting recent advances in materials and deployment strategies. Challenges and limitations in solar sail applications are also discussed, along with innovative approaches, such as thermal desorption, to enhance thrust. The chapter concludes by outlining the specific focus of this research within the broader context of solar sail technology.

3.1 Concept and Initial Studies

Solar sails, first theorized by K. Tsiolkovsky and F. Tsander back in the 1920s, are large sheets of low areal density material whose only source of energy is the Sun's photon flux [74].

"For flight in interplanetary space I am working on the idea of flying, using tremendous mirrors of very thin sheets, capable of achieving favorable results[1]*".*

[1]Engineer Fridrikh Tsander, 1924.

At least in theory, a solar sail mission could be of unlimited duration, thanks to the "ever-present gentle push of sunlight" [75]; a remarkable advantage is that no propellant is needed. Scientists and writers have been dreaming of solar sailing for a long time:

"Hold your hands out to the sun," he'd said. "What do you feel? Heat, of course. But there's pressure as well—though you've never noticed it, because it's so tiny. Over the area of your hands, it only comes to about a millionth of an ounce. "But out in space, even a pressure as small as that can be important—for it's acting all the time, hour after hour, day after day. Unlike rocket fuel, it's free and unlimited. If we want to, we can use it; we can build sails to catch the radiation blowing from the sun[2]*."*

Interest in solar sails grew in the 1970s with NASA's theoretical studies, though no practical missions materialized at the time. In the following decades, hundreds of theoretical and experimental studies on solar sailing were published. In 2010 the JAXA team announced the successful deployment of *IKAROS*, the world's first interplanetary solar sail (about 200 m^2), demonstrating spacecraft propulsion using solar radiation pressure (SRP).

Unlike chemical rockets that provide short, powerful bursts of acceleration (very high thrust with low specific impulse), solar sail acceleration is slow but continuous - and, if wisely driven, this device can reach much higher speeds.

Theoretical prediction that electromagnetic radiation exerts pressure on any exposed surface was first made by James Clerk Maxwell in 1873. Maxwell presented the core findings of his electromagnetic wave theory to the Royal Society on December 8, 1864, and published them in 1865 [76], later elaborating in his renowned

[2] *The Wind from the Sun* by Arthur C. Clarke, 1972; A part of the book was included in CD onboard the Planetary Society's solar sail, *Cosmos-1.*

work, *A treatise on electricity and magnetism* [77]. According to Maxwell's theory, electromagnetic waves carry energy that produces radiation pressure. Pyotr Lebedev was the first to experimentally measure light's pressure on a solid object in 1899 [78]. Following Lebedev, Nichols and Hull from Dartmouth College confirmed this phenomenon, collecting initial data in 1901 and publishing conclusive results in 1903 [79]. Together, the results from Lebedev and Nichols and Hull offered the first definitive evidence of measurable radiation pressure from light. In 1915, Yakov Perelman proposed using solar radiation pressure to propel spacecraft in his book *Interplanetary Journeys* [80]; however, he concluded that the pressure would likely be too weak for effective propulsion. The concept of solar sailing later gained traction as an engineering principle, particularly in the early 20th century, advocated by figures such as K. Tsiolkovsky and F. Tsander [81, 74]. Interest in solar sailing lay dormant for roughly 30 years, re-emerging in the mid-20th century when Richard Garwin coined the term "Solar Sailing" in the journal *Jet Propulsion* [82].

3.2 First Technology Demonstrations

The first attempt to showcase solar sailing was the *Cosmos-1* mission, which was a project by Cosmos Studios and The Planetary Society to test a solar sail in space. This mission failed due to a launch vehicle malfunction in 2005. Japan's *IKAROS* mission, launched by JAXA in 2010 [83, 84, 85], became the first spacecraft to successfully employ solar sail propulsion in interplanetary space. The sail generated measurable thrust, proving that sunlight could effectively power spacecraft for deep space missions [58]. In parallel, NASA's *NanoSail-D2* mission [86], launched the same year, validated the viability of solar sailing in Earth orbit on a smaller scale. These early milestones paved the way for more advanced applications. In 2015 *LightSail-1* successfully deployed its sail [87] and in 2019 *LightSail-2* became the

first small spacecraft to change its orbit using only sunlight for propulsion [88]. This success of the Planetary Society's sails highlighted their potential for propelling small, fuel-less spacecraft, critical for long-duration missions in deep space.

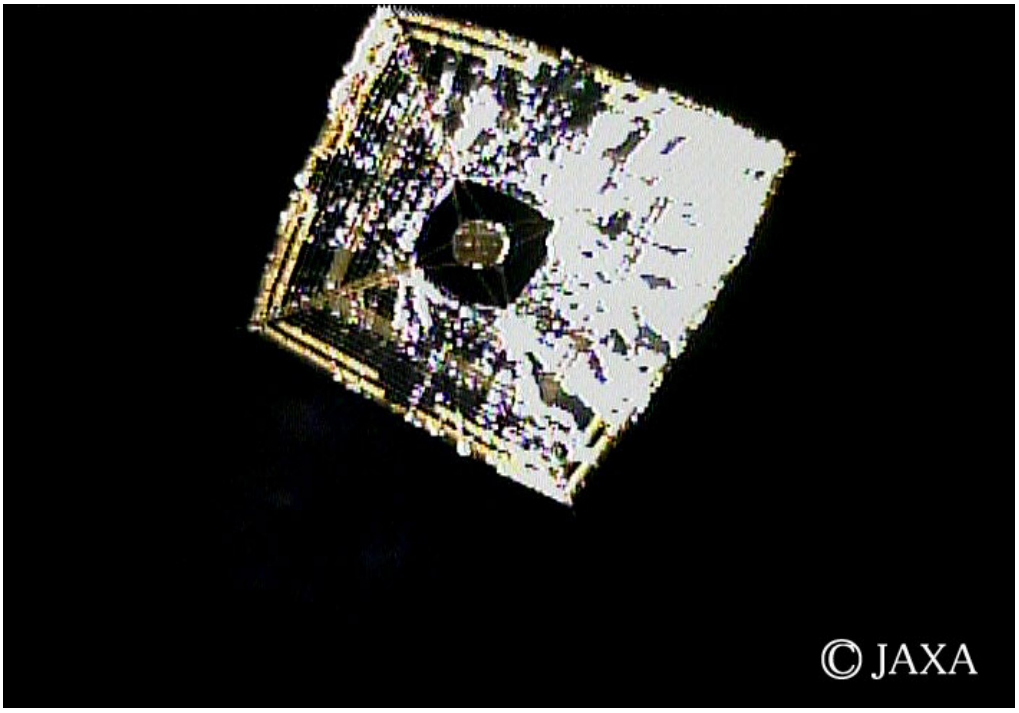

Figure 3.1: The Japan Aerospace Exploration Agency's *IKAROS* solar sail is seen in deep space after its deployment on June 14, 2010, in this view taken from a small camera ejected by the sail. Credit: JAXA.

3.3 State of the Art and Recent Advances

To promote collaboration within the scientific community, the 1st International Symposium on Solar Sailing (ISSS) was held in June 2007 in Herrsching, Germany. Advances in solar sail concepts, technologies, dynamics and control, and mission design were documented in a special issue of Advances in Space Research (ASR) titled *Solar Sailing: Concepts, Technology, and Missions* [84]. Ten years later, after three successful ISSS symposia (2013, 2017 and 2019 held in the UK, Japan and Germany respectively) and numerous publications in the field, a second special

issue reflected the vibrant reality of solar sailing research [89]. Meanwhile, review papers were also produced regularly on the topic [72, 90, 91].

Ongoing research continues to focus on improving sail materials and deployment mechanisms for future interplanetary missions. A recent milestone was achieved with Gama's first demonstrator mission, *Gama Alpha*, launched aboard a SpaceX *Falcon 9* on January 3, 2023. The 6U CubeSat, weighing just 12 kg (about the size of a large shoebox), carried a 73 m^2 solar sail. The *Gama Alpha* mission focused on demonstrating successful sail deployment, while its follow-up mission, *Gama Beta*, will aim to demonstrate solar sail propulsion and navigation [92]. NanoAvionics, a Lithuanian company specializing in nanosatellite platforms, played a crucial role in the development of *Gama Alpha*, Europe's first solar sail mission, designed with the support of the French Space Agency, CNES. NanoAvionics provided critical components for *Gama Alpha*, including electrical systems, telecommunications, and on-board hardware, which were essential in enabling the mission's success [93, 94]. Building on the success of the Gama mission, NanoAvionics also supplied the satellite bus for NASA's Advanced Composite Solar Sail System (*ACS3*), a 12U CubeSat carrying an 80 m^2 solar sail, designed to demonstrate solar sail technology for future small spacecraft applications [95]. Among its objectives is to showcase solar sails' capabilities for orbit control, including adjusting the semimajor axis to achieve various orbital altitudes. Following its April launch, *ACS3* was confirmed as fully operational on August 29, 2024 [96]. Table 3.1 reports missions that have been successful since *IKAROS* launch in 2010, whereas failed attempts are listed in Table 3.2. In all circumstances lessons learnt came out of the process: failure has to be considered an option when pushing the boundaries of technology.

Several solar sail missions have faced significant challenges, resulting in either failure or cancellation. The *Cosmos-1* mission, launched by The Planetary Society in 2005, was intended to be the first spacecraft to demonstrate solar sail propulsion.

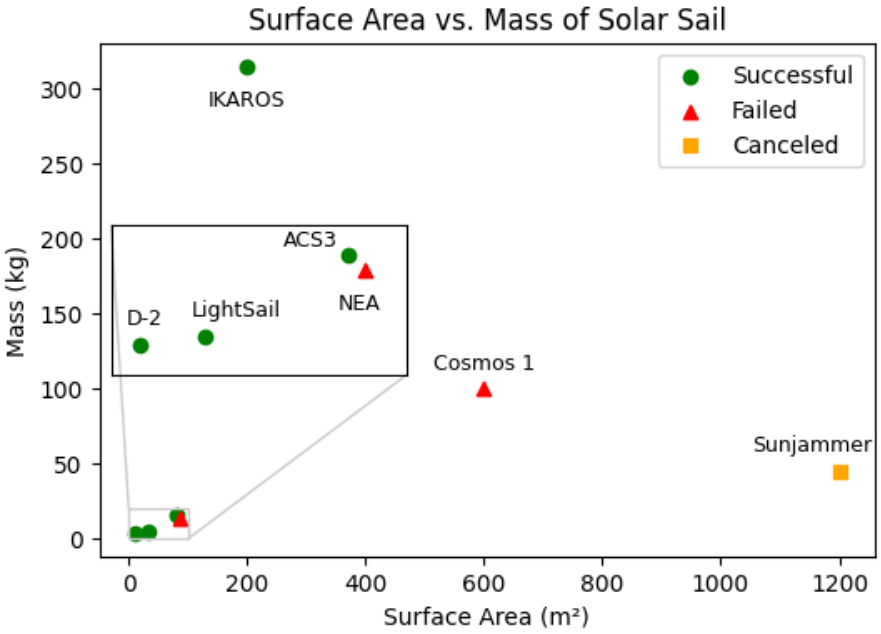

Figure 3.2: Sail area and mass (including the sail and its associated hardware) for some missions of the past decades.

Year	Name	Organization	Highlights
2010	IKAROS	JAXA	First interplanetary solar sail mission
2011	NanoSail-D2	NASA	Solar sail deployed in Earth orbit
2015	LightSail-1	Planetary Society	Successful sail deployment in orbit
2019	LightSail-2	Planetary Society	First to change orbit using sunlight
2023	Gama Alpha	GAMA	6U CubeSat with 73m^2 solar sail
2024	ACS3	NASA	12U CubeSat with 80m^2 solar sail

Table 3.1: Successful Solar Sail Missions

Year	Name	Organization	Highlights
1999	Znamya 2.5	ROSCOSMOS	Reflector failed, broke apart
2005	Cosmos-1	Planetary Society	Launch vehicle failure
2008	NanoSail-D	NASA	Rocket failure prevented deployment
2022	NEA Scout	NASA	Lost communication after launch

Table 3.2: Failed Solar Sail Missions

However, it failed due to a malfunction in the launch vehicle, preventing the spacecraft from reaching orbit. NASA's *Solar Sail Demonstrator*, initiated in 1999, was canceled before launch due to budgetary and technical constraints, stalling further solar sail research at that time. In 2008, NASA's *NanoSail-D* mission aimed to test solar sail technology in low Earth orbit, but the *Falcon 1* rocket failed, resulting in the loss of the spacecraft. Russia's ROSCOSMOS also encountered setbacks with its *Znamya 2.5* mission, wide space solar mirror, in 1999. Soon after deployment, the reflector caught on an antenna on the Progress and ripped. The reflector failed to deploy properly and broke apart.

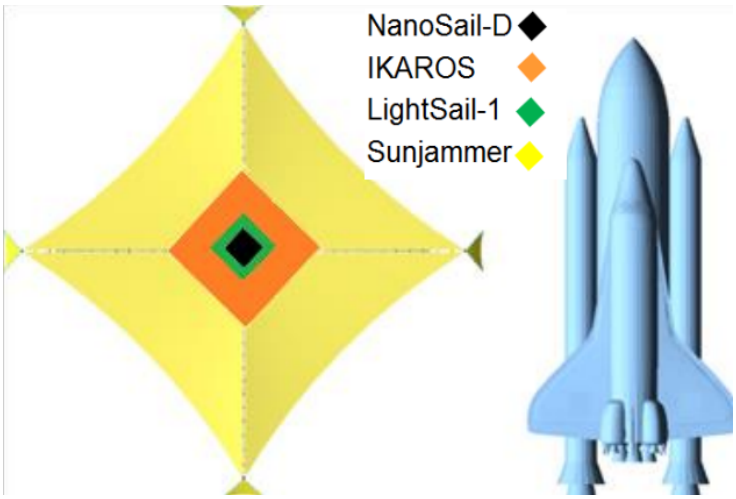

Figure 3.3: Sunjammer dimensions compared to other sails and the Space Shuttle. Credit: O. Eldad and G. Lightsey [97].

NASA's *Sunjammer* mission, led by the private company L'Garde Inc. and planned for 2014, was also canceled due to technical challenges and budget constraints [98]. Similarly, the European Space Agency's *Gossamer* mission was canceled in 2015 after facing technical issues and shifting priorities within ESA [99]. *Sunjammer*, named after a short story written by Sir Arthur C. Clarke, with a surface of 1200 m^2 (and a weight of just 45 kg) was meant to be much bigger than sails designed before, as shown in Fig. 3.3. Its area was twice that of *Cosmos-1* (600 m^2) and around six times that of *IKAROS* (200 m^2). More recently, the *Near-Earth*

Asteroid Scout (NEA Scout), a CubeSat mission launched aboard NASA's *Artemis I* in 2022, was expected to be the first CubeSat to study a near-Earth asteroid using solar sail propulsion. Unfortunately, after launch, communication was never established with the spacecraft, and multiple attempts to deploy its solar sail failed [100]. The mission was subsequently declared lost, marking another setback in solar sail development. Another interesting concept proposal was the *Solar Cruiser*, with a surface of more than 1600 m^2, which was expected to launch as a rideshare payload alongside the *Interstellar Mapping and Acceleration Probe (IMAP)* in February 2025 [101]. Although the *Solar Cruiser* mission was not approved to advance to phase C, its closeout plan included the development and advancement of several key technologies as well as the demonstration of a full quadrant sail deployment, which was successfully completed [102] and achieved NASA's Technology Readiness Level (TRL) 6 through extensive testing (January 2024) [103].

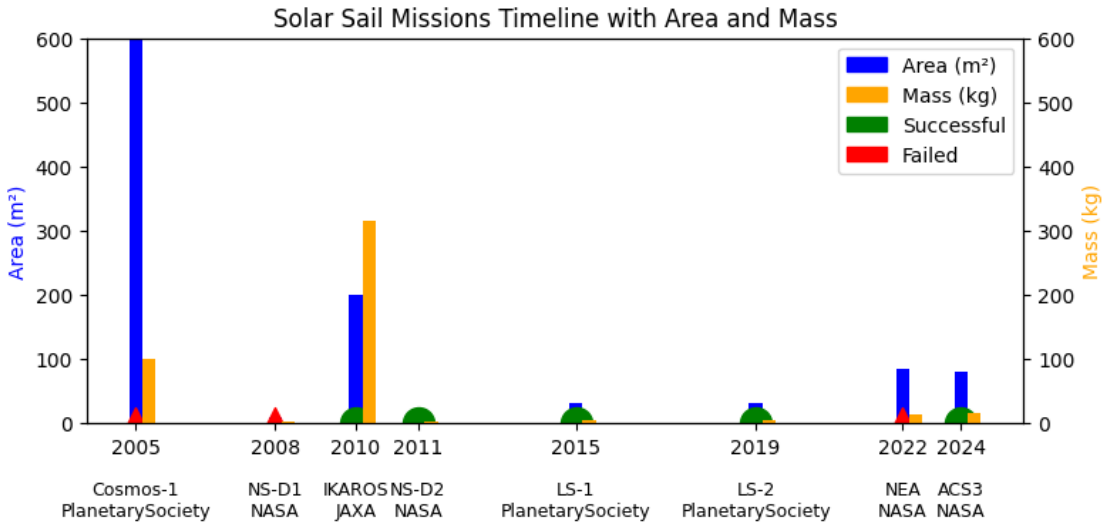

Figure 3.4: Sail missions timeline and characteristics

It is clear that, despite these challenges, valuable lessons from the unsuccessful and canceled missions continue to inform and improve the design and operation of future solar sail projects. Fig. 3.2 shows mass and area features for some of the missions mentioned above. Their characteristics are also reported in Fig. 3.4

and in Tab. 3.3 ordered by their launch dates. Although the basic idea behind solar sailing appears simple, challenging engineering problems have to be solved [104, 105]. Given the many applications and their great potential, solar sails are nowadays also being considered for various activities, such as deorbiting satellites ("drag sail") [106, 107]. The solar sailing community is actively trying to address these by fostering collaboration in conferences and forums such as the ISSS.

Mission	**Year**	**Status**	**m (kg)**	**A (m^2)**	**D (kg/m^2)**
Cosmos-1	2005	F	100	600	0.167
NanoSail-D1	2008	F	4	10	0.400
IKAROS	2010	S	315	200	1.575
NanoSail-D2	2011	S	4	10	0.400
LightSail-1	2015	S	5	32	0.156
LightSail-2	2019	S	5	32	0.156
NEA Scout	2022	F	14	86	0.163
GAMA Alpha	2023	S	12	73	0.164
ACS3	2024	S	16	80	0.200

Table 3.3: Solar Sail missions launched, their status (success/fail) and design details: mass (m), area (A) and resulting areal density (D).

3.4 Force Models and Acceleration Mechanism

In quantum mechanics, photons are the "packets of energy" that light is made of. Planck's law states that a photon of frequency ν will transport an amount of energy equal to:

$$E = h_P \nu = h_P \frac{c}{\lambda}, \tag{3.1}$$

where λ is the wavelength, c is the speed of light and $h_P = 6.626 \cdot 10^{-34} Js$ is the Planck's constant. Also the Einstein's mass-energy equation of special relativity gives the expression for the energy of a moving body, as function of its rest mass m and its momentum p:

$$E^2 = m^2 c^4 + p^2 c^2. \tag{3.2}$$

Photons have no mass, so, from Eq. (3.2), one can find that the momentum transported by a single photon is:

$$p = \frac{E}{c} = \frac{h_P \nu}{c}. \tag{3.3}$$

To evaluate the pressure exerted on the sail, it is necessary to consider the momentum transported not by a single photon, but by a flux of photons. Based on the inverse square law the energy flux ϕ (also said solar irradiance) depends on the distance r of the body from the Sun as:

$$\phi \left[\frac{W}{m^2}\right] = \phi_E \left(\frac{R_E}{r}\right)^2 = \frac{3.04 \cdot 10^{25}}{r^2}, \tag{3.4}$$

where $R_E = 1\,AU$ (Sun-Earth distance) and $\phi_E = L_S / \left(4\pi R_E^2\right) = 1346\,W/m^2$ is the Solar irradiance at Earth distance, defined through the solar luminosity L_S.

As ϕ is the energy crossing a unit area in unit time, the energy transported across a surface of area A normal to incident radiation in time Δt is:

$$\Delta U = \phi \cdot A \cdot \Delta t. \tag{3.5}$$

Using Eq. (3.3) the radiation pressure, representing the momentum transported per unit time, per unit area, can be obtained:

$$P = \frac{1}{A}\left(\frac{\Delta p}{\Delta t}\right) = \frac{\phi}{c}. \tag{3.6}$$

Assuming that the sail reflects part of the incident radiation, the total pressure acting on the sail can be written as function of the reflectivity parameter ϱ:

$$P_{sail} = \frac{1+\varrho}{c}\phi. \tag{3.7}$$

Considering perfect reflectivity ($\varrho = 1$) one finds $P_{sail} \equiv P_{sail_{MAX}} = 2P$. At a distance of $r = 1AU$, where $P \equiv (P_0)_{1AU} = 4.5\ N/km^2$, the pressure on a

perfectly reflecting sail would be $P_{sail_{MAX}} = 2\,(P_0)_{1AU} = 9\ N/km^2 = 9 \cdot 10^{-6} N/m^2$. Taking into account non-perfect reflection, a conservative value of sail efficiency $\eta \simeq 0.85$ can be used to evaluate the effective pressure on a sail at $r = 1AU$ oriented perpendicularly to the sun-line: $(P_{eff})_{1AU} = 2 \cdot \eta\,(P_0)_{1AU} = 7.7\ N/km^2$.

Force and Acceleration for a Perfectly Reflecting Solar Sail Consider a solar radiation pressure P acting on the sail's center of surface as shown in Fig. 3.5 (here and below $\mathbf{e}_r$ is the unit vector directed as the incident radiation, $\mathbf{e}'_r$ the one directed as the reflected radiation, and $\mathbf{n}$ the vector normal to the sail surface) then the force exerted on the sail can be written as:

- $\mathbf{F}_r = P_{sail} \cdot [A \cdot (\mathbf{e}_r \cdot \mathbf{n})]\,\mathbf{e}_r$ due to photons incident radiation in the $\mathbf{e}_r$ direction
- $\mathbf{F}'_r = -P_{sail} \cdot [A \cdot (\mathbf{e}_r \cdot \mathbf{n})]\,\mathbf{e}'_r$ due to photons reflected radiation in the $\mathbf{e}'_r$ direction

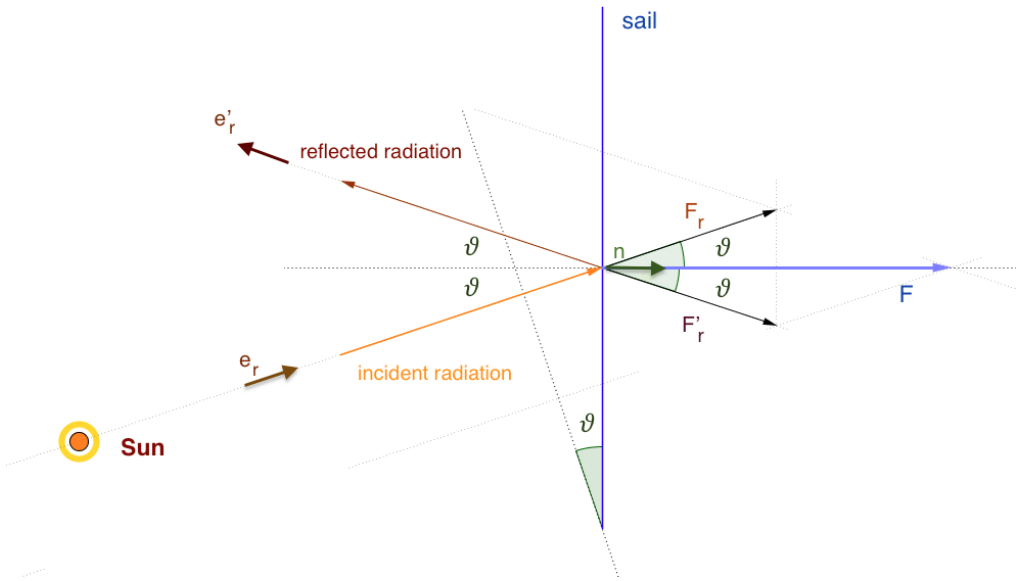

Figure 3.5: Force exerted on the sail with perfect reflection and angle of incidence ϑ.

where $[A \cdot (\mathbf{e}_r \cdot \mathbf{n})]$ is the projected sail area in the $\mathbf{e}_r$ direction. The thrust obtained, if the sail is oriented with an angle of incidence ϑ (*sail pitch angle*) with respect to

the Sun, using Eq. (3.6) (for perfect reflection) and (3.4), is given as:

$$\mathbf{T} = 2 \cdot \frac{\phi_E}{c} \left(\frac{R_E}{r} \right)^2 \cdot A \cdot cos^2\vartheta \cdot \mathbf{n}. \tag{3.8}$$

The thrust vector of a solar sail is constrained on a "bubble" surface (green in Fig. 3.6) directed away from the Sun [108]. The sail can lose or gain orbital angular momentum and change its orbit by controlling its orientation relative to the Sun depending on the scalar product of the thrust vector $\mathbf{F}$ with the vector tangent to the trajectory, $\mathbf{e}_t$:

- if $\mathbf{F} \cdot \mathbf{e}_t \equiv F \cdot e_t \cdot cos\delta < 0$ (relative clock angle > 90 deg) the sail loses angular momentum and starts to spiral inwards - towards the Sun (from A to B);

- if $\mathbf{F} \cdot \mathbf{e}_t \equiv F \cdot e_t \cdot cos\delta > 0$ (relative clock angle < 90 deg) the sail gains angular momentum and starts to spiral outwards - away from the Sun (from C to D);

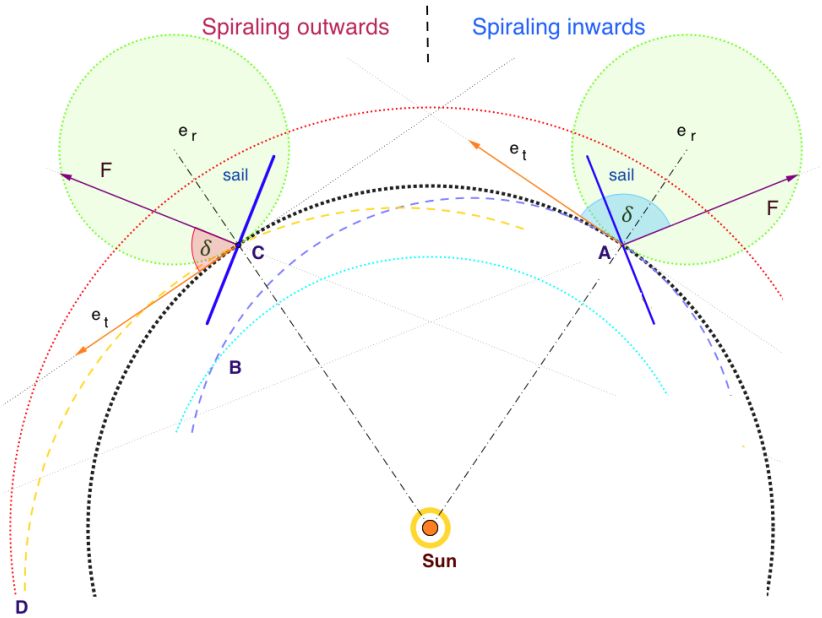

Figure 3.6: Spiraling inwards (from A to B) and outwards (from C to D).

For what concerns the sail acceleration:

$$\mathbf{a} = \frac{\mathbf{T}}{m} = 2\frac{\phi_E}{c}\left(\frac{R_E}{r}\right)^2 \frac{A}{m} cos^2\vartheta \mathbf{n}. \tag{3.9}$$

To experience a great acceleration the sail needs to be large ($A \uparrow$) and very light ($m \downarrow$). Because these two quantities, sail area and sail total mass, have a strong influence on the sail acceleration, a new parameter is introduced, the sailcraft loading factor σ, defined as the mass per unit area m/A $[g/m^2]$. The latter allows to rewrite Eq. (3.9) as:

$$\mathbf{a} = 2\frac{\phi_E}{c}\left(\frac{R_E}{r}\right)^2 \frac{1}{\sigma} cos^2\vartheta \mathbf{n}. \tag{3.10}$$

Force and acceleration for a not perfectly reflecting solar sail As a "real" solar sail is not a perfect reflector, a small fraction of the incident radiation may be absorbed and/or reflected not specularly, giving rise to a tangential force component; due to this, the thrust will no longer be along the $\overline{n}$ direction, although this component could be neglected for small ϑ angle. Considering a generic sail not perfectly reflecting, by using Eq. (3.7) the thrust is:

$$T = P_{sail} \cdot A cos^2\vartheta = \frac{1+\varrho}{c}\phi A cos^2\vartheta; \tag{3.11}$$

furthermore one can obtain acceleration as function of sail design and heliocentric distance:

$$a = \frac{P_{sail} \cdot A \cdot cos^2\vartheta}{m} = \frac{1+\varrho}{c}\phi\frac{1}{\sigma} \cdot cos^2\vartheta = 3{,}04 \cdot 10^{25}\frac{1+\varrho}{\sigma \cdot c \cdot r^2} \cdot cos^2\vartheta. \tag{3.12}$$

3.4.1 Performance Parameters

Some key parameters will be useful to evaluate a solar sail. If $m = m_s + m_{pl}$ is the total mass, where m_s is the mass of sail and m_{pl} is the mass of payload, then one can define:

- the sailcraft loading factor σ, defined via the total mass m that includes the payload,

$$\sigma = \frac{m}{A} = \frac{m_s + m_{pl}}{A} = \sigma_s + \frac{m_{pl}}{A} \quad \left[\frac{g}{m^2}\right].$$

- the characteristic acceleration a_0

$$a_0 = \frac{(P_{eff})_{1AU}}{\sigma} = \frac{2\eta\,(P_0)_{1AU}}{\sigma} \quad \left[\frac{mm}{s^2}\right], \tag{3.13}$$

  that is the maximum acceleration that can be experienced by the sail at a distance of $r = 1\,AU$, when the angle of incidence $\vartheta = 0°$ and the sail is normal to the Sun.

- the lightness number β

$$\beta = \frac{a_0}{(g)_{1AU}} = \frac{a_0}{5.93\,mm/s^2}, \tag{3.14}$$

  that is the ratio of the acceleration due to solar radiation pressure experienced by a solar sail perpendicular to the sun line at $r = 1\,AU$ (so the characteristic acceleration) and the acceleration caused by solar gravitation at the same distance $(g)_{1AU} = 5.93\,mm/s^2$.

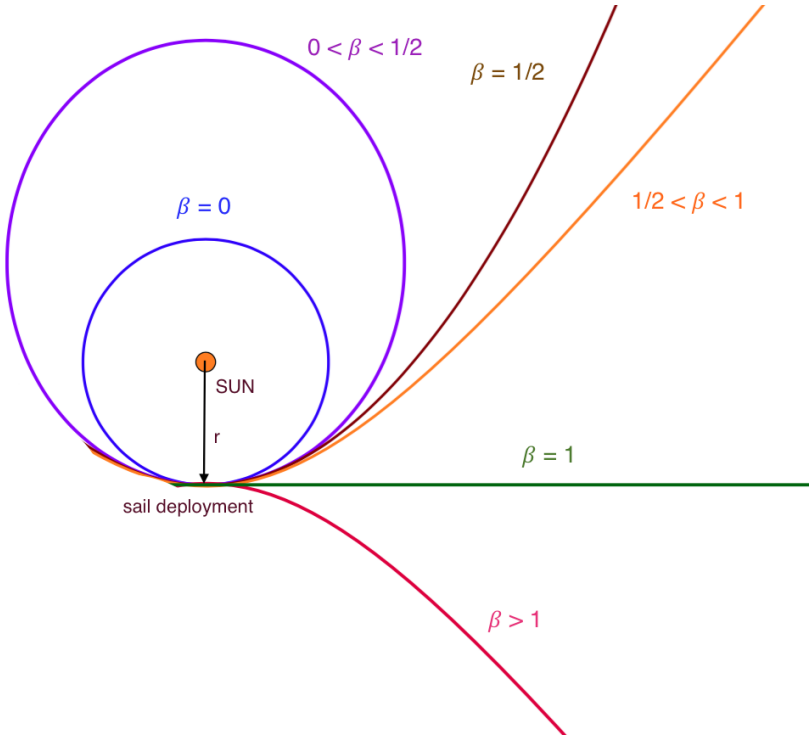

Figure 3.7: Classification of the orbit type for different solar sail lightness numbers.

$\beta = 0$	circular orbit	$E_g < 0$	$v = v_c$	$\mathfrak{a} = r$
$0 < \beta < 1/2$	elliptical orbit	$E_g < 0$	$v < v_{esc}$	$\mathfrak{a} > 0$
$\beta = 1/2$	parabolic orbit	$E_g = 0$	$v = v_{esc}$	$\mathfrak{a} \to \infty$
$1/2 < \beta < 1$	hyperbolic orbit (Sun inner focus)	$E_g > 0$	$v > v_{esc}$	$\mathfrak{a} < 0$
$\beta = 1$	rectilinear trajectory	$E_g > 0$	$v > v_{esc}$	/
$\beta > 1$	hyperbolic orbit (Sun outer focus)	$E_g > 0$	$v > v_{esc}$	$\mathfrak{a} < 0$

Tabella 3.4: Classification of solar sail orbits.

The sail follows a circular Keplerian orbit for a lightness number $\beta = 0$. When β is nonzero but within the range $0 < \beta < 1/2$, the orbit is elliptical. At $\beta = 1/2$, the trajectory reaches a critical threshold where an elliptical orbit transitions into a parabolic orbit, marking the minimum lightness number required for direct escape from the gravitational influence of the Sun. As

β increases further, within the range $1/2 < \beta < 1$, the trajectory becomes hyperbolic, allowing the sail to escape the Solar System. When $\beta = 1$, an equilibrium condition arises in which solar gravity is precisely counteracted by solar radiation pressure, resulting in a net-zero radial acceleration.

Using the lightness number, the solar sail acceleration could also be written in term of solar gravitational acceleration as:

$$\mathbf{a} = \beta \frac{GM_s}{r^2} \cdot cos^2\vartheta \cdot \mathbf{n}, \tag{3.15}$$

where $M_s = 1.99 \cdot 10^{30} kg$ is the mass of the Sun and $G = 6.67 \cdot 10^{-11} m^3/s^2 kg$ is the universal gravitational constant. Since both accelerations have an inverse square dependence in r this means that the lightness number is independent of the sail distance from the Sun. By means of Eqs. (3.10), (3.15) and substituting $\phi_E = L_S/\left(4\pi R_E^2\right)$ one can get:

$$\beta = \frac{L_s/\left(2\pi G M_s c\right)}{\sigma} = \frac{\sigma^*}{\sigma} = \frac{1.53\, g/m^2}{\sigma}, \tag{3.16}$$

where the constant $\sigma^* = 1.53\, g/m^2$ is the critical solar sail loading parameter; it is said "critical" because with this mass per unit area $\beta = 1$ and the two accelerations are exactly equal.

The lightness number β is also important in determining the orbit type [58] as shown in Fig. 3.7 and Tab. 3.4, where E_g is the orbit mechanical specific energy, $\mathfrak{a}$ is the semimajor axis and v_c and v_{esc} are the circular and escape velocity respectively.

3.5 Thermal Desorption for Additional Thrust

Thermal desorption is a process of mass loss that dominates all other similar processes above temperatures of 300-500 °C. Some special heat-sensitive materials can

undergo the transition from the solid state phase into the gas phase at a particular temperature. By heating to temperatures of 800-1000 K a sail on which surface there is a coat of embedded atoms or paint, their thermal desorption can provide higher specific impulse than liquid rockets as experimentally shown in Ref. [109]. The chemical process consists of atoms, embedded in a substrate, that are liberated by heating, thus providing an additional thrust. Desorption can attain high specific impulse if low-mass molecules are blown out of a lattice of material at high temperature [3].

3.5.1 The Thermal Desorption Chemical Process

An "adatom" (adsorbed atom) present on a surface at low temperatures may remain almost indefinitely in that state. As the temperature of the substrate is increased, however, there will come a point at which the thermal energy of the adsorbed species is such that it may desorb from the surface and return into the gas phase.

The rate of desorption R_d of an adsorbed species from a surface can be expressed in the general form as:

$$R_d = k_d \left(N_A\right)^q , \tag{3.17}$$

where N_A is the surface concentration of adsorbed species, q is the kinetic order of desorption and k_d is the rate constant for desorption. The latter one is commonly described by an Arrhenius type equation [110]:

$$k_d = \nu_0 \, \exp\left(-\frac{E_A}{k_B \mathcal{T}}\right), \tag{3.18}$$

where ν_0 is the pre-exponential frequency factor and its typical value is $10^{13} s^{-1}$, E_A is the activation or liberation energy (usually $\leq 1\, eV$), $\mathcal{T}$ is the temperature and $k_B = 1.38 \cdot 10^{-23}\, JK^{-1}$ is the Boltzmann constant, that is the gas universal constant divided by the Avogadro constant.

The order of desorption q mostly depends on the type of considered reaction: usually it is a first-order process if it involves atomic or simple molecular desorption. Sometimes ν_0 is also called the "attempt frequency" at overcoming the barrier to desorption. In the particular case of simple molecular adsorption, ν_0 corresponds to the frequency of vibration of the bond between the atom or molecule and substrate. This is because every time the bond is stretched during the course of a vibrational cycle could be considered as an attempt to break the bond and, hence, an attempt at desorption. In general, it was found that the pre-exponential frequency factor can span a wide range of values from $10^{13}s^{-1}$ to $10^{21}s^{-1}$ depending on the vibrational degrees of freedom of the adsorbate [110].

From Eqs. (3.17) and (3.18) the general expression for the rate of desorption can be obtained, considering that it corresponds to the time reduction of adatoms present on the surface:

$$R_d = -\frac{dN_A}{dt} = \nu_0 \ (N_A)^q \ \exp\left(-\frac{E_A}{k_B \mathcal{T}}\right). \tag{3.19}$$

The rate of mass loss under heating dN_A/dt is the desorbed flux in $atoms/m^2 s$. Note that the exponential factor suggests that the desorption will have a sudden onset after the surface gets warm [3]. Equation (3.19) can be formally solved when temperature varies with time. As the activation energy increases, the time to desorb gets longer, because the rate of desorption decreases.

A relation between the activation energy and the temperature at which desorption occurs can be derived from Eq. (3.19) and it is known as the Redhead equation [110, 111]:

$$E_A = R\mathcal{T}_{md}\left(\ln\frac{\nu_0 \mathcal{T}_{md}}{R_h} - 3.64\right). \tag{3.20}$$

In Eq. (3.20) R is the universal gas constant, $\mathcal{T}_{md}$ is the temperature at which the rate of desorption reaches its maximum, and R_h is the heating rate. Experimental

values for E_A have been found in Ref. [110] for carbon dioxide and monoxide, that are almost 24 and 13 kJ/mol, respectively.

This model does not fully correspond to reality, as desorption is a process that never occurs in isolation. Before an atom or molecule can desorb it must reach the surface in some way, lose energy to reach an approximate thermal equilibrium and then gain energy from the surface. The adsorbed atom is never in complete thermal equilibrium with the surface and models that begin with a thermal equilibrium assumption frequently encounter problems that can be traced to the fact that the true equilibrium state is one in which the atom has already desorbed and is far from the surface [112]. Despite this, the model is still accurate for preliminary calculations. More studies on the thermal desorption chemical process in Ref. [113, 114].

Surface Residence Time The surface residence time t_{sr} (also known as delay time) is the average time that a molecule or an adatom will spend on the surface, for a specified temperature, before it desorbs [115]. It is defined as the inverse of the rate constant for desorption k_d:

$$t_{sr} \equiv \frac{1}{k_d} = t_{sr\,0}\, \exp\left(\frac{E_A}{k_B \mathcal{T}}\right), \tag{3.21}$$

where $t_{sr\,0} = 1/\nu_0 \cong 10^{-13} s$ corresponds to the period of vibration of the bond between the adsorbed atom and substrate. Note that the sign of the exponential has changed coherently with respect to the rate of desorption (the higher the rate, the lower the residence time). This result is known as Frenkel's law.

3.5.2 Desorption as a Propulsion Mechanism

Thermal desorption was suggested as a propulsion method in Ref. [109, 116]. The original idea was to use a microwave beam to heat a solar sail until its surface

coat sublimes or desorbs. They thought of two different scenarios: a ground-based microwave beamer where the microwave power source is stationary on the ground, and alternatively an orbital-boosting method where the orbiting microwave beamer is deployed behind a solar sail in the same initial circular orbit. In this study instead, the suggestion is to use space environmental effects, such as solar radiation heating, to accelerate a conventional coated solar sail, as already proposed in Ref. [117].

Robert Forward first proposed microwave-driven sail as an alternative to his laser sail concept [118, 119], but no experiments were possible until light carbon appeared, because other materials did not allow lift-off under Earth's gravity. As carbon sublimes instead of melting, it can operate at very high temperatures. James and Gregory Benford conducted experiments on ultralight sails in carbon and found out that photonic pressure can account for 3 to 30% of the observed acceleration, while the remainder comes from the desorption of embedded molecules [109]. Here is the extraordinary potential of this sort of propulsion mechanism: if sapiently used, desorption could enhance thrust by many orders of magnitude over solar sails' conventional thrust, for example, shortening the escape time to weeks, instead of years for conventional solar sails [116].

The acceleration from photon momentum a_P produced by a power W on a thin film of mass m, area A and reflectivity ϱ is:

$$a_P = (\varrho + 1)\,\frac{W}{m_A \cdot A \cdot c}, \tag{3.22}$$

where $m_A = m/A$ is the mass per unit area and corresponds to the solar sail's σ. Of the power incident in the film, a fraction αW will be absorbed, which in steady state must be radiated away from both sides of the film, according to Stefan-Boltzmann law:

$$\alpha W = 2A\,\zeta\,\sigma_{SB}\,\mathcal{T}^4, \tag{3.23}$$

where ζ is the film emissivity that is assumed to be the same for both sides of the film surface and $\sigma_{SB} = 5.67 \cdot 10^{-8} W\, m^{-2} K^{-4}$ is the Stefan-Boltzmann constant. Substituting W/A from (3.23) into (3.22) the acceleration clearly turns out to be strongly limited by temperature $\mathcal{T}$:

$$a_P = \frac{2\sigma_{SB}}{c} \frac{\zeta\,[\varrho + 1]}{\alpha} \frac{\mathcal{T}^4}{m_A} = 3.78 \cdot 10^{-16} \frac{\zeta\,[\varrho + 1]}{\alpha} \frac{\mathcal{T}^4}{m_A}. \tag{3.24}$$

But there is also another mechanism which should be considered: acceleration due to the sublimation of the coating material mass. In fact, due to mass ejected from the material in a direction, a force rises in the opposite one:

$$F = v_{th} \frac{dm}{dt}, \tag{3.25}$$

which determines the acceleration due to thermal desorption,

$$a_D = \frac{v_{th}}{m} \frac{dm}{dt}, \tag{3.26}$$

where v_{th} is the thermal speed of the evaporated material. This acceleration can vastly exceed that of photon pressure, if the temperature is high enough.

The ratio of the acceleration is

$$\frac{a_D}{a_P} = \frac{2}{\pi g^*} \frac{c}{v_{th}}, \tag{3.27}$$

where g^* represents the degrees of freedom of the exhaust gas. This means that $a_D/a_P \gg 1$ for plausible temperatures: for instance $a_D/a_P \gg 4.5 \cdot 10^4$ for molecular hydrogen at $\mathcal{T} = 1000\, K$ as in Ref. [3].

Dependence of thermal velocity on temperature: the Maxwell distribution of velocities If N particles of molecular mass m_p leave the sail surface at velocity v_{th}, as follows from the law of conservation of total momentum,

the sail of mass m will move in the opposite direction with velocity v, that is $v = (N\, m_p\, v_{th})\,/m$. To determine the sail velocity, it is necessary to evaluate the thermal speed v_{th} of the evaporated particles. Note that, as there is no nozzle in a solar sail, molecules may leave the surface at random angles. However, due to the large desorption surface area, assuming a uniform distribution of subliming matter over the surface, the averaging by random angles leans towards the normal to the surface. Moreover, some materials tend to concentrate sublimed matter toward the normal to the surface, so as a first approximation one could consider v_{th} as the exhaust velocity. From the Maxwell speed distribution this speed as well as the average and most probable speeds can be calculated.

Let $N\,\mathfrak{p}\,(v_{th})\,dv_{th}$ be the number of atoms with speed in the range dv_{th} at v_{th}, so with velocity magnitude between v_{th} and $v_{th} + dv_{th}$. With the assumption that all particles leave the substrate in an orthogonal direction to the surface, their momentum is $[N\,\mathfrak{p}\,(v_{th})\,dv_{th}]\; m_p\, v_{th}$. Using the latter expression and applying the Maxwell distribution function to express the probability $\mathfrak{p}\,(v_{th})$ as a function of the temperature, both the mean speed $\overline{v}$ and the total momentum p can be obtained by integrating it over $v_{th} = 0$ to infinity:

$$\overline{v} = \sqrt{\frac{8k_B\mathcal{T}}{\pi m_p}}, \tag{3.28}$$

$$p = \sqrt{8\pi\, N\, m_p\, \mathcal{T}}. \tag{3.29}$$

From Eq. (3.29) follows that the momentum of thrust appears to be proportional to the square root of the temperature. However, since the acceleration of the solar sail is also proportional to the momentum,

$$a_D = \frac{F}{m} = \frac{p}{m\; t} = \frac{\sqrt{8\pi\, N\, m_p\, \mathcal{T}}}{m\; t}, \tag{3.30}$$

it follows that also acceleration is proportional to $\sqrt{\mathcal{T}}$ and to the inverse of the

desorption time. This result can be compared to the photon pressure acceleration a_P in Eq. (3.24), which was strongly limited by temperature, being proportional to $\mathcal{T}^4$.

3.5.3 Thermal Desorption for a Sail Coating

Now consider a sail coated with a material that undergoes thermal desorption. In Ref. [120] the minimum thickness requirement for a solar sail was investigated. Based on that study, one can assume a sail thickness of tens of nanometers, for example $H = 40\,nm = 40 \cdot 10^{-9}\,m$, corresponding to 400 $\mathring{A}$, being 1 $\mathring{A} = 10^{-10}\,m$. The proposed coating is in Carbon, as suggested in Ref. [3]. The acceleration due to thermal desorption is given by Eq. (3.30), where N is the number of atoms desorbed, m_p is the molecular mass of the particles, $\mathcal{T}$ is the temperature for which desorption occurs, m is the sail mass and t is the time needed for the physical process of thermal desorption to be completed.

For the common graphite, Carbon ^{12}C, the molecular mass is $m_p = 12\,Da = 19.2 \cdot 10^{-27}\,kg$ and its density is $d = 2267\,kg/m^3$, whereas Fullerene C_{60} has $m_p = 720.66\,Da = 1203.5 \cdot 10^{-27}\,kg$ and its density is $d = 1650\,kg/m^3$ [121, 122]. Once the material is known, one can find the number of atoms desorbed:

$$N = \frac{M}{m_p} = \frac{dV}{m_p} = \frac{dHA}{m_p}.$$

Then the number of atoms desorbed per unit area during the time, dN_A/dt, is obtained from (3.19) if the activation energy E_A is known (see Ref. [121, 122]). If the sail area is defined, N_A is fixed, so the required desorption time can be found [123, 124]. However this approach would require very accurate information about the material's characteristics, and the activation energy varies in a wide range and would require ad hoc experiments to have reliable data. For this reason another approach was used: as suggested in Benford's paper [3] a nominal rate of mass loss

was chosen, $dm/dt = 1\ g/s$. For a given sail area A and thickness H or loading factor σ, the mass of the sail is fixed. For example a sail of $A = 3000\ m^2$ and with $\sigma = 1\ g/m^2$ has a mass of $3\ kg$. For each heliocentric distance r_P (to which corresponds a defined temperature $\mathcal{T}$) one can evaluate the mean thermal velocity with Eq. (3.28) that by means of (3.26) provides the acceleration due to desorption. Given a sail coating thickness H_c, the density of the material and the area of the sail, the total mass required for the desorption is obtained, and then the desorption time dividing the mass over the rate of mass loss.

Solution of the Problem

For example, considering an heliocentric distance $r_P = 0.3\ AU$ (to which corresponds $\mathcal{T} = 737\ K$ as shown in Ref. [125]) the mean thermal velocity for Carbon is $1168\ m/s$ and the acceleration due to desorption $0.39\ m/s^2$. If the sail coating thickness is $H_c = 5 \cdot 10^{-6}\ m$ (note that $H_c > H$) the total mass required for the desorption is $M_c = 34\ kg$ (note that $M_c > M$), and the desorption time $34005\ s$ (over 9 hours). Because the mass of the coating is not negligible with respect to the sail mass, and also the desorption time is also relevant, the formula $v = v_0 + a \cdot t$ does not apply. In fact, this analysis cannot neglect the variation of mass during the acceleration time. The force on the sail is:

$$F = \frac{d(M \cdot v)}{dt} = \frac{d}{dt}\left(\sigma A + M_c\right) v = \left(\sigma A + M_c\right) \frac{dv}{dt} + \frac{dM_c}{dt} v, \tag{3.31}$$

whereas the force due to thermal desorption is:

$$F = \frac{dM_c}{dt} v_{th}. \tag{3.32}$$

By comparing these two equations one obtains a differential equation in v:

$$\frac{dv}{dt} + \frac{1}{(\sigma A + M_c)}\frac{dM_c}{dt}v - \frac{1}{(\sigma A + M_c)}\frac{dM_c}{dt}v_{th} = \frac{dv}{dt} + E \cdot v - F = 0, \tag{3.33}$$

that can be solved introducing two constant C_1 and C_2:

$$v(t) = C_1 e^{-Et} + C_2, \tag{3.34}$$

for which the first derivative is:

$$v' = -EC_1 e^{-Et}, \tag{3.35}$$

so one of the constants is:

$$C_2 = \frac{F}{E}, \tag{3.36}$$

$$v(t) = C_1 e^{-Et} + \frac{F}{E}, \tag{3.37}$$

for $t = t_0$ the velocity v_0 is the speed at which the sail is travelling when desorption occurs and depends on the orbital dynamics:

$$v_0 = C_1 e^{-E \cdot 0} + \frac{F}{E} = C_1 + \frac{F}{E}. \tag{3.38}$$

As v_0 is known, the other constant is:

$$C_1 = v_0 - \frac{F}{E}, \tag{3.39}$$

and so the expression of the velocity as a function of time is finally the following:

$$v(t) = \left(v_0 - \frac{F}{E}\right) e^{-Et} + \frac{F}{E}. \tag{3.40}$$

The results of this analysis will be explored in section 6.2.2 for the Solar Sail scenario.

3.6 Focus of This Research

Exploring the outer solar system using solar sail propulsion requires achieving high cruise speeds, which can be facilitated by accelerating the sailcraft in the region near the Sun. In this thesis the main interest is focused on the possibilities of a high-performance sail to escape the Solar System at significant speed by means of thermal desorption of its coatings. The sail's deployment from its stowed configuration allows the heat-sensitive materials to undergo thermal desorption at the perihelion of the heliocentric escape orbit. This mechanism provides an additional acceleration on top of the conventional one due to solar electromagnetic radiation.

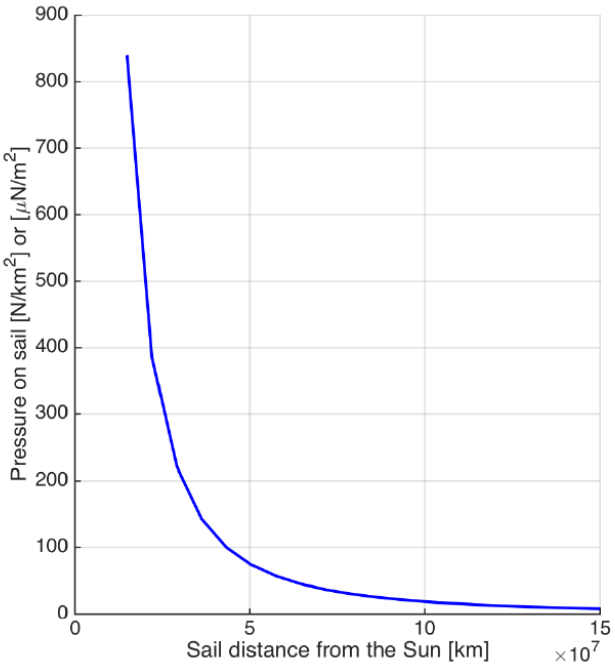

Figure 3.8: Pressure on the sail as a function of the sail distance from the Sun, assuming reflectivity of 0.85.

The efficiency of a solar sail increases as it approaches the Sun because of the

stronger solar radiation pressure, as shown in Fig. 3.8.

Deploying a solar sail close to the Sun maximizes the force exerted by the radiation, enabling higher acceleration and faster cruise speeds. To further enhance this acceleration, we propose utilizing space environmental effects; by coating the solar sail with materials that undergo desorption at elevated temperatures, we can introduce an additional acceleration mechanism [4, 5]. As the sail heats up from solar radiation at a specific heliocentric distance, the coated material desorbs, releasing additional energy that boosts the sail's speed [117]. The conceptual approach developed in Ref. [117] allows the perihelion of the solar sail orbits to be determined based on the temperature requirement for the solar sail materials. In that study, the proposed sail has two coats of the materials that undergo desorption at different solar sail temperatures depending on the heliocentric distance. The first desorption occurs at the Earth orbit and provides the thrust that is needed to propel the solar sail toward the Sun. When the solar sail approaches the Sun, its temperature increases, and the second coat undergoes desorption at the perihelion of the heliocentric escape orbit. This approach undergoes further development and implementation with the author's contribution in Ref. [4] by considering orbital dynamics of a solar sail coated with materials that undergo thermal desorption at a specific temperature, as a result of heating by solar radiation at a particular heliocentric distance, and focus on two scenarios that only differ in the way the sail approaches the Sun: (1) Hohmann transfer plus thermal desorption. In this scenario, the sail would be carried as a payload to the perihelion with a conventional propulsion system by a Hohmann transfer from Earth's orbit to an orbit very close to the Sun, and then it is deployed; (2) Elliptical transfer plus Slingshot plus thermal desorption. Moreover, this study analyses and compares the different scenarios in which thermal desorption comes alongside traditional propulsion systems for extrasolar space exploration.

This effect, combined with the traditional solar radiation pressure, provides an

extra source of propulsion. The perihelion of the solar sail's orbit is selected based on the temperature required for the desorption of the coating material. At this critical perihelion, the sail, that was stowed, is deployed and reaches its maximum temperature, triggering desorption and subsequent acceleration. The sail achieves escape velocity from this process but continues to accelerate further due to the radiation pressure. By leveraging both the increased solar radiation pressure near the Sun and the additional thrust from material desorption, this approach offers a promising method for reaching high velocities, making it highly suitable for missions to the outer solar system and beyond.

A potential factor that has not been considered in this analysis is the effect of Compton scattering caused by the cloud of ionized particles released during the desorption process. As the sail undergoes desorption near the Sun, the emitted material could interact with incoming solar photons, leading to scattering effects that may reduce the efficiency of radiation pressure on the sail. Since scattered photons may not reach the sail at normal incidence, this could introduce a reduction in the effective thrust. While this aspect is beyond the scope of the present work, future studies should investigate the extent of scattering losses and incorporate an appropriate efficiency factor to account for potential thrust reductions.

Chapter 4

The Direct Fusion Drive

This chapter introduces the Direct Fusion Drive (DFD), covering its main characteristics, applications, and associated challenges. Following an introduction to nuclear power and a description of the DFD's unique design features, the chapter explores the potential advantages of this fusion-based propulsion system, such as high efficiency and suitability for long-duration deep-space missions. Possible applications, including both robotic and manned missions, are discussed to highlight the versatility of the DFD. The chapter also addresses the limitations and technical challenges involved in DFD development, including plasma containment and energy management. Finally, it outlines the specific aspects of the DFD that this research aims to investigate in greater depth, establishing the foundation for the studies in the subsequent chapter.

4.1 Nuclear Power

Nuclear power is primarily obtained by releasing the strong nuclear interaction through fission and fusion reactions. From an engineering point of view, fission reactors are easier to build than fusion reactors and, for this reason, since the 1950s, they found application in power plants that produce electricity, as well as in propulsion. In these systems, the power required by the thermodynamic cycle

comes mainly from the kinetic energy of the fission products, which are confined in the fuel. This energy is converted into heat through friction, heating the fuel itself. The fission of a single Uranium-235 nucleus typically produces around 200 MeV of energy. Fusion reactors are still under development, and the most efficient reaction in terms of the lowest temperature required and the highest energy release is the deuterium-tritium fusion. To achieve this reaction, matter must be in a plasma state, with temperatures reaching hundreds of millions of Celsius degrees. A specific reaction, one of the most important, involves deuterium and tritium nuclei: this reaction produces Helium-4 nuclides and a neutron with kinetic energy of around 15 MeV. Because this neutron can escape from the plasma, its energy is collected by a blanket through friction, which increases in temperature while diffusing heat to a cooling circuit.

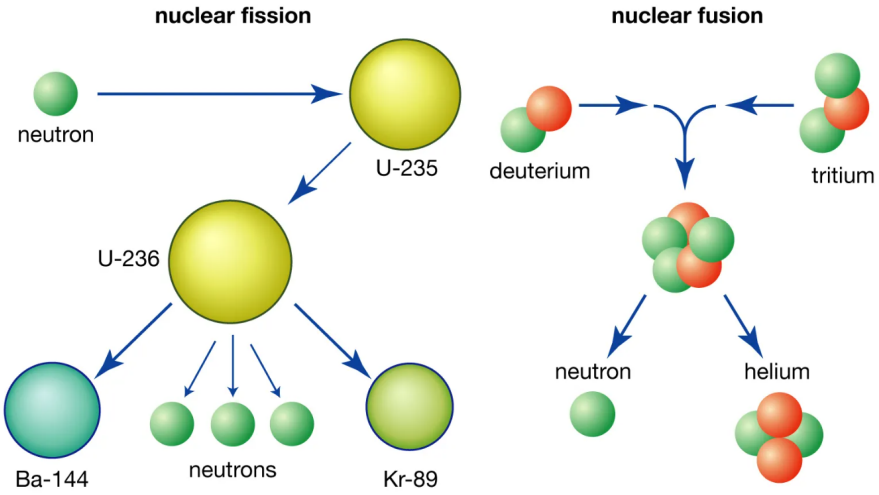

Figure 4.1: Nuclear fusion and fission events. Credit: Merriam-Webster Inc.

There are two main aspects that make fusion reactors technologically more challenging and costly. First, in fission reactors, particles need to be slowed down to maximize the probability of undergoing a fission event in the fuel, while fusion reactors require particles to be accelerated using force fields or heat. Slowing down particles is easier and cheaper to achieve, as it simply involves allowing them to

interact with matter. Conversely, particles in plasma must reach the necessary temperature conditions to initiate the desired reaction, which requires introducing a significant amount of energy into the system. Secondly, fission is a chain reaction process that can be easily self-sustaining so, in other words, it requires no external action. This is due to the neutron balance, as one fission of a heavy nuclide typically emits two or three new high-energy neutrons which, in turn, will produce new fission events. To achieve a self-sustaining fusion reaction, one must consider energy economy instead. When the rate of energy production exceeds the rate of energy loss, the system will produce net energy. If enough of that energy is captured by the fuel, the reaction can be maintained, and the system is said to be ignited. This energy balance strongly depends on the confinement of the plasma, which is crucial to prevent it from cooling down and losing energy, while also isolating it from any surrounding component that cannot withstand these extreme conditions. In Ref. [48] Long thoroughly explores the application of inertial confinement fusion physics to advanced spacecraft propulsion for deep space missions.

A plasma can be modeled as an ionized gas that obeys the magnetohydrodynamics (MHD) equations, which combine Maxwell's equations for electromagnetic force fields and Navier–Stokes equations for fluid dynamics [126]. The latter can be derived from Boltzmann's kinetic theory, which describes the evolution of particle distributions in a system. However, this description is often not enough information, and the so-called kinetics approaches are used instead, where the kinetics of single particles is described at a more microscopic level. These approaches are based on the Boltzmann equation, describing the collisional behaviour of particles colliding with each other; this introduces a non-linear term related to particle distribution. The solution of this equation is challenging and computationally expensive. In practice, it is often substituted with simplified kinetic models, where, for instance, the term depends linearly on the particle distributions, aiming to provide useful approximations for macroscopic quantities such as mass, momentum, and energy.

The linearized transport model remains a complex equation to solve, and Monte Carlo methods are generally employed as powerful tools to find solutions. Particle transport theory and the computational methods associated with it are discussed in Chapter 5 where it will be described a method to deal with the actual kinetics of charged particles in a magnetized plasma strongly reducing the computational requirements while retaining the advantages of a kinetic approach.

4.2 Nuclear Fusion

The fusion mechanism is based on the merging of light elements, mainly hydrogen (H) with its neutron-free, most common isotope protium, and its neutron-bearing isotopes deuterium (D) and tritium (T). The protium nucleus consists of a single proton, the deuterium nucleus has one proton and one neutron, while tritium has one proton and two neutrons. A fusion reaction is possible if two light nuclei merge into a nucleus below an atomic mass of 56. Due to the increase in binding energy, the final state is more stable. The difference of mass (Δm) between the initial and final states is transformed into energy (E) according to Einstein's relation: $E = \Delta m \cdot c^2$.

A fusion reaction can typically be written as:

$$ {}^{a}_{b}\mathrm{X} + {}^{A-a}_{B-b}\mathrm{Y} \rightarrow {}^{A}_{B}\mathrm{Z} + Q, $$

where A,a represent the mass number (protons and neutrons), B,b the atomic number (protons) for the elements X,Y,Z, $Q > 0$ is the energy released and it is given by:

$$ Q = [(m_X + m_Y) - m_Z] \cdot c^2. $$

Since nuclear interaction is a short-range interaction, this process can be obtained only if the two nuclei involved have enough kinetic energy to overcome the Coulomb barrier. Studies of nuclear properties of light elements indicate that three reactions may be more advantageous for the production of energy [127]: D-D, D-^{3}He and D-T, whose nuclear structures are given in Fig. 4.2.

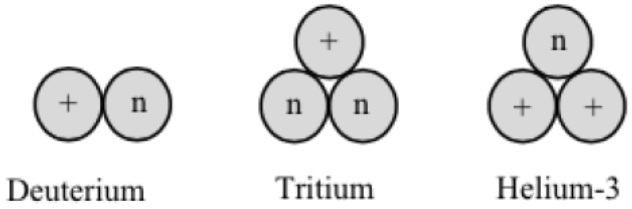

Figure 4.2: Nuclear structure of the basic fusion fuels.

The D-D reaction

$$D + D \rightarrow {}^3\mathrm{He} + n + 3.27\,\mathrm{MeV},$$

$$D + D \rightarrow T + p + 4.03\,\mathrm{MeV},$$

where n and p are neutrons and protons released. These two reactions (each occurring with approximately equal probability) are more difficult to initiate with respect to the D-T, but the main advantage is that D is available in ocean water. In fact, there is one atom of deuterium per 6700 atoms of hydrogen.

The D-^{3}He reaction

$$D + {}^3\mathrm{He} \rightarrow \alpha + p + 18.3\,\mathrm{MeV}.$$

The energy produced per reaction is impressive but there are no natural supplies of He^3 on Earth.

The D-T reaction

$$D + T \rightarrow \alpha + n + 17.6\,\mathrm{MeV}.$$

The main advantage is that this reaction occurs at a faster rate, but there is no natural tritium on Earth since this nuclide is unstable and decays with a half-life of 12.3 years.

Reaction	Ignition T (MK)	Energy Yield (MeV)	Neutron Prod.
D-D	∼300	3.3–4.6	Moderate
D-T	∼150	17.6	High
D-^{3}He	∼500	18.3	None (direct)

Table 4.1: Comparison of Nuclear Fusion Reactions: ignition temperatures, energy yield per reaction and neutron production.

Reaction	Fuel Availability	Main Challenges
D-D	High (seawater)	Lower efficiency, neutron radiation
D-T	Low (requires lithium breeding)	Neutron damage, tritium scarcity
D-^{3}He	Extremely rare	High ignition temp, fuel scarcity

Table 4.2: Comparison of Nuclear Fusion Reactions: fuel availability and main challenges.

Comments D-D reactions are promising candidates for fusion because they produce charged particles that can be retained within the reactor. This helps offset energy losses and maintain the required high temperatures. Even more favorable is the deuterium-tritium (D-T) reaction, mentioned before, which has a Coulomb barrier similar to D-D but a larger cross section. Additionally, the D-T reaction releases significantly more energy, as one of the products is the tightly bound alpha particle, resulting in an energy yield about four times higher than uranium fission. However, it relies on tritium as a fuel, which as mentioned is radioactive. Therefore it must be produced within the fusion reactor due to its scarcity in nature.

For both D-D and D-T reactions, the private company Deutelio is suggesting a poloidal confinement method to achieve more efficiency and better performance, the Polomac [128]. In this system the outboard magnetic lines are deviated aside together with the plasma, to open some accesses to the dipole coils located inside the plasma. These accesses, called magnetic tunnels, are used to support, feed and

cool the dipole coils. The magnetic tunnels avoid the impact with plasma which led to the abandonment of past poloidal experiments, despite their good stability and confinement efficiency.

The D-^{3}He reaction is appealing since it has a high energy release (Q-value) and produces only charged particles (making it aneutronic). This allows for easier energy containment within the reactor and avoids the neutron production associated with the D-T reaction, which contributes to radioactivity. However, the D-^{3}He reaction faces the challenge of a higher Coulomb barrier, requiring a reactor temperature approximately six times greater than that of a D-T reactor to achieve a comparable reaction rate. Moreover, a major challenge for this reaction is the scarcity of ^{3}He resources on Earth.

Although ^{3}He is a stable nuclide that is immune to natural chemical processes and is continually produced by the Sun, its abundance on Earth is extremely low - around 1/10,000 that of ^{4}He. The ^{3}He available is not only limited but also very costly to produce, as it can only be obtained through the radioactive decay of tritium (which has a half-life of 12.3 years) generated in nuclear fission reactors. Since 1955, only about 150 kg of non-radioactive ^{3}He has been produced in the United States, and currently, there are only about 30 kg of ^{3}He in human possession [129].

One potential solution is to tap into ^{3}He resources found elsewhere in our Solar System. The lunar surface, for instance, contains ^{3}He deposits from the solar wind, making it a nearby and relatively accessible source. Numerous studies have explored the economic feasibility of mining ^{3}He on the Moon, assessing both the energy costs of extraction from lunar soil and the potential financial returns [130].

Other sources could include the helium-rich atmospheres of gas giants such as Jupiter, Saturn, and Neptune [129].

Conclusions

- D-T fusion is the most promising for near-term energy production due to its lower ignition temperature and high energy output, despite neutron radiation issues.
- D-D fusion is attractive due to fuel abundance but suffers from high neutron production and lower energy output.
- D-^{3}He fusion is ideal for future space propulsion and clean energy due to its aneutronic nature, however the challenges of high ignition temperature and fuel scarcity make it impractical in the short term.

For space propulsion, D-^{3}He fusion is highly desirable due to its efficiency and clean energy output, but D-T fusion remains the most viable in the near future due to existing technological advancements.

4.3 DFD Engine Characterization

The Direct Fusion Drive is a D-^{3}He-fueled, aneutronic, thermonuclear fusion propulsion system that is under development at Princeton University Plasma Physics Laboratory [1]. It produces both propulsion and electrical power from a compact fusion reactor. Funded by NASA and based on the Princeton Field Reversed Configuration (PFRC) fusion experiment [131], DFD is designed for various space missions, including crewed and robotic missions to Mars, and cargo missions to the outer solar system. The second generation machine (PFRC-2) uses a unique radio frequency plasma heating method, known as "odd-parity heating", to increase plasma temperatures for fusion [131, 132]. The technique relies on a magnetic field structure that maintains plasma confinement, crucial for achieving optimal fusion conditions. This configuration ensures stable plasma behaviour, making it more resilient to instability than other fusion devices [133].

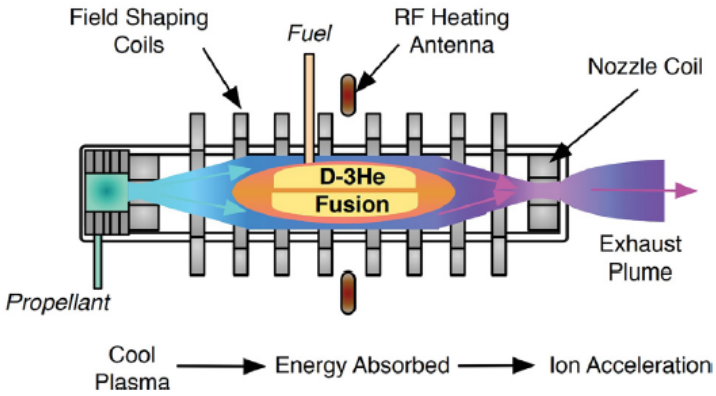

Figure 4.3: Schematic diagram of the Direct Fusion Drive (DFD) engine subsystems. Credit: Cohen et al. [1].

A diagram of the DFD is provided in Fig. 4.3. Fusion occurs in the Closed Field Region (CFR). Propellant is added in the gas box where it is ionized; the plasma then flows along field lines in the open-field-line region and across the separatrix surface of the CFR where its electrons are heated. The propellant ions are accelerated axially as they pass through the nozzle coil.

The field-reversed configuration (FRC) is a distinctive magnetic field geometry that was discovered by accident in θ-pinch machines in the 1960s: a toroidal electric current is induced within a cylindrical plasma, generating a poloidal magnetic field that is reversed relative to an externally applied magnetic field.

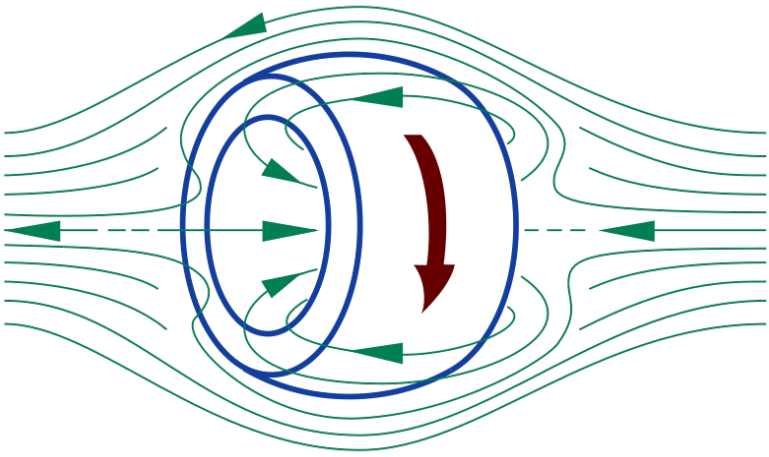

Figure 4.4: The field-reversed configuration (FRC). Credit: [134].

Indicating with β_{MF} the ratio of plasma pressure to magnetic-field energy density, this setup creates a high-β_{MF}, axisymmetric, compact toroid, as conceptually shown in Fig. 4.4, which is self-confined by diamagnetic ion currents. Key features of the FRC include the absence of a significant toroidal field, a β_{MF} value around unity, no rotational transform, and a self-sustaining equilibrium current via diamagnetism. A scrape-off layer (SOL) . The lack of a toroidal field in FRCs greatly reduces problems related to instabilities.

The core region, where fusion reactions occur, consists of high-temperature (about 100 keV), moderate-density ($5 \cdot 10^{14}\,\mathrm{cm}^{-3}$) plasma [135]. In the Field Reversed Configuration (FRC), this core lies within the magnetic separatrix, an imaginary closed surface that separates open magnetic field lines - those extending outside the device - from closed magnetic field lines that remain entirely contained. The region with open field lines is also known as the scrape-off layer (SOL), exhausting heat and particles outside the coil system. To form closed magnetic field lines, a strong plasma current perpendicular to the FRC's magnetic field is essential. Along the central axis, the magnetic field direction generated by the plasma current opposes the external field lines produced by surrounding coils. According to MHD theory [136], any misalignment between these field axes would result in a significant tilt and eventual destabilization of the configuration. However, Cohen and Milroy demonstrated that adding an antisymmetric magnetic field about the axial midplane can help maintain the closed field line structure in the FRC [132].

Fuel Selection and Neutron Production Neutron production in fusion reactions poses significant challenges for spacecraft propulsion. Neutrons can damage and activate nearby materials and structures, which limits their lifespan, increases maintenance needs, and necessitates additional shielding, adding to the system's overall mass. Unlike charged particles, neutrons are difficult to control within magnetic devices, as they do not interact with electric or magnetic fields. To address

this, reducing neutron fluxes is essential. Looking at the reactions presented in section 4.2, the D-^{3}He is an aneutronic fusion reaction:

$$ {}^2_1\mathrm{D} + {}^3_2\mathrm{He} \rightarrow {}^4_2\mathrm{He}\,(3.6\,\mathrm{MeV}) + p\,(14.7\,\mathrm{MeV}). \tag{4.1} $$

Nevertheless, it is not the only fusion reaction that can take place. In fact, the following side reactions can also occur:

$$ {}^2_1\mathrm{D} + {}^2_1\mathrm{D} \rightarrow {}^4_2\mathrm{He} + \gamma + 23.85\,\mathrm{MeV}, \tag{4.2} $$

$$ {}^2_1\mathrm{D} + {}^2_1\mathrm{D} \rightarrow {}^3_2\mathrm{He}\,(0.82\,\mathrm{MeV}) + n^0\,|\,(50\%), \tag{4.3} $$

$$ {}^2_1\mathrm{D} + {}^2_1\mathrm{D} \rightarrow {}^3_1\mathrm{T}\,(1.01\,\mathrm{MeV}) + p\,(3.02\,\mathrm{MeV})\,|\,(50\%), \tag{4.4} $$

$$ {}^2_1\mathrm{D} + {}^3_1\mathrm{T} \rightarrow {}^4_2\mathrm{He}\,(3.49\,\mathrm{MeV}) + n^0\,(14.1\,\mathrm{MeV}). \tag{4.5} $$

In other words, choosing D-^{3}He helps to minimize neutron production but it does not completely prevent their creation. D-D side reactions generate a small number of moderate-energy neutrons and some tritium. If this tritium then fuses with deuterium, it produces high-energy neutrons that can be highly damaging. The compact size of the device allows for quick removal of tritium "ash," effectively preventing these harmful deuterium-tritium side reactions. Neutron production is further minimized by adjusting the fuel mix to contain three times as much ^{3}He as deuterium, achieving a 3:1 ratio that favours ^{3}He reactions. This significant reduction in neutron production greatly reduces the mass required for shielding, benefiting the overall engine design.

Technical Challenges

The fusion reaction of nuclei of deuterium (D) and tritium (T) is the most promising for the energy produced. However, D–T fuel is not ideal for the DFD, due to the significant emission of neutrons. When neutrons are generated in fusion reactions, part of the energy becomes unusable, causing energy losses and neutron emissions that can contaminate the spacecraft. To protect the spacecraft (and the crew, if present) shielding is necessary since neutrons, being uncharged, cannot be controlled by electric or magnetic fields. Reducing neutron flux is crucial to minimize material damage and radiation but would also increase the mass needed for radiation shielding. For these reasons, aneutronic fuel, such as a deuterium and ^{3}He mixture, discussed in the previus section, is preferred. This choice addresses the issue of neutron production, however the DFD - like every cutting-edge technology - holds avenues for improvement. A detailed review of the initial concept and suggestions for modifications were provided by Jain et al. [137]. For example, replacing the conventional turbine and radiator system with a MHD generator could reduce complexity, mass, and maintenance requirements on long deep-space missions. Further considerations and ongoing research on this topic are available online; we will not expand on the subject that is beyond the scope of this work.

4.4 Main Advantages and Possible Applications

As mentioned in section 2.2, the advantage in using nuclear energy in space propulsion is related to the very high temperatures that can be obtained, leading to large expansion velocities and consequently much higher values of specific impulse, compared to those of a chemical propulsion.

With a power range of 1 to 10 MW, depending on mission-specific requirements, the DFD demonstrates versatility for a variety of use cases. Characteristics for low and high power configurations of the engine are listed in Table 4.3. In previous

collaborations, the authors of this study have identified potential applications for the breakthrough technology. While a broad overview of its capabilities to provide the required mobility even for human planetary exploration is given in Ref. [2], analysis of realistic trajectories for robotic missions to Titan [138], trans-Neptunian objects [139] and other destinations in the solar system [140] have been performed.

	Low power	High power
Fusion Power [MW]	1	10
Specific Impulse [s]	8500-8000	12000-9900
Thrust [N]	4-5	35-55

Table 4.3: DFD characteristics for low and high power configurations [1].

4.5 Focus of this Research

Designing the complete system for use in space requires solving a series of technological challenges and computer modeling problems. For the latter, the necessary simulations include the kinetics and dynamics of the particles of the actual high-temperature core of the system in which the reaction takes place.

This thesis aims to investigate and explore the need for models and experiments that involve aspects of low-temperature or moderate-temperature plasmas that must necessarily be understood much better before a prototype can be produced that can be used in space.

To give a first example, in a real device the plasma cannot be in contact with the reactor materials at the core temperature since no known material can be in a condition other than that of ionized gas at the temperatures reached, not even refractory materials such as oxides or silicates or metals such as molybdenum.

This means that the plasma must have an interface with any solid surface of the system. At this interface, significant cooling must occur and the resulting low-temperature plasma is actually in direct contact with the solid surfaces. This situation is similar to that found in the treatment of materials via plasma or solid

surfaces in contact with the plasma [141]. This leads to a negative potential and ions accelerated by this potential strike the material, producing superficial or deeper modifications since ions can penetrate to different depths in any solid material, especially light ions.

Understanding the behaviour of plasma at moderate temperature in contact with solid surfaces requires a detailed examination of aspects of the transport of charged particles such as electrons and ions, which will have a very different behaviour due to their very different mass: in particular electrons can be magnetized and therefore move in a Larmor spiral with magnetic fields much less intense than those that magnetize the ions [142]. It is necessary to develop reliable numerical simulation methods for the behaviour of charged particles in the presence of electric and magnetic fields and collisions with positive ions and neutral particles. As is known from collisional plasma physics this problem is not simple [143].

Another application that justifies a significant effort in this direction is the already well-tested possibility for large-scale fusion experiment actors to additionally heat the plasma using neutral particle beams obtained by neutralization of charged particle beams with the same composition as the reactor plasma [144].

Optimization of these reactor operation support devices requires low-temperature collisional plasma simulations to describe, in particular, the primary ion source.

At the same time this aspect of technological development is interesting and consistent with the ideas developed in this thesis since, as in the case of solar sail enhancements, the required skills are essentially in the field of kinetic theory of gases.

As an important part of the thesis work, an advanced model for the transport of charged particles, both electrons and ions, in a collisional plasma gas at high temperature and subjected to a magnetic field has been developed: the details of this study and its results are reported in the following chapter.

Chapter 5

Transport of Particles for DFD

This chapter delves into the particle transport processes that are critical to the function of the DFD. Starting with an overview of particle transport in matter, the chapter explains the methodologies used to model particle behavior within the DFD environment. The Monte Carlo (MC) method is introduced as a foundational simulation technique, followed by the Monte Carlo Flux (MCF) method, an advanced approach used for variance reduction and faster computations. Results from MCF simulations are presented, including verification for electron transport in ideal gases and applications to both magnetized electron and ion transport. The chapter concludes with insights into the strengths and limitations of the MCF method, setting the stage for its use in more complex DFD simulations.

The fusion propulsion described in the previous chapter and its design variants require significant development and progressive improvements, which can be assisted by computer simulations. An essential subject of these simulations is the prediction of the transport of charged particles in an ionized gas. The simulation of an ionized gas at moderate temperature can be helpful in two cases: one is the improvement of the interface between the high-temperature zone and the solid materials from which the propulsion system is necessarily built, the other is the development of nuclear reactor assist technologies such as neutral injection and ion beam production. All these cases require accurate transport simulations that take

into account collisions between charged and neutral particles and the presence of strong magnetic fields. Furthermore, the efficient simulation methods of electron and ion transport in a magnetized gas that have been developed within this thesis can certainly also be applied to the optimization and numerical design of electric plasma thrusters of the type described in the chapter on propulsion systems.

After running some initial Monte Carlo simulations of electrons in ideal gas model, validated against analytical solutions, an additional technique has been used in this thesis for variance reduction of MC simulations, to quicken the calculations: the Monte Carlo Flux method. The MCF provides a partition of the velocity space, in order to describe the kinetics of the free electrons by means of a probability balance equation, in which the transition frequencies are calculated with a large number of short-time Monte Carlo simulations. This method provided a reduction of the computational time up to several dozen times compared to conventional MC simulations. Detailed and accurate databases of cross sections of elementary processes for electrons in molecular deuterium gas were used; in addition, the effects of combined electric and magnetic fields on the electron distribution function is investigated. Finally, the MCF method has been extended to study ion transport in gases under the effect of electric and magnetic fields. The thesis presents the first application of MCF to H^+ ions in H_2 gas. The results presented in this thesis are of relevant interest for primary systems support technologies, in particular for ion sources and for plasma diagnostics in fusion reactor prototypes.

The past few years have witnessed a growing interest in the study of the kinetics and transport of electrons in low-temperature plasmas, particularly those dominated by collisions between electrons and neutral particles under the influence of magnetic fields [145, 146, 147, 148, 149]. This interest stems from the broadening applications of ionized gases influenced by magnetic fields in various areas, ranging from gaseous electronics to auxiliary systems in fusion reactors, and the development of plasma support systems for deep space navigation [150, 151].

As regards the development of nuclear fusion technology, a low-temperature partially-magnetized plasma is found in the neutral beam injector system for the ITER project [152, 153, 154]. In fact, in the RF drivers of these deuterium-based inductive discharges, magnetic fields are used to reduce electron losses at the walls. Moreover, in the expansion region, a transverse magnetic field is generated with the aim of preventing hot electrons from reaching the extraction region and thus effectively neutralizing the negative ions [155]. Other systems of interest for fusion technology in which the plasma is found in non-equilibrium conditions are the scrape-off-layer (SOL) and the divertor region of thermonuclear fusion reactors [156, 157, 158, 159].

Magnetized plasma has also gained high interest in recent years for its use in the framework of spaceflight propulsion.

Plasma is also considered as an option to generate thrust in other innovative concepts, including those based on nuclear propulsion [160]. For example, in the DFD presented in Chapter 4, the plasma is confined in a torus-like magnetic field inside of a linear solenoidal coil, being then heated to relevant fusion temperatures by a rotating magnetic field [1]. The DFD has already been indicated as a potential disruptive machine that would help us achieve the required mobility in the solar system [2]. However, some challenges remain on the path to operational readiness. Being able to determine with the highest possible accuracy the behavior of particles under the influence of electric and magnetic fields becomes pivotal in advancing the current status of cutting-edge technologies like these, enabling us to reach goals that only a few decades ago would have been inconceivable.

Magnetron sputtering is another significant application of partially-magnetized discharges, extensively utilized in thin-film deposition technologies [161]. This technique employs a magnetically confined plasma to enhance the efficiency of material ejection from a target surface, typically a metal or ceramic, onto a substrate. By placing magnets behind the target, the electrons are trapped in a magnetic field,

increasing their collision frequency with the neutral gas and thereby sustaining a higher plasma density. This results in a more efficient sputtering process, allowing for uniform coating of complex geometries with controlled film properties.

The kinetics of low-temperature, weakly-ionized plasmas, such as those found in the applications described above, is an intensively studied topic [162]. Optimal theoretical and numerical methods have been developed for these systems and, with the recent focus on the role and effects of static magnetic fields on these systems, previously developed methods are being reconsidered. The most widely used charged particle simulation technique is the Monte Carlo (MC) simulations method, known for its flexibility in accounting for various collisional processes together with external electric fields [163, 164, 165]. It is particularly straightforward to incorporate the magnetic component of the Lorentz force into electron and ion dynamics using this method [166, 167]. Moreover, the MC method is also used in self-consistent simulations of plasmas within the Particle-In-Cell with Monte Carlo Collisions (PIC/MCC) method [168]. However, MC simulations are also characterized by significant statistical fluctuations in the computed distribution functions. These fluctuations are particularly important for the high-energy part of the distribution function, which is crucial for calculations of atomic and molecular excitation and ionization rate coefficients. To address this issue, the most effective way is to rely on the deterministic solution of the Boltzmann transport equation in the two-term or multi-term approximation [169, 170, 171, 172, 173]. Although recent studies have highlighted limitations of the two-term approximation when magnetic fields are applied to plasma [145], deterministic techniques offer the advantage of eliminating statistical fluctuations, leading to complete repeatability and uniform accuracy across the energy range. The primary limitation of deterministic techniques is their complexity, particularly in the theoretical formulations and implementation of efficient algorithms for numerical solutions of coupled systems of partial differential equations [174, 175]. Furthermore, despite the two-term theory

is widely used for description of electron kinetics in gases and plasmas under hydrodynamic regime [176], the description of ion kinetics under two-term expansion of the velocity distribution function fails due to the large ion-to-neutral mass and a multi-term description for the ion Boltzmann equation becomes cumbersome [177].

To overcome these challenges, in this work, we propose a hybrid stochastic and deterministic method known as the Monte Carlo Flux (MCF). Originally conceived by Schaefer and Hui in the early 90s [178], the MCF has seen limited application in subsequent years, but it has recently sparked renewed interest [179, 180, 26, 181]. This hybrid technique offers several advantages, among which (*i*) a significant savings in computational time compared with conventional MC simulations and (*ii*) a deterministic calculation of the diffusion regime which guarantees uniform accuracy for calculations of the VDF. Despite these advantages, the MCF method has only been applied to electron transport under DC electric field and its applicability to a wider range of conditions that are relevant for plasma modelling and simulations still has to be determined. In this chapter, for the first time, we aim to (*i*) verify the applicability of MCF for electron transport under electric and magnetic fields, and (*ii*) to extend the method for magnetized and non-magnetized ion transport in gases. These extensions are a step forward towards integration of MCF within self-consistent plasma simulations.

The chapter is organized as follows. In Section 5.4, the MCF method and its numerical implementation are introduced. In Section 5.5.1, the application of MCF for electron transport in model gas under electric and magnetic fields is shown. In Section 5.5.2, the MCF method is applied to electrons in molecular deuterium (D_2) under electric and magnetic fields using a large set of collision processes and corresponding cross sections. In Section 5.5.3, the applicability of MCF for H^+ ions in molecular hydrogen H_2 under external electric and magnetic fields is shown. Advantages and disadvantages of the method are summarized in the conclusions.

5.1 Transport of Particles in Matter

Transport theory describes the statistical nature of the interactions between particles and matter. The quantitative and qualitative behaviors of these interactions allow us to determine the effect of matter on the propagation of particles and, vice-versa, the effect of particles on the properties of the matter. As mentioned earlier, a common mathematical model for particle transport is provided by the Boltzmann transport equation which, based on a statistical mechanics approach, allows us to "bridge" macroscopic physical quantities of a system to microscopic ones that fluctuate around an average. These quantities are, for instance, the average particle density in phase space, as well as reaction rates experienced by the matter. We revisit the reference [182], to which the reader is referred for more details.

The phase space contains all possible states that particles can have in the system, and it is generally the product of the position space, containing the position vectors $\mathbf{r}$ with respect to a reference frame, and the momentum space, containing the momentum vectors $\mathbf{p} = m\mathbf{v}$. Particles interact with matter according to the microscopic cross section $\sigma_{\alpha,i}$, that is defined as the probability that a specific event, or reaction α, occurs when particles interact with an isotope i. The dimension of σ is an area and it is often interpreted as the quantity that expresses, figuratively speaking, "how large the target is seen by the incident particle". The bigger, the more chances they will interact to produce a reaction. When a target material is a mixture of different isotopes i with atomic density N_i, it is practical to use a quantity that includes all of them, that is called macroscopic cross section Σ_α and it is defined as:

$$\Sigma_\alpha = \sum_i \Sigma_{\alpha,i} = \sum_i \sigma_{\alpha,i} N_i. \tag{5.1}$$

The dimension of the macroscopic cross section [cm^{-1}] represents the probability per unit path for a particle to undergo reaction α in a material. The sum over all reactions provide the total macroscopic cross section.

Because this nuclear data of the matter are tabulated in energy, it may be advantageous to split the momentum space into an angular space and an energy space. The former contains the vectors $\mathbf{\Omega}$ defined in the unit sphere, where $\mathbf{\Omega} = \mathbf{p}/p$ is the solid angle describing the direction of the particle streaming, while the latter is a scalar space defined such that $E \in (0, \infty)$, where E is the particle energy that equals $p^2/(2m)$. The particle density $n(\mathbf{r}, \mathbf{\Omega}, E, t)$ can be defined as the distribution of the number of particles in the phase space and a function of time. In order to determine the number of events, it is useful to know the total distance traveled in one second by all particles contained in an element of the phase space $d\mathbf{r}d\mathbf{\Omega}dE$. This quantity is called *angular flux* and it is equal to the product of the particle density and the module of their average velocity:

$$\psi(\mathbf{r}, \mathbf{\Omega}, E, t) = v(\mathbf{r}, E)n(\mathbf{r}, \mathbf{\Omega}, E, t), \tag{5.2}$$

and, for physical constraints, it is non-negative in any point $(\mathbf{r}, \mathbf{\Omega}, E)$ of the phase space. The number of reactions per unit time and unit volume experienced by the matter, is the result of the contributions of all the particles coming from any direction and with at all energies, thus the reaction rate can be determined as follows:

$$\tau_\alpha(\mathbf{r}, t) = \int_0^\infty \int_{4\pi} \Sigma_\alpha(\mathbf{r}, E)\psi(\mathbf{r}, \mathbf{\Omega}, E, t)d\mathbf{\Omega}dE. \tag{5.3}$$

The linearized transport equation for neutral particles, that is with no force fields, is constructed by imposing balance of particles in each point of the phase space $(\mathbf{r}, \mathbf{\Omega}, E)$, yielding:

$$\begin{aligned}\frac{1}{v(\mathbf{r}, E)}\frac{\partial\psi(\mathbf{r}, \mathbf{\Omega}, E, t)}{\partial t} = &- \mathbf{\Omega} \cdot \nabla\psi(\mathbf{r}, \mathbf{\Omega}, E, t) - \Sigma(\mathbf{r}, E)\psi(\mathbf{r}, \mathbf{\Omega}, E, t) \\ &+ \int_{4\pi} d\mathbf{\Omega}' \int_0^\infty dE'\, \Sigma_{\mathrm{p}}(\mathbf{r}, \mathbf{\Omega}' \to \mathbf{\Omega}, E' \to E)\psi(\mathbf{r}, \mathbf{\Omega}', E', t) \\ &+ S(\mathbf{r}, \mathbf{\Omega}, E, t).\end{aligned} \tag{5.4}$$

In the last equation, the left-hand side describes the variation in time of the particle population, while the right-hand side contains all the events that contribute to particle emission and loss in a volume of the phase space. Specifically, the space-derivative term ($\mathbf{\Omega}\cdot\nabla\psi$) represents the loss of particles due to their motion, and the collision term ($\Sigma\psi$) is the loss due to the particle disappearance from the phase, with Σ the total cross section. This behavior, in fact, can be due to any kind of interaction with the matter, as the particle will eventually be absorbed by a nuclide or scattered to another phase. The integral term is the transfer kernel that accounts for all reactions with probability Σ_{p} that any particle in the phase $(\mathbf{r}, \mathbf{\Omega}', E')$ produces new particles in $(\mathbf{r}, \mathbf{\Omega}, E)$. This can be due, for instance, to the scattering, spallation, or fission events. The first one differs from the last two in the fact that particles are only transferred to a new phase, while the last two actually produce a certain number of new particles in the system. Finally, S is an external source of particles which does not depend on the angular flux. Because the linear transport equation in the integro-differential form is a first-order differential equation with respect to space and time, it requires one initial condition and one boundary condition, which is generally set as zero-incoming angular flux at the boundary.

An analytical solution of the Boltzmann equation is rarely possible, and numerical methods need to be employed. There are essentially two classes of methods called deterministic and stochastic approaches.

5.2 Methodology Overview

The deterministic approach requires the discretization of the whole problem phase space for which the discretized transport equation is solved. This means that a deterministic solution is found most of the time also in "regions" of the phase space that might not be useful in engineering applications. Also, here it is indispensable

that the domain discretization is fine enough to guarantee both the stability of a numerical method and the precision of the solution, that should not be affected by truncation errors. Particular attention is given to the discretization of the energy domain, the so called multigroup formalism. A deterministic solver has, first of all, to process and condense the continuous energy-dependent cross sections into a set of effective values. These values should be determined to accurately represent $\Sigma(E)$, which is a sharp functions in energy for nuclides exhibiting resonant behavior. The deterministic approach allows to run fast transport calculations, making it preferable when the system's physics is well understood and a large number of calculations are needed for problem analysis.

The stochastic approach, instead, uses Monte-Carlo methods to simulate the history of each particle in the system and determine estimates of fluxes and reaction rates in the phase space. The Monte Carlo solution is approximation-free, in the sense that it does not require any discretization of the transport equation. The trade-off is that the solutions are random variables, and the statistical uncertainty on the estimates is inversely proportional to the square root of the number of particle histories. This means that convergence is typically slow: halving the statistical uncertainty requires sampling four times as many histories. It follows that the method can be time-consuming, with run-times that might not be practical. Variance reduction techniques have then been applied with the aim to force particles to explore regions of the phase space that give more contribution to the solution, possibly leaving other regions largely unexplored.

5.3 Monte-Carlo Method

The basic principle of the Monte-Carlo method is to follow the random walk of each single particle, from its initial emission until its death by capture or escape outside the system boundaries. The frequency and outcome of the various interactions with

matter that occur during the particle history, are sampled and simulated according to cross sections and collision laws. When the process is repeated for a large number of particles, the results is a detailed simulation of the transport process.
At start, the particle is characterized by its initial position, direction and energy that are sampled using the emission spectrum, angular distribution and position of a source. Next, the free path is sampled along a trajectory, that is the distance traveled by the particle to undergo a collision. With no force fields, these trajectories are straight lines, and the free path is sampled according to the probability density function:

$$p(x) = \Sigma(E)e^{-\Sigma(E)x}, \quad x > 0, \tag{5.5}$$

where $e^{-\Sigma(E)x}$ is the probability to survive at distance x and, $\Sigma(E)$ the probability per unit path to collide. Typically, the procedure of sampling the distance x is carried out by inverting the cumulative density function $P(L)$, and setting it equal to a uniformly distributed random number r generated between 0 and 1 [183]. The cumulative density is defined as follows:

$$P(L) = \int_0^L p(x)dx, \tag{5.6}$$

corresponding to the probability of the random variable x to have a value smaller than L. The condition $P(L) = r$ requires the inversion of eq. (5.6), leading to the following formula for the flight distance between two collisions:

$$L = -\frac{\log(1-r)}{\Sigma(E)}. \tag{5.7}$$

At this point, it is possible to determine the new position of the particle. However, if the system is not homogeneous, the flight has to be split in different volumes and, if x is larger than the distance to the boundary of the initial volume, the particle is first stopped at the volume boundary and the next flight length is then sampled

according to the cross section of the new volume.

At the new sampled position, the interacting nuclide is chosen using a similar inversion approach, with a probability density defined as a step-wise function:

$$p_i = \frac{\Sigma_i(E)}{\Sigma(E)}, \tag{5.8}$$

with Σ_i the macroscopic total cross section of isotope i. Finally, the reaction type is sampled with probability:

$$p_{\alpha,i} = \frac{\sigma_{\alpha,i}(E)}{\sigma_i(E)}, \tag{5.9}$$

with σ the microscopic cross section of reaction α for the isotope i. Depending on the interaction, the particle can be absorbed and thus removed from the balance, or scattered to another phase. The new direction and energy are sampled according to the scattering cross section $\sigma_{s,i}(\mathbf{r}, \mathbf{\Omega}' \rightarrow \mathbf{\Omega}, E' \rightarrow E)$. A new trajectory is then determined leading to the next collision, and so on, until the job is terminated or the simulation stops. Finally, particle contributions are collected if they reach the detectors. The whole process of transporting N particles is repeated for M independent replicas, having a statistical uncertainty on the ensemble average.

5.4 Monte Carlo Flux Method

We propose a method for studying electron and ion transport in weakly ionized gases under electric and magnetic fields which is based on a computationally efficient variance reduction technique. The transport of charged particles is expressed as a discrete-time Markov process. The transition frequencies are determined by Monte Carlo simulations for time scales much shorter than those needed for the relaxation of the velocity distribution function (VDF). This results in a significant reduction of the computational time and statistical fluctuations of the computed VDFs. Results are presented for a model gas and different values of the Hall parameter. The

method is then applied to simulations of electrons in D_2, and H^+ ions in H_2 using state-of-the-art cross sections and different values of externally applied electric and magnetic fields. It is shown that this approach allows one to study the combined effects of electric and magnetic fields on charged particles transport in a notably simple way, without employing spherical harmonic expansion of the VDF.

The model and assumptions underlying the MCF method are described in previous publications [178, 181]. A more detailed comparison of MCF against other methods, such as conventional MC, two-term Boltzmann solver, and multi-term Boltzmann solver, is described in [179, 180]. Furthermore, the method has been recently coupled with detailed plasma chemistry models in [184, 185, 26, 186]. The method used in this work differs in that the particles' dynamics take into account not only the electric field but also the magnetic field. The implementation is based on the rotation of the velocity component perpendicular to the local field, considering the cyclotron frequency.

The schematics of MCF is shown in Fig. 5.1, where the three main steps of the numerical methods are highlighted. In the first step, the velocity space is discretized into equally spaced cells. Then, transition frequencies $p_{i\to j}(\Delta t)$ from velocity space cells are calculated within short-time MC simulations. In each of these collections of simulations, particles (i.e., electrons or ions) are uniformly distributed within a cell of the lattice in the configuration space and a simulation of the duration Δt corresponding to a few collisions is therefore performed [178]. Finally, transition frequencies are collected into a transport matrix which is used to evolve the initial VDF at time t_0 to a final one at time $t_0 + \Delta t$. Alternatively, the stationary distribution can be calculated by solving an eigenvalue problem [179].

In this chapter, a uniform external electric field $\boldsymbol{E}$ is considered, such that $\boldsymbol{E} = (0, 0, -|E_z|)$. Moreover, as a difference with respect to previous works, we also consider the effect of a uniform and constant magnetic field applied in the direction perpendicular of the electric field $\boldsymbol{B} = (0, B_y, 0)$. Under these conditions,

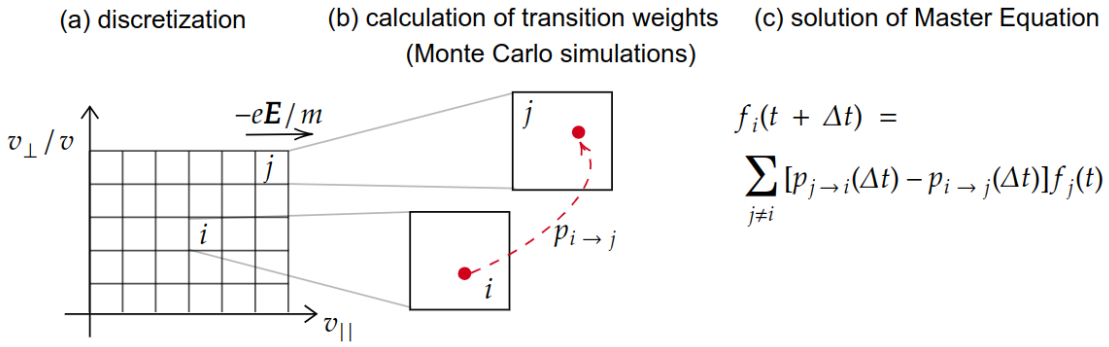

Figure 5.1: The MCF schematics. Figure reproduced with permission from [181].

the velocity space $(\epsilon, \cos\theta)$ is partitioned into cells $C_{i,j}$, with $1 \leq i \leq I$ the index for the energy component and $1 \leq j \leq J$ the index for the angular component. ϵ is the electron kinetic energy and θ is the angle between $\boldsymbol{v}$ and the z-direction. The calculation range is assumed as $0 \leq \epsilon \leq \epsilon_{\max}$ and $-1 \leq \cos\theta \leq 1$, where $\epsilon_{\max}$ is chosen such that we can neglect electron diffusive fluxes to energies higher than $\epsilon_{\max}$. In this way, the energy and angular bin sizes are defined as $\Delta\epsilon = \epsilon_{\max}/I$ and $|\Delta(\cos\theta)| = 2/J$.

In the MCF method, the temporal evolution of the VDF is obtained by a matrix-vector operation, given an initial distribution function at the time $t = 0$. The VDF (for either electrons or ions) at time $t + \Delta t$ is computed as [178]

$$\boldsymbol{f}(t + \Delta t) = \boldsymbol{M}(\Delta t)^\top \boldsymbol{f}(t), \tag{5.10}$$

where $\boldsymbol{M}(\Delta t)$ is the transport matrix of size $IJ \times IJ$ [181]. The elements of the transport matrix are determined by a set of traditional MC simulations starting from each energy interval for a time step Δt, which is chosen as an intermediate between the momentum relaxation times and the energy relaxation times.

More generally, if the reduced electric and magnetic field are fixed for any $t > 0$, the transport matrix remains unchanged and the VDF can be found with an iterative procedure as

$$\boldsymbol{f}(t + n\Delta t) = \left(\boldsymbol{M}(\Delta t)^{\top}\right)^{n} \boldsymbol{f}(t), \tag{5.11}$$

with n the iteration number, and $n\Delta t$ the time-step associated with the n-th iteration. An important consequence of equation (5.11) is that the evolution of the system after Δt is determined only by the state of the system at a time t and it is not affected by the previous history. This is known as the Markov property and allows one to rewrite the linear Boltzmann equation as a simple Markov chain [187]. This reformulation, as will be demonstrated in the following sections of this chapter, results in a significant gain in computation time and reduction of statistical fluctuations in the computed VDFs that are typical of the conventional MC method.

Notoriously, everything comes with a cost: the MCF method has a specific strong limitation compared to others. Due to the deterministic time evolution of the VDF, the charged particles cannot change during the diffusion phase, since the Markov matrix is calculated once and for all. Consequently, the method cannot be used without radical modifications to the systems in which the external fields depend on time. The extension of MCF for time-dependent electric and magnetic fields is left for future work.

5.5 MCF Results

5.5.1 Verification of the Model for Electrons in Ideal Gas

The purpose of the case study presented in this section is to illustrate the proposed procedure. For this reason, the author intentionally preferred to consider a so-called "model gas" - closer to the needs of theoretical physics and statistical mechanics - rather than to those of specific applications. For these calculations, we will therefore consider a background gas of particles with a mass corresponding to that of the

hydrogen molecule and the deuterium molecule (or the helium atom) respectively, that interact solely through elastic collisions with electrons. We also assume that ν_m, the frequency of the elastic collision between the electron and a neutral particle, does not depend on the electron kinetic energy. This hypothesis, which is known to be exact in the case of collisions mediated by a polarization potential [188], is convenient as it enables a precise definition of the Hall parameter.

For the case study, we select an electron-molecule collision frequency $\nu_m = 10^8$ s^{-1}. Assuming a value of elastic momentum-transfer cross-section of 15 $\mathring{A}^2$ [189], this corresponds to a gas pressure of 3 Pa at $T_g = 300$ K. This gas pressure is within the range for magnetically driven processing reactors and for the inductive driver discharge of large-scale negative ions sources, such as those used for ITER [154].

The ratio of the electric field to the momentum transfer collision frequency (E/ν_m) is set to 10^{-7} Vs/m. For the calculations of transition probabilities in MCF, the following values are selected: time step $\Delta t = 10^{-10}$ s, number of particles per cell $N_p = 100$. The time step is chosen such that it is equal to 1/100 of the inverse of the collision frequency. The Boris push algorithm is used to update the velocity of each electron based on the Lorentz force [190]. For the deterministic evolution of the VDF, the number of matrix iterations is 100, number chosen such that enough diffusion on the energy axis is allowed. As an alternative, the stationary solution for the electron VDF can be found by solving an eigenvalue problem [179]. In this calculation, for simplicity, only energy space discretization is applied which limits the method to calculation of the electron energy distribution function (EEDF). This is a limited approach compared to the possibility offered by the method to work with two-dimensional or even three-dimensional cells, but it is consistent with a calculation based on the solution of the Boltzmann equation in the two-term approximation [169]. The extension of the method and results to the velocity space is shown in the next subsection.

The conventional MC simulation is performed with 100 particles sampled in

the course of 10^6 time steps. The applied electric field E is determined from the E/ν_m ratio, while the magnitude of the magnetic field B is determined based on the Hall parameter $\beta = eB/(m_e\nu)$ [189], where e is the elementary charge and m_e the electron mass. Although the magnetic field can be oriented in any direction, the maximum effect is obtained when it is perpendicular to the electric field, therefore this is the configuration that we considered for the test case. In regards to the collision events, the hypothesis is made that the direction of the electron velocity after the collision has a completely isotropic distribution, a hypothesis which is not too far from what actually happens for low-energy electrons in a gas with elastic collisions. In each collision, a fraction of the electron kinetic energy is lost, corresponding to $-2m_e/m_g$ [191], where m_g is the mass of the neutral gas molecule. This expression is correct on average for elastic collisions and can be adopted with confidence given that in these simulations the relaxation of the energy distribution requires hundreds of collisions.

Figure 5.2 shows the EEDF obtained using both conventional MC and MCF methods. In particular, it is is evident that the variance reduction technique employed in MCF is very effective in reducing the statistical fluctuations in the tail of the EEDF, while the overall computational time is lower than for the traditional simulation by about a factor 10.

Figure 5.3 shows the effect of the magnetic field on the stationary EEDFs, as calculated by the MCF method. In particular, for a magnetic field perpendicular to the electric field, a lower EEDF tail is found with increasing Hall parameter β, which is expected given the fact that the rotation of the velocity direction due to the magnetic field hinders the energy gain due to the electric field.

In summary, the results of this case study demonstrate the advantages of the MCF method over conventional MC simulations, particularly in terms of computational efficiency and the reduction of statistical noise in the electron energy distribution function. The ability to capture subtle effects, such as the influence of

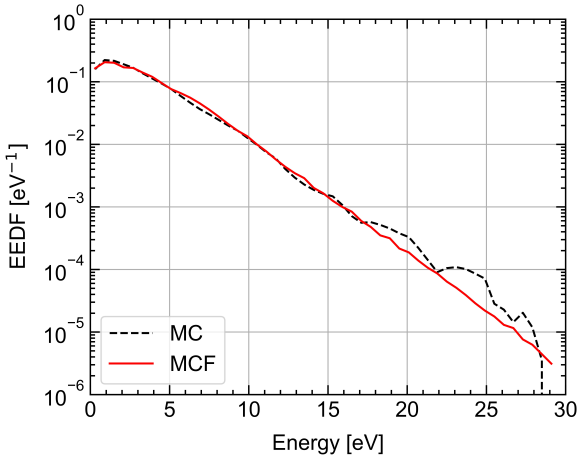

Figure 5.2: Comparison of MC (dashed black line) and MCF (red line) results for electron energy distribution function in ideal gas (4 AMU) model obtained for $E/\nu_m = 10^{-7}$ V s/m. The plots demonstrates the reduction of the statistical fluctuations in EEDFs obtained with MCF compared to the conventional MC method.

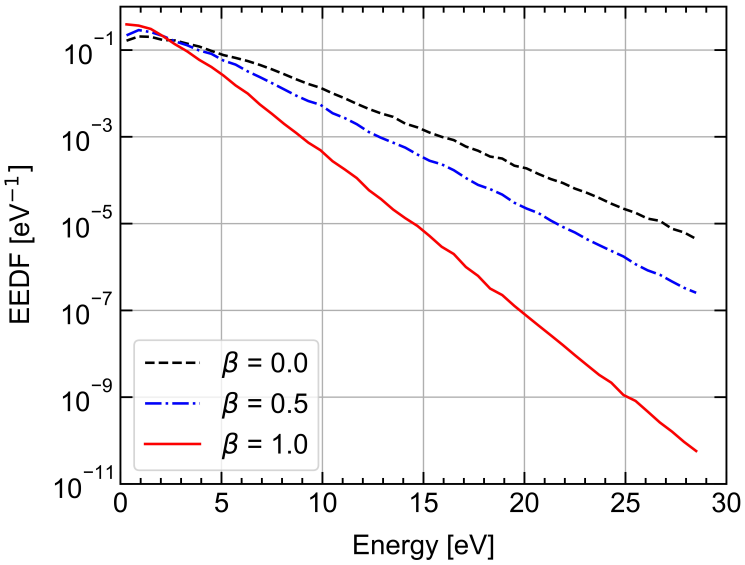

Figure 5.3: Effect of the magnetic field on the EEDF calculated for an orientation of the magnetic field perpendicular to that of the electric field. The same parameters as in Fig. 5.2 and three different values of the Hall parameter $\beta = 0$, 0.5, and 1.0 have been used.

magnetic fields on the EEDF, further showcases the robustness and versatility of this approach. The next sections will show an application of MCF to electrons in D_2 using state-of-the-art cross sections and an extension of the model for simulations of ions in electric and magnetic fields.

5.5.2 Application of MCF to Magnetized Electron Transport

The aim of this section is to show the applicability of MCF for electrons in real gas. In particular, electrons in D_2 gas are considered under the effect of external electric and magnetic fields. Electron impact cross sections with D_2 molecules are taken from the Biagi database of LXCat [192], which includes 15 collisional processes. Furthermore, in this section, the transport matrix of Eq. (5.11) is considered for the whole velocity space, not only for the energy space. In this way, the MCF method provides access to the full VDF, and not only to the EEDF. All the MCF simulations reported in the following have been performed with 100 cells in energy space and 10 cells in $\cos\theta$, where θ is the angle between the velocity vector and the direction of the electric field. The number of electrons per cell is set to 100.

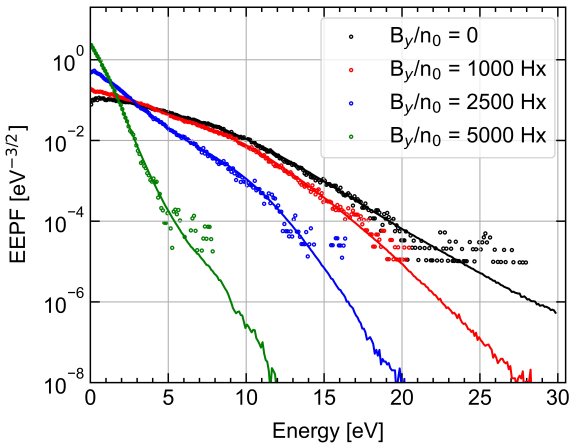

Figure 5.4: EEPFs computed using Monte Carlo (dots) and Monte Carlo Flux (lines) simulations of electrons under constant reduced electric field of 100 Td and variable magnetic field from 0 to 5000 Hx for electrons in D_2 gas.

Figure 5.4 shows the electron energy probability function (EEPF) obtained with conventional MC and MCF for a fixed value of the reduced electric field (E/n_g) of 100 Td (1 Td = 10^{-21} V m^2 and different values of the reduced magnetic field (B/n_g) from 0 to 5000 Hx (1 Hx = 10^{-27} T m^3). The magnetic field is assumed to be perpendicular to the electric field direction. As shown in Fig. 5.3, increasing the magnetic field results in a reduction of the EEPF tail, which becomes closer to

a Maxwellian for $B/n_g = 5000$ Hx. Results showed in Fig. 5.4 also illustrate the increased resolution in the tail of the EEPFs computed using MCF compared to the ones obtained with MC. It is noticed that similar results could also be obtained with conventional MC simulations by increasing the total number of simulated particles by (at least) two orders of magnitude, which would also increase the computational time of the simulations.

The increased information present in this simulation compared to a numerical solution of the two-term Boltzmann equation is clearly shown in Fig. 5.5, where the Legendre polynomial coefficients up to the third term of the spherical harmonic expansion of the electron VFD are reported. It is worth noticing that MCF is not based on a spherical harmonic expansion of the VDF and the l-th order coefficients of the Legendre polynomials are computed as [179]:

$$f_l\left(\epsilon + \frac{\Delta\epsilon}{2}\right) = \frac{2l+1}{2}\frac{1}{N\Delta\epsilon}\int_0^\pi P_l(\cos\theta) f(\epsilon, \cos\theta)\sin\theta d\theta, \tag{5.12}$$

where $\Delta\epsilon$ is the energy bin, and N is the total number of simulated particles. In particular, Figs. 5.5a and 5.5b show the MCF results at $E/n_g = 100$ Td and different values of B/n_g of 0 and 2500 Hx, respectively. Results in the Figures aforementioned clearly show that, as the magnetic field strength increases, the distribution becomes increasingly spherically symmetric, with a significant reduction in the energy gain along the direction of the electric field.

This example with a realistic and large dataset of cross sections for electrons in D_2 demonstrates the applicability of our procedure to magnetized low-temperature deuterium plasmas. Our protocol guarantees a significant reduction in the statistical flutuations of the computed VDFs and solves the problem of characteristic transport times. The author is aware that there are optimization techniques for the Monte Carlo method that allow improving the statistics in regions with fewer events, such as the branching-pruning technique [193, 194]. However, these techniques undoubtedly make the Monte Carlo method more complex and do not solve

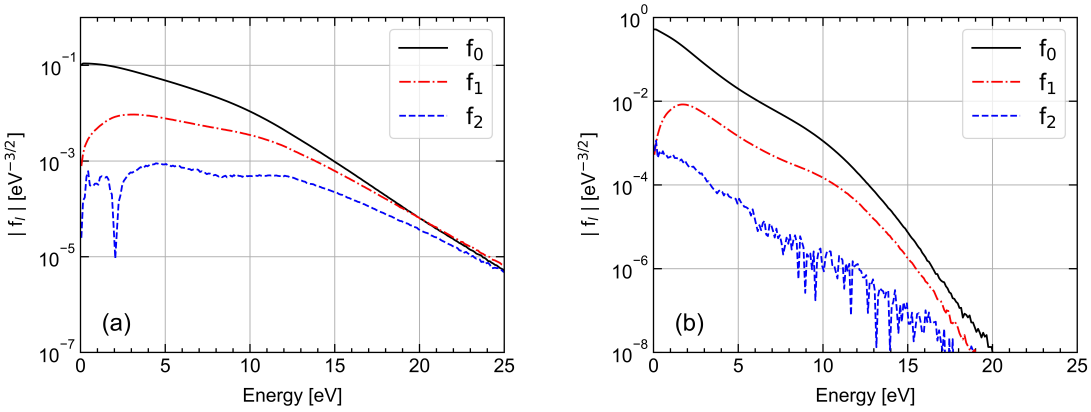

Figure 5.5: Zero*th* (black solid line), first (red dashed-dotted line), and second (blue dashed line) Legendre polynomial coefficients for electrons in D_2 calculated with MCF at a reduced electric field of 100 Td and (a) no magnetic field, (b) reduced magnetic field of 2500 Hx along the y-direction.

the problem of the mismatch of the characteristic times. As is it shown in the next Subsection, the MCF method can be extended to magnetized and non-magnetized ions.

5.5.3 Application of MCF to Magnetized Ion Transport

In many applications, both the ions and the electrons in a discharge are magnetized [195]. This is particularly achievable in hydrogen plasmas, where the ions are relatively lighter compared to other gases. In this subsection, we demonstrate the applicability of MCF for magnetized and non-magnetized ion transport. In particular, the case of atomic ions H^+ in a background gas of H_2 has been considered. The calculation method and numerical parameters are the same procedure as the previous case. Cross sections are derived from the work by Phelps [196] which includes 10 different collisional processes for H^+ ions in H_2. Cross sections reported in the laboratory ion energy frame have been expressed in the centre-of-mass frame for correct computation of the scattering process [197].

Figure 5.6(a) and 5.6(b) show results obtained with conventional MC and MCF

for the first three Legendre polynomial coefficients of the ion VDF expansion. A reduced electric field of 100 Td and a reduced magnetic field $B/n_g = 0$ and 10^4 Hx, respectively, have been used in the simulations. In particular, as a difference with respect to the electron case, the collision between an ion and a molecule results in a significant loss of kinetic energy, as the masses of the colliding particles are comparable. Hence, it is possible to notice that an energy distribution with an extended high-energy tail is produced. Furthermore, unlike the electron case, the ion VDF exhibits considerable anisotropy, where a unidirectional beam of high-energy ions persists after collisions, alongside a more isotropic low-energy bulk.

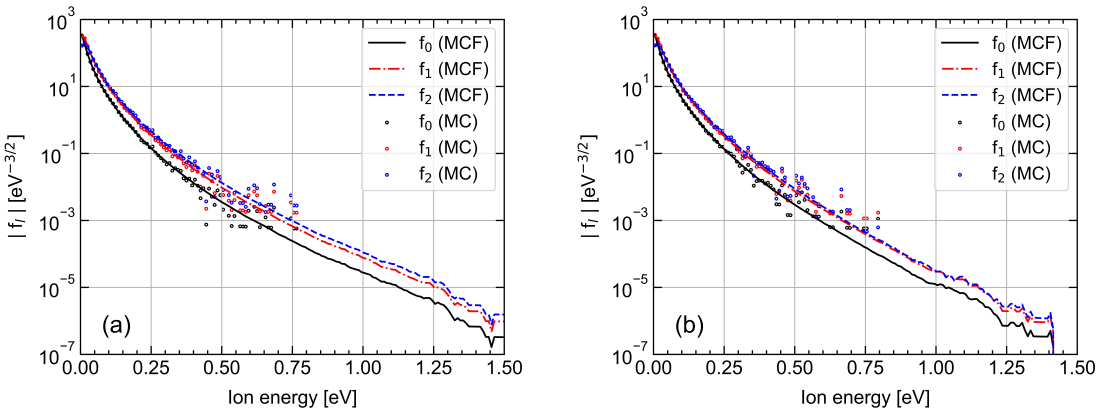

Figure 5.6: Zero*th* (black), first (red), and second (blue) order Legendre polynomial coefficients for H^+ in H_2 calculated with MC (points) and MCF (lines) at a reduced electric field of 100 Td and (a) no magnetic field, and (b) reduced magnetic field of 10^4 Hx. The magnetic field is assumed to be perpendicular to the direction of the applied electric field.

This behavior is confirmed by the different components of the spherical harmonic expansion of the velocity distribution, plotted as a function of ion kinetic energy. The magnetic field modifies the direction of the ion beam, significantly impacting the high-energy tail of the distribution and leading to an overall reduction in the average ion energy.

Larger differences between non-magnetized and magnetized conditions can be seen by comparing Fig. 5.6(a) with Fig. 5.7(a) and Fig. 5.7(b) where a reduced

magnetic field of 5×10^4 Hx and 10^5 Hx has been used. In particular, the magnetic field tends to suppress the formation of high-energy ion beams, which are more prominent in the absence of a strong magnetic field due to the reduced constraint on ion trajectories. The increased isotropization of the ion VDF is clearly observed in the decrease of higher-order Legendre polynomial coefficients with increasing magnetic field strength, as seen in Figures 5.7(a) and 5.7(b). This overall trend reflects the significant role of the magnetic field in reducing the anisotropy of the VDF.

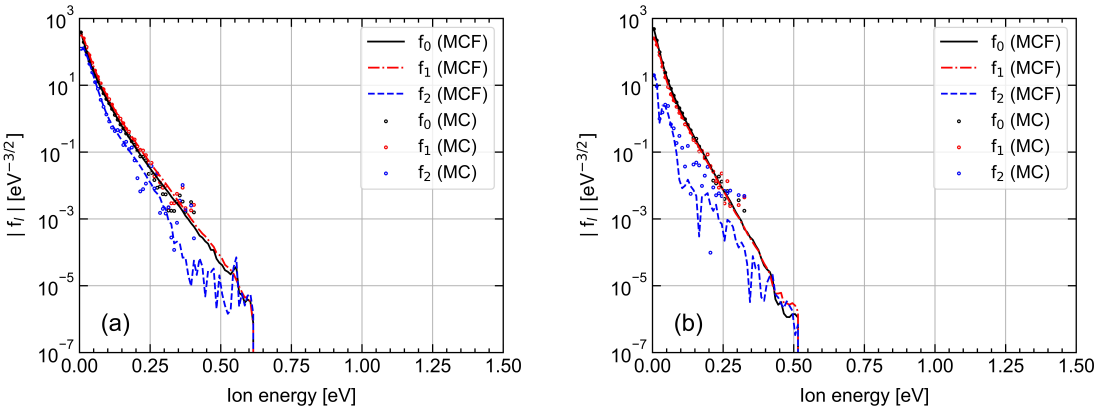

Figure 5.7: Zero*th* (black), first (red), and second (blue) order Legendre polynomial coefficients for H^+ in H_2 calculated with MC (points) and MCF (lines) at a reduced electric field of 100 Td and (a) reduced magnetic field of 5×10^4 Hx, (b) reduced magnetic field of 10^5 Hx. The magnetic field is assumed to be perpendicular to the direction of the applied electric field.

These results also show, for the first time, the effective application of MCF for ion transport in gases. In particular, in Fig. 5.6 and Fig. 5.7, it is shown that MCF can lead to a better resolution of the tail of the distribution, as compared to conventional MC. This is due to the fact that a uniform distribution of charged particles is used at time $t = 0$ for calculation of transition probabilities. This advantage makes the variance reduction technique particularly attractive for multi-scale and multi-physics simulations of fusion devices.

5.6 Remarks on MCF

In this chapter we have demonstrated the effectiveness of the MCF method in quantitatively capturing the kinetic behavior of electrons in a gas under the influence of electric and magnetic fields. For the first time, MCF has been applied to the study of magnetized electron transport. Moreover, this method has been applied for the first time to study both magnetized and non-magnetized ion transport in gases, highlighting its versatility in modeling different charged particle species.

The MCF approach leverages a hybrid method that combines the stochastic treatment of individual Monte Carlo collisions with a Master Equation framework, which accurately extends the kinetics over the relaxation time scales of the system. This allows the method to efficiently simulate systems with widely separated time scales by treating fast, collisional processes stochastically and the slower kinetic energy relaxation deterministically. The result is a uniform reduction of statistical fluctuations in the computed VDF, independent of the value of the sampled distribution, and a computational time gain up to a factor 10, particularly in highly collisional electron systems. The method is thus especially advantageous in scenarios where the collisional timescales are short compared to the relaxation time-scales, as demonstrated in our simulations of electrons in D_2.

In this work, MCF has been verified for electron transport in a model gas, and we have applied it to both electron dynamics in D_2 and ion transport in H_2. In the electron case, we observe a strong anisotropy in the VDF due to the high mobility of electrons in the direction of the electric field, which is gradually suppressed as the magnetic field increases. This behavior is reflected in the decrease of higher-order Legendre polynomial coefficients, indicating that the magnetic field redistributes the electron velocities more uniformly. For ions, we explored H^+ transport in H_2 across various magnetic field strengths. At low magnetic fields, ion VDFs exhibit a pronounced anisotropy, characterized by a high-energy ion beam. However, as the

magnetic field increases, we observe a reduction in this anisotropy, with the ions' motion becoming more isotropic due to enhanced magnetic field. The magnetic field also suppresses the high-energy tails of the ion VDF, reducing the average ion kinetic energy.

The MCF method retains the flexibility of conventional Monte Carlo approaches, allowing it to easily adapt to systems with magnetic fields oriented in any direction while preserving the computational efficiency of lattice-based Boltzmann solvers. Despite its wide-ranging advantages, the implementation of MCF remains straightforward, requiring only minor modifications compared to conventional Monte Carlo simulations. Given these benefits, we anticipate that MCF can become a widely used tool in the study of magnetized and non-magnetized transport in plasmas and gases, and eventually coupled to machine learning approaches for fast matrix solutions [198]. Future work will focus on extending this approach to non-hydrodynamic regimes and incorporating time-dependent electric and magnetic fields, further broadening its applicability to complex plasma systems.

5.6.1 MCF for future DFD design

Beyond its demonstrated accuracy and computational efficiency, the MCF method holds significant potential to inform the design of future DFD systems. While the results in this thesis are obtained under simplified conditions with a uniform plasma, the advantages of MCF become particularly relevant in more complex simulations of direct-drive propulsion. One of the key benefits is the substantial reduction in granular noise, a common limitation of Monte Carlo simulations, particularly in the high-energy regions of the electron and ion velocity distributions. This improvement enables a more precise determination of reaction rates at a much lower computational cost, which is essential for optimizing plasma behavior in DFD concepts. Additionally, the method's ability to accurately resolve electron velocity

distributions, even in multidimensional multi-physical simulations, makes it a valuable tool for integrated propulsion modeling. Furthermore, its potential extends beyond propulsion, as MCF can be applied to the optimization of ion sources, which have been proposed as auxiliary plasma heating systems in fusion reactors. These advantages make MCF a promising component for future simulations of DFD devices, where capturing kinetic effects with high accuracy and efficiency is crucial. Indeed, advancing our understanding of direct fusion propulsion requires simulation techniques that are as general as possible while remaining intuitive enough to integrate into a modular model seamlessly. A significant challenge in this regard stems from the fact that most plasma models applicable to fusion drives are fluid-based, assuming that the plasma can be described macroscopically at least on a local scale. However, in fusion propulsion, the mean free path of the particles is not necessarily small compared to the dimensions of the reactor—this is even more pronounced for the energy relaxation length of electrons. In other words, achieving a reliable model of the complete system requires describing electron dynamics from first principles, a conceptual and computational challenge that may take years to fully develop.

This thesis presents a solution to what is arguably the most critical aspect of system modeling after the kinetics of the fusion reactions themselves: the transport of charged particles. By applying an optimized Monte Carlo simulation technique that has only recently gained significant attention in the plasma community, it becomes possible to account simultaneously for collisional processes and the influence of electric and magnetic fields. Moreover, this approach effectively mitigates the primary limitations of traditional Monte Carlo methods precisely where improvements are most needed, such as in the high-energy tail of the electron velocity distribution. This makes it ideally suited for integration into a future multi-physics simulation of the entire propulsion system. Additionally, the same methodology can be applied to auxiliary systems based on "cold" electrical discharges, including

those used for generating neutral hydrogen beams and plasma diagnostics.

In conclusion of this chapter we can state that the methodology developed in this thesis, due to its calculation speed and accuracy, has the potential to become in future studies an essential part of modular simulation programs for DFD devices.

Chapter 6

Mission Analysis and Applications

This chapter presents a comprehensive mission analysis for scenarios employing advanced propulsion technologies, specifically the solar sail and the DFD. It begins with an overview of proposed mission concepts in the literature, examining the feasibility of low-thrust missions to the outer solar system and beyond. Separate sections detail simulation results for both the solar sail and DFD propulsion scenarios, evaluating parameters such as acceleration, payload capability, and mission duration. The chapter concludes with a comparative analysis, synthesizing findings from the simulations and identifying the relative advantages and limitations of each system. This comparison provides valuable context for selecting propulsion methods based on mission requirements and technological capabilities.

6.1 Deep Space Mission Requirements

The Δv requirements for deep space missions vary significantly depending on the target destination and mission's objectives. For missions aimed at exploring celestial bodies such as Enceladus, Europa, asteroids, and even distant targets like Sedna and the Kuiper Belt, understanding the Δv requirements is crucial for mission planning, spacecraft design and trajectory optimization [199].

For near-Earth asteroids (NEAs), the Δv required for rendezvous can be lower

than that needed for lunar missions, with many NEAs offering advantageous trajectories due to their positions and orbits' shape. This makes them attractive targets, as they provide opportunities to study the early solar system with relatively lower propulsion costs. In Ref. [200] a survey of suitable targets is presented, with rendezvous Δv lower than 10.5 km/s, well below the solar system escape velocity (12.3 km/s). Recent studies also suggest using AI and neural networks for multiple NEAs rendezvous missions with continuous thrust [32, 201].

In the context of missions to the outer solar system, such as those targeting Enceladus or Europa, the Δv requirements increase substantially due to the greater distances involved and the need for more complex trajectory maneuvers. For instance, missions to these icy moons often require multiple gravity assists and precise orbital insertions, which can escalate the Δv demands.

For missions venturing into the Kuiper Belt or even to the Oort Cloud, the Δv requirements become even more pronounced; finally, when considering interstellar missions, such as those targeting Alpha Centauri, the Δv requirements become remarkably high, necessitating innovative propulsion technologies and mission architectures.

Table 6.1 presents the destinations proposed in Chapter 1, their distances (in AU) and their orbits' semi-major axis, eccentricity and inclination. For generic regions (e.g. Kuiper Belt, Oort Cloud), we indicate approximate orbital parameter values corresponding to typical orbits of bodies within those areas.

Destination	r [AU]	SMA [km]	ECC	INC [deg]
Europa (Jup)	5.2	6.71×10^8	0.009	0.466
Enceladus (Sat)	9.5	1.43×10^9	0.056	2.489
Kuiper Belt*	30-50	$\sim 5 \times 10^9$	0.25-0.75	0-30
TNO Sedna	70-1,000	1.41×10^{10}	0.846	11.93
Oort Cloud*	2,000-100,000	7.5×10^{12}	0.9	0-180
Alpha Centauri*	272,000	4.07×10^{13}	0.52	79.19

Table 6.1: Deep space mission destinations' reference heliocentric distances (AU) and main orbital parameters, describing orbit size (SMA) shape (ECC) and inclination (INC). For targets identifying a region, values are given for typical bodies within those areas.

Given the immense distances involved, it is clear that traditional propulsion systems could never reach most deep-space targets within a reasonable time frame. For example, at a cruise velocity of 10 km/s, it would take approximately 130,000 years to reach Alpha Centauri, which is 4.34 light-years away. This speed is just slightly slower than that of *Voyager 1*, launched in 1977, which by 2024 had traveled 164 AU (around 3 AU per year). Even at a velocity of 100 km/s, the journey would still take 13,000 years. To make the timing reasonable, a speed of about 25,000 km/s would be required, reducing travel time to roughly 50 years. Long explores plausible concepts for achieving this velocity in the future in Ref. [44]. The *Breakthrough Starshot* project proposes ultra-light *StarChip* robotic nanocrafts equipped with light sails, which are designed to travel at 20% of the speed of light. These would reach Alpha Centauri within 20 to 30 years and take around 4 years to notify Earth of a successful arrival [29].

6.2 Proposed Scenarios and Tools

Following the description of the propulsion mechanisms presented in previous Chapters, this section provides details on the suggested mission profiles for both the DFD and the solar sail enhancing thermal desorption. In Ref. [202] results for a mission to Sedna were discussed. The results presented below have been obtained in the course of several years, and within different applications. Besides from classic Mission Analysis tools, such as Ansys STK and NASA GMAT, ad-hoc scripts were realized for specific purposes (Matlab, python, etc.). The opportunity to use the IRMA (InteRplanetary Mission Analysis) code [203] was also explored for some initial estimates on optimal departure dates.

6.2.1 Current, Legacy, and Future Mission Concepts

Missions to the icy moons and the Kuiper Belt hold a significant place in the history of space exploration, with numerous suggestions in the literature for future exploration. For missions targeting Enceladus, Saturn's moon, the Cassini mission provides valuable insights [11, 12, 57], having conducted extensive studies of Enceladus. The Δv for a mission to Enceladus can be estimated at around 6.5 km/s, accounting for necessary trajectory adjustments and possible gravity assists. Due to Enceladus's low mass and close orbit around Saturn, maintaining stable, near-polar science orbits poses challenges [204]. One approach involves orbits around Enceladus's equilibrium points within the circular restricted three-body problem, with Saturn and Enceladus as primary bodies. The geometric and kinematic properties of these trajectories make them promising for extended observations of Enceladus's surface: they are highly inclined, bring the spacecraft close to the moon, and are largely maneuver-free. However, the low altitudes and Saturn's strong perturbing forces require careful analysis of these orbits [205]. Such solutions provide long, uninterrupted views of the lunar surface at low speeds, enhancing scientific returns.

Similar considerations apply to missions targeting Jupiter's moon Europa. The recently launched Europa Clipper mission [16], designed to investigate Europa's potential for habitability, requires a projected Δv of about 7.5 km/s for its entire mission profile, including launch, trajectory corrections, and planned orbital insertion in 2030.

For exploring the Kuiper Belt and the Oort Cloud, NASA's New Horizons mission to Pluto serves as a valuable precedent [9, 10]. The mission required an initial Δv of approximately 14 km/s to escape Earth's gravity and set the spacecraft on its trajectory to the distant target.

Regarding the TNO Sedna, given its orbital period of about 11 thousand years and considering its perihelion passage (at a distance of around 74 au from the Sun) estimated to be in 2073–74, scientists have been proposing missions for launch in

the next few years (around 2030), including gravity assist that would allow reaching Sedna in time for its closest approach [206]. In Ref. [206] Zubko et al. presented a possible concept including gravity assist maneuvers near Venus, Earth, Jupiter, Saturn and Neptune, with a departure date between 2029-2034. Further details on the optimal trajectory proposed are given in Ref. [207], where Venus, Earth and Jupiter flybys allow to reach the target in less than 30 years for a Δv of less than 5 km/s. The same author investigated the possibility of meeting even more demanding time constraints and limiting the mission to 20 years with a departure in 2041 [208]. These studies considered impulsive maneuvers with conventional engines.

6.2.2 Solar Sail Scenario

In this section we present applications and performances for the solar sail. The sail proposed consists of a reflective membrane coated by materials that undergo thermal desorption. In the case of selecting a structural design with an inflatable torus-shaped rim, the sail's deployment from its stowed configuration is initiated by introducing inflation pressure into the toroidal rim [209, 210]. For a conventional square sail, instead, the sail deployment would happen with traditional booms [91]. The heat-sensitive materials' coating undergoes thermal desorption at the perihelion of the heliocentric escape orbit and provides an acceleration - in addition to the conventional one due to solar electromagnetic radiation. As a first step, a scenario with a traditional solar sail is presented, to better highlight the contribution of thermal desorption when it is introduced.

Solar sail spiral trajectory without desorption

In this paragraph the trajectory of the sail without any kind of additional aid is introduced. Logarithmic spiral trajectories can be obtained with low-thrust propulsion and require the sail attitude to be fixed relative to the Sun-line, so a constant

ϑ with respect to the instantaneous radius vector. A simple steering law is required to control the sail attitude. This type of trajectory requires the spacecraft acceleration to have an inverse square variation with orbit radius, as in the case of solar sails. The more β increases, the less time is required: a solar sail with $\beta = 0.1$ requires between 400 and 500 days to reach 0.1 AU; considering $\beta = 0.4$ instead, only about 100 days are needed to reach the same distance. Results of calculations are presented in Fig. 6.1 and Table 6.2 for the lightness number $\beta = 0.1$.

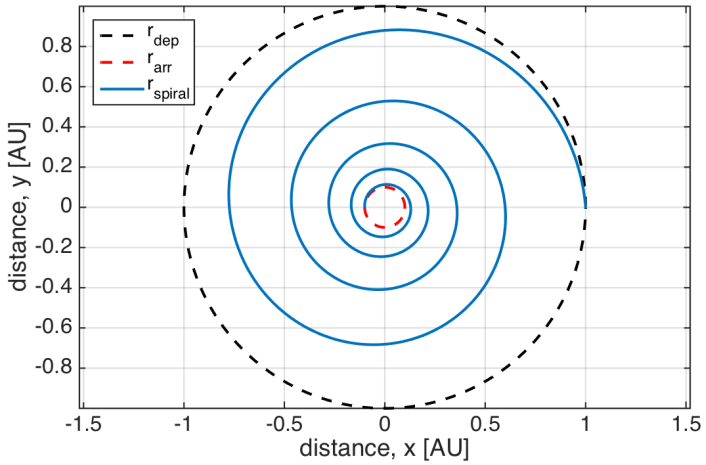

Figure 6.1: Solar sail trajectory from 1 AU to 0.1 AU with optimum pitch angle $\vartheta = 35°$ and low lightness number $\beta = 0.1$.

Table 6.2: Spiral logarithmic trajectories from Earth to different perihelion radii, for $\beta = 0.1$, $\vartheta = 35°$.

radius of perihelion	r_P	$[AU]$	0.3	0.2	0.1
speed at r_P	v_P	$[km/s]$	54.33	64.77	91.60
transfer time	t_f	$[days]$	409	445	474
required ΔV at departure	ΔV_{dep}	$[km/s]$	2.5	2.5	2.5

Alternative trajectory to reach the desired heliocentric distance

As an alternative to reach the same heliocentric distance, one could also evaluate the use of traditional chemical propulsion, having the sail stowed and then only deployed at perihelion. For this scenario, we assume a Hohmann transfer that would bring the sail to the required heliocentric distance, where the sail is then released. In the following section, we compare the results of a traditional solar sail from the moment it is deployed, against those obtained with the additional contribute of thermal desorption acceleration.

Earth orbit is considered to be circular. Take into account a transfer from the Earth orbit of radius $r_2 = 1\,AU$ to an inner orbit of radius $r_1 < r_2$.

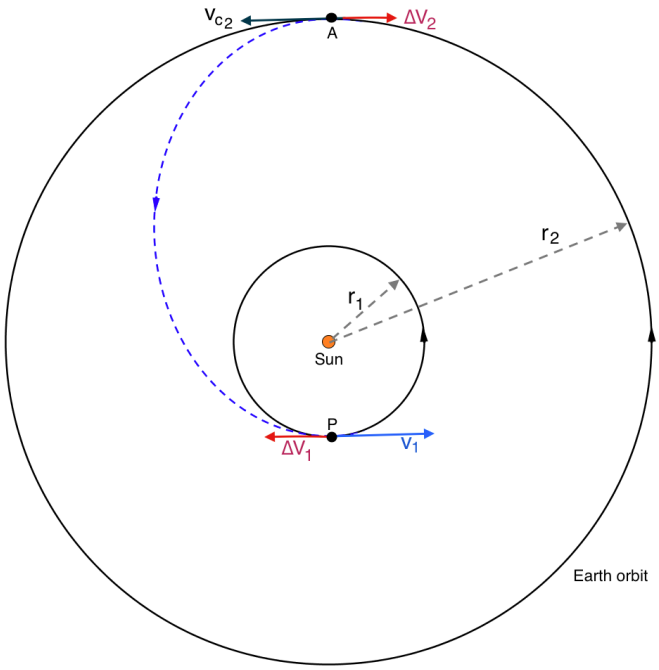

Figure 6.2: Hohmann transfer from Earth orbit to an inner orbit. The considered scenario doesn't require any change in velocity when the inner orbit is reached.

Fig. 6.2 shows the schematic diagram for the Hohmann transfer from Earth orbit to an inner orbit. When leaving Earth, the sail (still not deployed) is at a distance $r_2 = 1\,AU$ and has a circular velocity $v_{c_2} = \sqrt{\mu/r_2} = 29.76\,km/s$; note that as an heliocentric frame is considered, μ is the Sun gravitational parameter

$\mu_\odot = GM_s = 132500 \cdot 10^6\, km^3/s^2$. In order to reach the orbit of radius r_1, a change in velocity ΔV_2 is required, parallel to v_{c_2} but in the opposite direction. In fact, to diminish the perihelion - point P in Fig. 6.2 - it in necessary to reduce the velocity at the aphelion (point A in the same Figure). For example, if $r_1 = 0.1\, AU$, the ΔV_2 that allows to get onto the semi-elliptical transfer orbit, by obtaining a velocity $v_2 = 12.69\, km/s$, starting from v_{c_2}:

$$\Delta V_2 = |v_2 - v_{c_2}| = \left| v_{c_2} \left(\sqrt{\frac{2r_1}{r_1 + r_2}} - 1 \right) \right| = 17.07\, \frac{km}{s}. \tag{6.1}$$

Once in point P, a second change in velocity would be required, ΔV_1, for a standard Hohmann transfer, in order to circularize the orbit. However, the scenario described doesn't deserve the second ΔV to be performed: in fact, the aim is to escape the Solar System, and not to start orbiting around the Sun.

Considering the Earth's sphere of influence, ΔV_2 corresponds to the hyperbolic excess of velocity v_{∞_e}. The required ΔV_0 is given by Eq. (6.2):

$$\Delta V_0 = v_0 - v_{c_0} = \sqrt{v_{esc_0}^2 + v_{\infty_e}^2} - v_{c_0} = \sqrt{\frac{2\mu}{r_0} + v_{\infty_e}^2} - \sqrt{\frac{\mu}{r_0}}. \tag{6.2}$$

In Table 6.3 the Hohmann transfer has been evaluated for three different desorption radius, $r_1 = 0.3,\ 0.2,\ 0.1\, AU$ respectively. For every heliocentric distance, the corresponding temperature is given. The velocities v_2 and v_1 come from the conservation of energy. For the Hohmann transfer the ellipse is tangent to both orbits, so the flight path angles are $\gamma_1 = \gamma_2 = 0°$. Once the point P has been reached, the sail can finally be deployed. If the sail is coated with a material that undergo thermal desorption, for example, at the temperature $T_1 = 1140.6\, K$ at the distance 0.1 AU, this will start to evaporate and generate additional thrust. But before considering it, it should be interesting to evaluate the sail behavior if only photon thrust is present, as a traditional solar sail without coating.

Table 6.3: Heliocentric Hohmann transfer from Earth orbit to the heliocentric distance that corresponds to the required temperature of desorption.

radius of perihelion	r_P	$[AU]$	0.3	0.2	0.1
temperature	$\mathcal{T}$	$[K]$	737	865	1140
eccentricity	e_H	-	0.54	0.67	0.81
semi-major axis	$\mathfrak{a}_H$	$[km]$	$9.72 \cdot 10^7$	$8.98 \cdot 10^7$	$8.23 \cdot 10^7$
time of flight	t_f	$[years]$	0.26	0.23	0.20
speed at r_2	v_2	$[km/s]$	20.22	17.18	12.69
speed at r_P	v_1	$[km/s]$	67.39	85.91	126.89
hyp. ex. vel. at Earth	v_{∞_e}	$[km/s]$	9.54	12.58	17.07
ΔV required	ΔV_0	$[km/s]$	6.79	8.93	12.53

Traditional solar sail performance

In this paragraph no desorption is considered, only photon thrust. During the Hohmann transfer the sail was not deployed, so the velocity at the perihelion, when $r_1 = 0.1\ AU$, is

$$v_P \equiv v_1 = \sqrt{\frac{\mu}{r_1} \frac{2r_2}{(r_1 + r_2)}} = 126.89\ \frac{km}{s}. \tag{6.3}$$

At the perihelion the sail is deployed and approaches its asymptotic speed on the hyperbolic orbit, which can be considered its cruise speed. For the conservation of energy, it yields:

$$E_g = \frac{v^2}{2} - \frac{\mu\,(1-\beta)}{r} = \frac{v_P^2}{2} - \frac{\mu\,(1-\beta)}{r_P}, \tag{6.4}$$

where β is the lightness number of the solar sail as defined in Eq. (3.14). However E_g is also known from the Hohmann transfer orbit. Therefore, the asymptotic speed can be obtained by setting $r \longrightarrow \infty$ in the Eq. (6.4):

$$v_{cruise} = v_\infty \equiv \sqrt{v_P^2 - \frac{2\mu\,(1-\beta)}{r_P}} \tag{6.5}$$

With the cruise speed one can find the distance covered per year.

Both Eqs. (6.4) and (6.5) depend on the lightness number. As shown in Fig. 3.7, β influences the sail trajectory: in order to escape $\beta \geq 1/2$ is required. Also, it depends on the sail loading factor σ and its acceptable value are $\sigma \leq 2.5\, g/m^2$.

Table 6.4: Traditional sail cruise speed and distance covered.

σ $[g/m^2]$	β	v_{cruise} [km/s]	distance/year [AU/year]
2.5	0.5	86.7	18.3
2.1	0.6	95.6	20.2
1.7	0.7	106.9	22.6
1.4	0.9	122.5	25.8
1	1.2	145.7	30.7

Acceleration due to thermal desorption

Now consider that, once the perihelion is reached, the sail is deployed and its coating undergoes thermal desorption. Solving Eq. (3.33) the final velocity of the sail after the desorption time can be determined. The considered sail area, coating mass and thickness are the ones indicated in Section 3.5.3. The acceleration due to desorption is of the order of m/s^2, whereas that of photon pressure is a few mm/s^2, for this reason the photon pressure acceleration is neglected during the desorption time.

The final velocity obtained after 34000 s of thermal desorption is $v = 167.16 km/s$, $v = 213.43\ km/s$ and $v = 315.81\ km/s$ for $r_P = 0.3\ AU$, $r_P = 0.2\ AU$ and $r_P = 0.1\ AU$ respectively.

Considering $\sigma = 1 g/m^2$, so that $\beta = 1.2$, the cruise speed obtained thanks to the photon pressure from Eq. (6.5) is then $v_{cruise} = 170.65\, km/s$, $v_{cruise} = 217.54\, km/s$ and $v_{cruise} = 321.43\, km/s$ respectively.

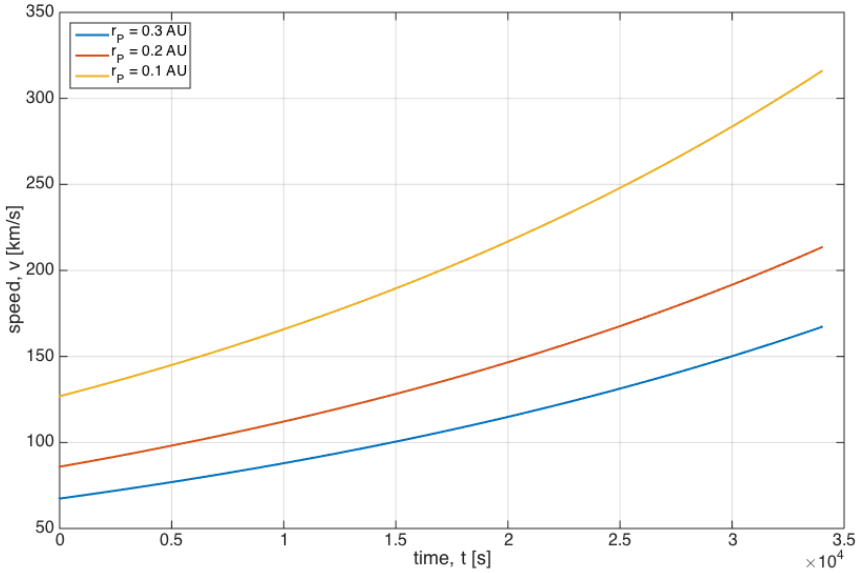

Figure 6.3: Gain in velocity due to thermal desorption acceleration for the three different perihelion radii.

Table 6.5: Sail cruise speed and distance covered considering thermal desorption.

radius of perihelion	r_P	$[AU]$	0.3	0.2	0.1
speed at r_P before desorption	v_1	$[km/s]$	67.39	85.91	126.89
speed at r_P after desorption	v_P	$[km/s]$	167.16	213.43	315.81
cruise speed	v_{cruise}	$[km/s]$	170.65	217.54	321.43
distance/year	AU_y	$[AU/year]$	35.9	45.8	67.7

Sail scenario proposed

We suggest the following sequence for the mission: elliptical transfer to Jupiter, gravitational slingshot, followed by thermal desorption. Initially, the spacecraft performs a transfer from Earth's orbit to Jupiter's orbit using conventional propulsion. A gravitational assist from Jupiter then redirects the trajectory towards a close approach to the Sun, as shown in the red orbit in Fig. 6.4.

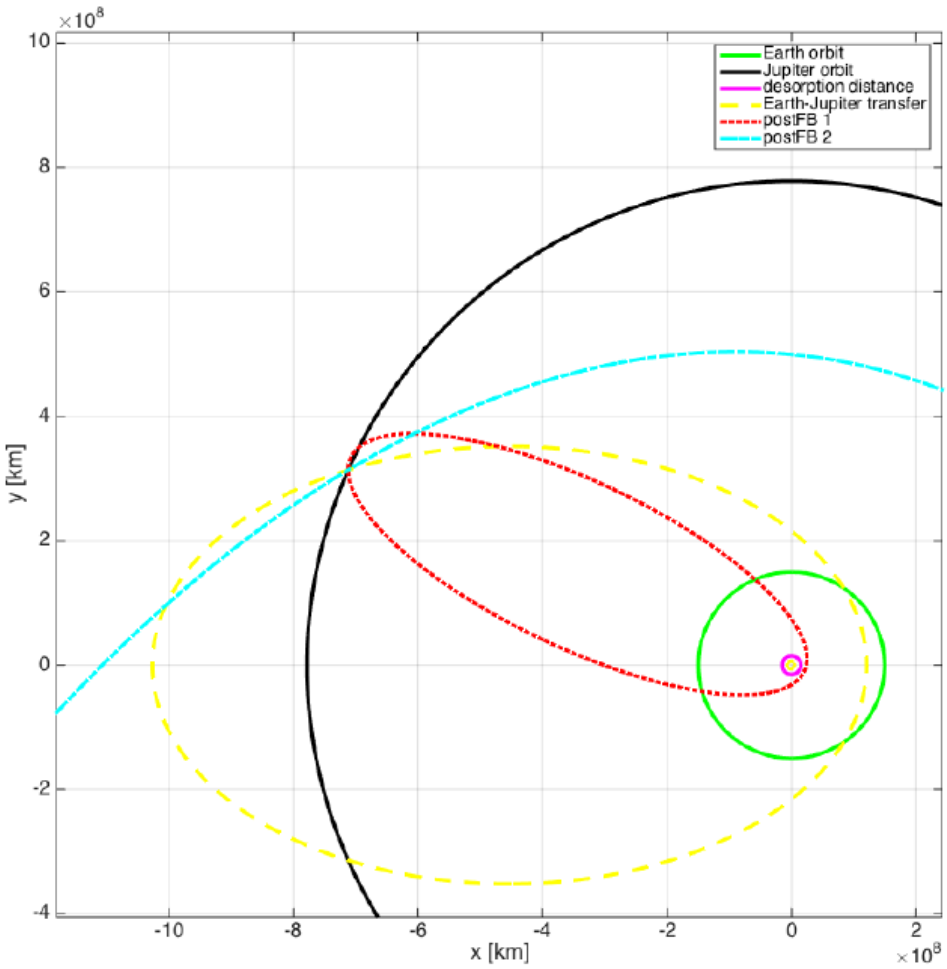

Figure 6.4: Jupiter Flyby: increase and decrease in orbital energy when passing behind (cyan orbit, dash-dot line) or in front (red orbit, dotted line) of the planet, respectively.

At the perihelion, the solar sail is deployed, and its coating undergoes desorption. This results in two sources of acceleration: one from the material desorption of the coating and the other from the solar radiation pressure, propelling the spacecraft toward deep space. The perihelion distance to aim for depends on the coating material [125]. We assume the following parameters for the sail: lightness number β = 0.75, areal mass σ = 5 g/m^2, coating mass M_c = 1 kg, mass of payload m_{pl} = 1.5 kg, desorption rate of 1 g/s. For a perihelion of 0.3 AU, the resulting cruise speed would reach about 100 km/s. Traveling at about 20 AU/year, from the moment of

deployment at perihelion it would take approximately 4 years to arrive at Sedna; however, the time for the transfer to Jupiter first and then the desorption target distance has to be added, giving a total mission time of about 7 years. This would still be less than a half of the results obtained for with a traditional propulsion system [208]. For the same sail, it would take 100 years to reach the inner edge of the Oort cloud (about 2000 AU). In order to reduce the time required even further, a closer approach to the Sun would be effective, however limitations on the materials have to be taken into account. Results for a parametrical analysis and the influence of other factors that could allow achieving higher cruise speed are given in [4].

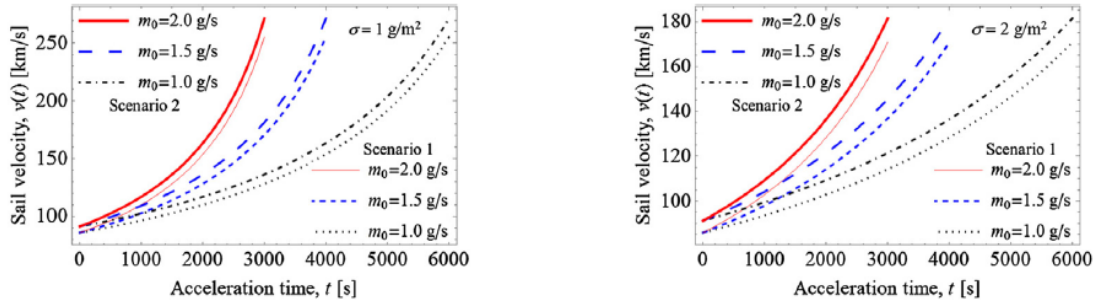

Figure 6.5: Dependence of the sail velocity on the acceleration time for the different rate of desorption. Calculations are performed for a coating mass of 6 kg and perihelion 0.2 AU, with the areal mass 1 g/m^2 (left panel) and 2 g/m^2 (right panel) respectively [4].

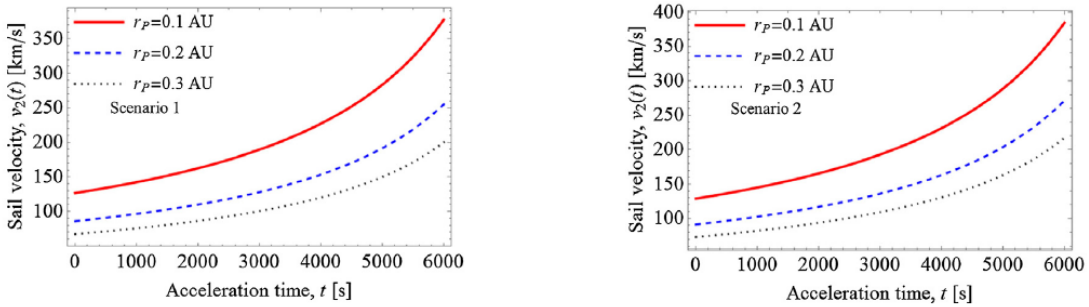

Figure 6.6: Gain in velocity due to thermal desorption for the different heliocentric distances of perihelion. Calculations are performed for the coating mass 6 kg and the desorption rate 1 g/s.

Fig. 6.5 and 6.6 show the dependence of the sail velocity on the acceleration time for the different rates of desorption for two different scenarios: the first consisting of

a direct transfer from Earth orbit to the perihelion of the heliocentric orbit required for desorption; the second corresponding to the one analyzed in this study, thus a transfer to Jupiter allowing to reach the perihelion at a higher speed.

6.2.3 DFD Scenario

The exploration of the solar system requires advanced propulsion techniques capable of specific impulse above 10^4 s and specific power in the range 1–10 kW/kg. Using the Direct Fusion Drive, one way trips to Mars become possible in slightly more than 100 days [2], and the total mission duration for exploration of trans-Neptunian objects would take slightly more than eight years [139]. In Chapter 1, we discussed Enceladus (Saturn's moon) and Europa (Jupiter's moon) as promising exploration targets within distances already reached by past missions, as noted in the previous section. However, employing the Direct Fusion Drive would considerably shorten the journey time: as demonstrated in Ref. [138], a mission to Titan could be completed in under two years using a continuous thrust profile. An optimized Thrust-Coast-Thrust (TCT) profile would extend the travel time slightly to 2.6 years, while reducing the propellant required.

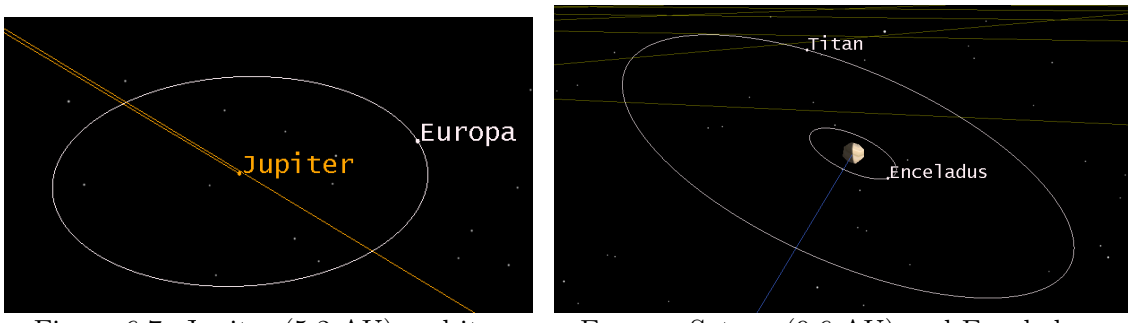

Figure 6.7: Jupiter (5.2 AU) and its moon Europa; Saturn (9.6 AU) and Enceladus.

The performance capabilities of the DFD offer significant flexibility for mission planning. By carefully choosing the departure date, it may be possible to design a multi-target mission that includes a close approach to Europa and either an orbit

insertion or flyby of Titan. These encounters could also be integrated into a longer mission to reach more distant targets, such as Sedna.

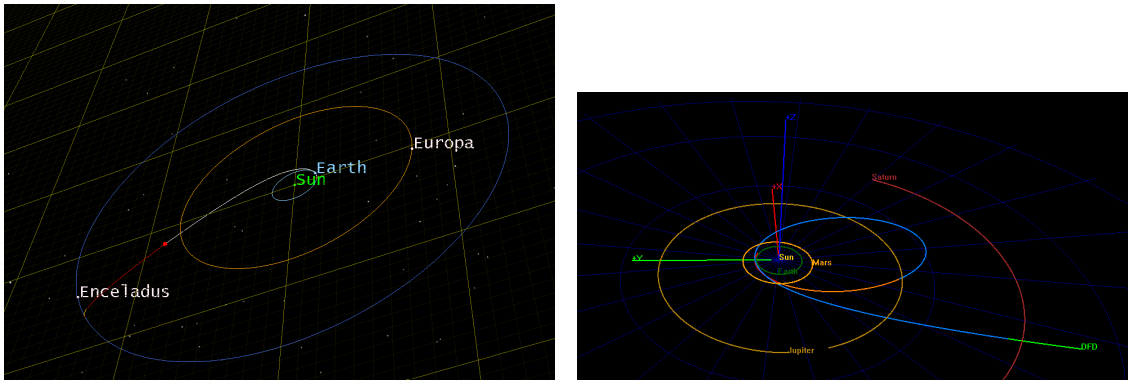

Figure 6.8: Mission scenario for DFD targeting icy moons; DFD on an escape trajectory.

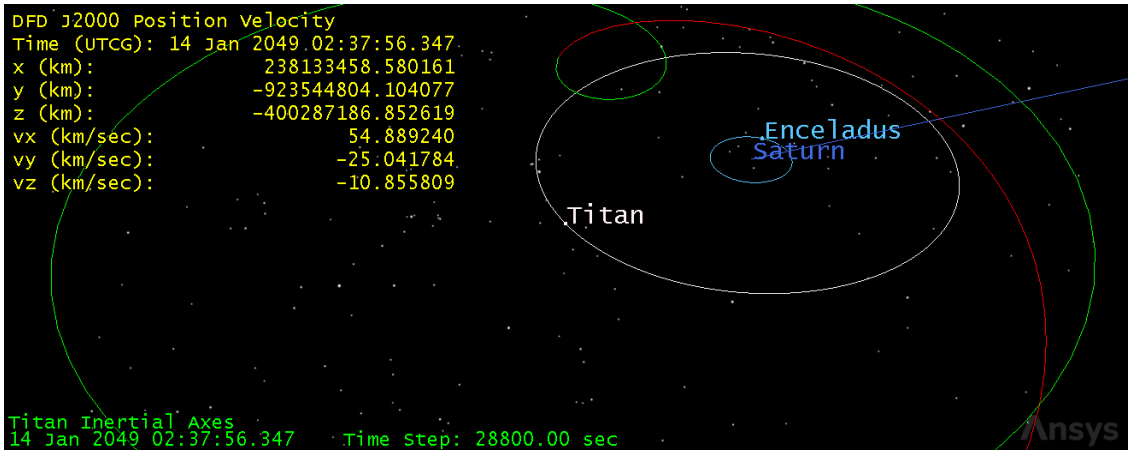

Figure 6.9: Titan orbit insertion with DFD.

For a trajectory design to trans-Neptunian object Sedna, we considered a 2 MW DFD, assuming constant thrust (8 N) and specific impulse (9600 s). Within a TCT profile 3 phases are identified: the Earth escape spiral trajectory; the interplanetary travel coasting phase; and final maneuvers to rendezvous with the target.

As an initial step, we used an Earth Point Mass model propagator, which does not account for Earth orbital perturbations, to simulate the spiral trajectory. This simulation aimed to assess propellant mass consumption and maneuver time required to escape Earth's gravitational sphere of influence. The Earth escape maneuver was obtained using the engine model implemented in STK software, based on

the characteristics outlined earlier. Subsequently, we considered the more accurate Earth HPOP Default v10 finite propagator, which includes Earth perturbations. The results showed that accounting for these perturbations resulted in only a negligible increase in propellant mass and maneuver time. Therefore, it was decided to disregard these perturbations for this relatively short maneuver. The analysis was performed using the sparse non-linear optimizer (SNOPT) on STK software. The thrust components have been calculated using the VNC reference system relative to the Sun.

Sedna ephemeris, like those of any other body, can be downloaded online through the Horizon System as shown in Fig. 6.10 [211]. As demonstrated in [140] a spacecraft with DFD would reach the TNO Eris (at a distance of 78 AU at rendezvous) in around 10 years. Considering this matches with Sedna's perihelion, DFD would decrease the time required by 50% (compared to the 20 years of the traditional propulsion systems in Ref. [208]). A valid solution to reduce the time even more would be to evaluate a constant thrust (CT) profile; thus the disadvantage is that this would require additional propellant, and result in a 1/3 reduction of payload mass. The goal is to deliver at least 1500 kg of payload to the destination in under 10 years. With a specific power of 1 kW/kg, the DFD engine weighs around 2000 kg, resulting in a total dry mass of 3500 kg. Based on an initial estimate, approximately 4000 kg of propellant would be required, bringing the total launch mass to around 7500 kg. The total Δv for the mission is approximately 80 km/s, with half of that needed to slow down during the rendezvous phase, where the coasting velocity is around 38 km/s. Each maneuver would take between 250 and 300 days, requiring about 1.5 years of thrust over the 10-year journey. However, the engine would remain active to supply power to the system. The estimated amount of ^{3}He required for this mission is approximately 0.300 kg. With only about 30 kg of ^{3}He currently available on Earth, sustaining this propulsion system for multiple missions would necessitate obtaining ^{3}He from additional sources, such as mining terrestrial

or off-world deposits, or through synthesis. Note that in this study, no flyby opportunity was considered; including one or more gravity assists could significantly decrease the necessary Δv, as thoroughly analyzed in Ref. [207].

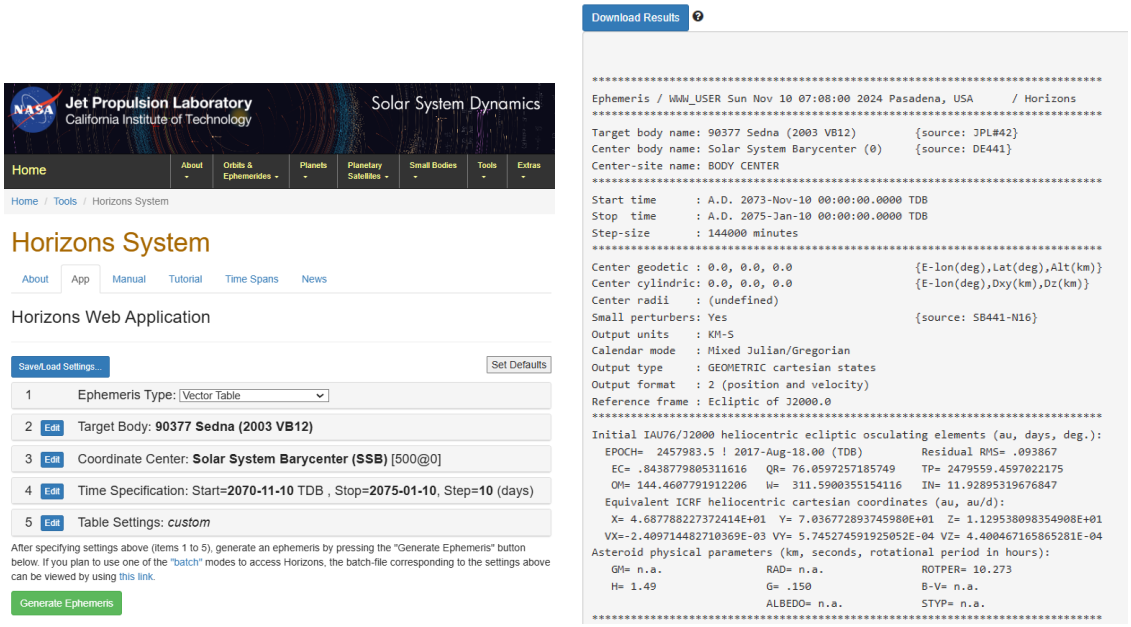

Figure 6.10: NASA Horizons System for Ephemeris download [211].

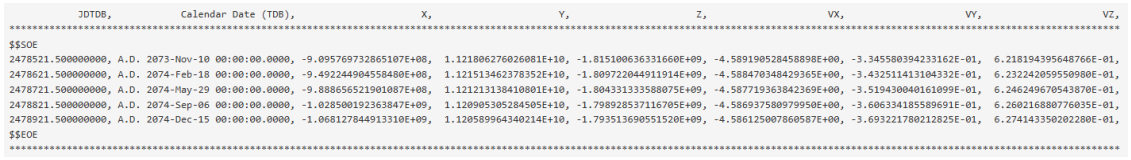

Figure 6.11: Example of Ephemeris for Sedna downloaded from NASA Horizon [211].

A final consideration regarding the proposed strategy is that the TCT profile mission assumes the DFD can be switched on and off for thrust generation. This is a crucial assumption, as it requires the engine to remain inactive for approximately a year during the coasting phase. While theoretically feasible, this capability has not yet been confirmed.

6.3 Comparison and Remarks

This chapter explored the mission potential and performance characteristics of two advanced propulsion systems: the Direct Fusion Drive and a solar sail enhanced by thermal desorption. While each system offers unique advantages, their suitability varies significantly based on mission objectives and payload requirements.

The thermal-desorption-enhanced solar sail demonstrates remarkable speed capabilities, allowing it to reach extremely distant targets at impressive cruise velocities. This approach, where heat-sensitive coating materials desorb at perihelion, provides an additional thrust that supplements solar radiation pressure, pushing the spacecraft to high speeds. For example, the proposed mission profile reaches Sedna in approximately 7 years, and the solar sail could potentially reach the inner Oort Cloud (2000 AU) within a century. However, this technology is limited in payload capacity—typically, only a few kilograms—which restricts it to small-scale missions, such as lightweight probes for initial assessments or exploratory flybys of deep-space objects. Although solar sails can achieve very high speeds, they lack the flexibility to carry heavier or more complex payloads, which constrains their broader application.

In contrast, the DFD system offers substantial flexibility and scalability for both robotic and potential manned missions, enabling it to accommodate much larger payloads. With specific impulse values above 10,000 s and the ability to sustain long-duration missions, DFD could reduce mission times to the outer solar system and beyond while supporting payloads of up to 1500 kg. This system is well-suited for multi-target missions and detailed exploration, as it allows for close approaches and orbit insertions, such as a flyby of Europa, orbit insertion around Titan, or even extended missions to trans-Neptunian objects like Sedna. The DFD is capable of delivering high payload capacities over extended durations. These characteristics

make DFD an appealing option for more ambitious missions requiring comprehensive scientific equipment or life-support systems for future manned exploration.

In conclusion, the choice between these two propulsion methods ultimately depends on the mission's primary goals. For high-speed, lightweight exploration of distant targets, the solar sail with thermal desorption is an effective solution. For versatile, high-payload missions that require intricate operations, such as close planetary flybys or detailed studies of multiple targets, the DFD provides a more adaptable and robust option. Each technology holds distinct potential to expand our reach within the solar system and beyond, depending on mission priorities and constraints.

Conclusions

This study explores two promising propulsion technologies, the Direct Fusion Drive and solar sails enhanced by thermal desorption, for deep space missions. Both methods aim to overcome the significant challenges posed by the vast distance and the long duration of such missions. The DFD, with its high efficiency and power, is ideally suited for robotic exploration missions, enabling substantial payloads and comprehensive scientific analysis. Among the most cutting-edge propulsion technologies, the DFD would be a true game-changer for any robotic missions to distant targets, offering a payload capacity of up to 1500 kg. On the other hand, the solar sail, due to its light payload capacity (approximately 1.5 kg), could be an excellent choice for a preliminary mission carrying minimal equipment to conduct initial assessments and evaluations.

In this thesis, various aspects of physical modeling were developed to suggest that alternative low-thrust propulsion systems could be concretely employed in mission scenarios made attractive by recent developments in astrobiology.

For what concerns the solar sail, our work presented an innovative solution enhancing thermal desorption. The sail's deployment from its stowed configuration allows the heat-sensitive materials to undergo desorption at the perihelion of the heliocentric escape orbit. This provides an additional acceleration on top of the conventional one due to solar electromagnetic radiation. The details of the propulsion mechanism are given in Chapter 3, and results for mission scenarios are presented in Chapter 6.

Regarding the DFD instead, as an important part of the thesis work, an advanced model for the transport of charged particles was developed, for both electrons and ions, in a collisional plasma gas at high temperature and subjected to a magnetic field. This analysis is provided in Chapter 5, whereas proposed applications of the DFD are presented in the respective section of Chapter 6.

The main difference between these two innovative systems lies in the mission objectives and payload requirements, making each technology suitable for different applications. Deep space missions, regardless of the chosen propulsion system, would yield unprecedented scientific discoveries about the outer solar system and the formation of planetary bodies. These innovative propulsion solutions not only shorten mission times but also provide new pathways for future exploration. By addressing the technical challenges of long-distance travel and presenting viable mission scenarios, the study demonstrates the potential for groundbreaking advancements in the exploration of the outer solar system.

The specific aspects developed in this thesis are the use of evaporable materials to increase the thrust in solar sails, the modeling of the transport of charged particles in magnetized plasmas such as those of interest for compact fusion reactors, and the simulation of specific mission scenarios. The methods used for this purpose are based on the kinetic theory of gases and plasma and on flight dynamics, supported by the use of specific mission analysis tools.

The full potential of an innovative simulation method for plasma particle transport can only be fully realized within a comprehensive multiphysics simulation of the propulsion system, which remains beyond the current state of the art. However, the MCF module can be assessed by comparing its results with existing simulation methods used for this specific aspect of plasma physics. Its performance is highly promising, demonstrating significant improvements in both error reduction and computational speed. Since both the DFD thruster and potential auxiliary plasma technologies require plasma simulations in the presence of magnetic fields, this work

represents a major milestone: for the first time, an MCF simulation of a magnetized plasma, specifically in hydrogen and deuterium, has been successfully conducted.

The results obtained, in addition to the first integrated exposure of these two propulsion systems within specific scenarios, are the study of the effect of evaporable material, the development of a high-performance computing program for the simulation of the dynamics of charged particles in magnetized plasmas, the detailed simulation of a scenario for reaching distant targets for future missions, exploring scientifically rich destinations such as the icy moons Enceladus and Europa, the Kuiper Belt region, and the distant trans-Neptunian object Sedna, in the pursuit of uncovering the mysteries of deep space.

Bibliography

[1] S. A. Cohen, C. Swanson, et al. «Direct Fusion Drive for Interstellar Exploration». *JBIS - Journal of the British Interplanetary Society* **72** (2019), pp. 37–50.

[2] G. Genta and R. Y. Kezerashvili. «Achieving the Required Mobility in the Solar System Through Direct Fusion Drive». *Acta Astronautica* **173** (2020), pp. 303–309.

[3] G. Benford and J. Benford. «Acceleration of Sails by Thermal Desorption of Coatings». *Acta Astronautica* **56** (2005), pp. 593–599.

[4] E. Ancona and R. Ya. Kezerashvili. «Extrasolar Space Exploration by a Solar Sail Accelerated via Thermal Desorption of Coating». *Advances in Space Research* **63** (2019), pp. 2021–2034.

[5] E. Ancona, R. Ya. Kezerashvili, and G. L. Matloff. «Exploring the Kuiper Belt with Sun-Diving Solar Sails». *Acta Astronautica* **160** (2019), pp. 601–605.

[6] D. Doody. *Deep Space Craft: An Overview of Interplanetary Flight*. Springer, 2010.

[7] NASA Science. *Solar system exploration: Voyager 2*. (accessed 06.11.24). 2019. URL: `https://science.nasa.gov/mission/voyager/voyager-2/`.

[8] NASA Jet Propulsion Laboratory. *NASA's Voyager 2 Enters Interstellar Space*. (accessed 04.11.24). 2018. URL: `https://www.jpl.nasa.gov/videos/voyager-2-enters-interstellar-space/`.

[9] S. Stern, F. Bagenal, et al. «The Pluto System: Initial Results From Its Exploration by New Horizons». *Science* **350** (2015).

[10] J. Spencer, S. Stern, et al. «The geology and geophysics of Kuiper Belt object (486958) Arrokoth». *Science* **367** (2020).

[11] D. M. Harland. *Mission to Saturn: Cassini and the Huygens probe*. Springer, 2002.

[12] R. T. Mitchell. «Cassini/Huygens at Saturn and Titan». *Acta Astronautica* **59** (2006), pp. 335–343.

[13] S. J. Bolton, A. Adriani, et al. «Jupiter's Interior and Deep Atmosphere: The Initial Pole-to-Pole Passes with the Juno Spacecraft». *Science* **356**.6340 (2017), pp. 821–825.

[14] K.-H. Glassmeier, H. Boehnhardt, et al. «The ROSETTA Mission: Flying Towards the Origin of the Solar System». *Space Science Review* **128**.1-4 (2007), pp. 1–21.

[15] NASA Science. *Rosetta-Philae Mission Overview*. (accessed 04.11.24). Nov. 1, 2024. URL: `https://science.nasa.gov/mission/rosetta-philae/`.

[16] C. Phillips and R. Pappalardo. «Europa Clipper Mission Concept: Exploring Jupiter's Ocean Moon». *Eos, Transactions American Geophysical Union* **95** (2014).

[17] J. Barnes, E. Turtle, et al. «Science Goals and Objectives for the Dragonfly Titan Rotorcraft Relocatable Lander». *The Planetary Science Journal* **2** (2021).

[18] O. Grasset, M. Dougherty, et al. «JUpiter ICy moons Explorer (JUICE): An ESA mission to orbit Ganymede and to characterise the Jupiter system». *Planetary and Space Science* **78** (2013), pp. 1–21.

[19] P. C. Brandt, E. Provornikova, et al. «Interstellar Probe: Humanity's exploration of the Galaxy Begins». *Acta Astronautica* **199** (2022), pp. 364–373.

[20] R. L. McNutt, R. F. Wimmer-Schweingruber, et al. «Interstellar probe – Destination: Universe!» *Acta Astronautica* **196** (2022), pp. 13–28.

[21] A. H. Delsemme. «1999 KUIPER PRIZE LECTURE: Cometary Origin of the Biosphere». *Icarus* **146**.2 (2000), pp. 313–325.

[22] C. de Bergh. «Astrobiology: Future Perspectives». Springer Netherlands, 2005. Chap. Kuiper Belt: Water and Organics, pp. 205–243.

[23] A. M. Shaw. *Astrochemistry: From astronomy to astrobiology*. John Wiley & Sons, 2007.

[24] P. Tsou, D. Brownlee, et al. «LIFE: Life Investigation For Enceladus A Sample Return Mission Concept in Search for Evidence of Life». *Astrobiology* **12** (2012), pp. 730–42.

[25] M. Lingam, A. Hibberd, and A. M. Hein. «A Light Sail Astrobiology Precursor Mission to Enceladus and Europa». *Acta Astronautica* **218** (2023), pp. 251–268.

[26] G. Micca Longo, L. Vialetto, et al. «Plasma Modeling and Prebiotic Chemistry: A Review of the State-of-the-Art and Perspectives». *Molecules* **26**.12 (2021).

[27] S. Worden, C. Bandutunga, et al. «Breakthrough Starshot Program Overview». *Laser Propulsion in Space*. Elsevier, 2024, pp. 39–70.

[28] P. Daukantas. «Breakthrough Starshot». *Optics and Photonics News* **28** (2017), pp. 26–33.

[29] P. Lubin. «A Roadmap to Interstellar Flight». *Journal of the British Interplanetary Society* **69** (2016), pp. 40–72.

[30] G. Matloff and L. Johnson. «Breakthrough Sun Diving: The Rectilinear Option». *JBIS - Journal of the British Interplanetary Society* **76** (2023), pp. 283–287.

[31] Breakthrough Foundation. *Breakthrough Discuss 2024*. (accessed 24.09.24). July 29, 2024. URL: https://breakthroughinitiatives.org/initiative/5.

[32] G. Viavattene and M. Ceriotti. «Artificial Neural Networks for Multiple NEA Rendezvous Missions with Continuous Thrust». *Journal of Spacecraft and Rockets* **59** (2022), pp. 574–586.

[33] ESA. *Artificial intelligence in space*. (accessed 26.09.24). Aug. 3, 2023. URL: https://www.esa.int/Enabling_Support/Preparing_for_the_Future/Discovery_and_Preparation/Artificial_intelligence_in_space.

[34] L. David. *NASA's CAPSTONE is testing "Autopilot" software suite for cislunar operations*. (accessed 24.09.24). July 15, 2024. URL: https://spacenews.com/nasa-capstone-testing-autopilot-software-suite-cislunar-operations/.

[35] B. P. Theiling, L. Chou, et al. «Science Autonomy for Ocean Worlds Astrobiology: A Perspective». *Astrobiology* **22**.8 (2022), pp. 901–913.

[36] A. Pradeepkumar Girija. «A Flagship-class Uranus Orbiter and Probe mission concept using aerocapture». *Acta Astronautica* **202** (2023), pp. 104–118.

[37] K. Hara. «An overview of discharge plasma modeling for Hall effect thrusters». *Plasma Sources Science and Technology* **28**.4 (2019), p. 044001.

[38] I. Kaganovich, A. Smolyakov, et al. «Physics of E× B discharges relevant to plasma propulsion and similar technologies». *Physics of Plasmas* **27**.12 (2020).

[39] I. Levchenko, K. Bazaka, et al. «Space micropropulsion systems for Cubesats and small satellites: From proximate targets to furthermost frontiers». *Physical Review Applied* **5**.1 (2018), p. 011104.

[40] C. Paissoni, N. Viola, et al. «Deep space transportation enhanced by 20 kW-Class Hall Thrusters». *Acta Astronautica* **171** (2020), pp. 83–96.

[41] D. Rafalskyi, J. Martinez, et al. «In-orbit demonstration of an iodine electric propulsion system». *Nature* **599**.7885 (2021), pp. 411–415.

[42] R. Bhatia, J. Cassady, et al. «The Operational Realities of Electric Propulsion». *Proceedings of the 73rd International Astronautical Congress (IAC)*. Paris, France, 2022, Paper IAC–22, C4, 5, 8, x73689.

[43] Y. T. Yoon, P. Ghezzo, et al. «Navigating a large satellite constellation in the new space era: An operational perspective». *Journal of Space Safety Engineering* **10** (2023), pp. 531–537.

[44] K. F. Long. *Deep Space Propulsion - A Roadmap to Interstellar Flight*. Springer, 2012.

[45] M. D. Rayman. «Dawn at Ceres: The First Exploration of the First Dwarf Planet Discovered». *Acta Astronautica* **194** (2022), pp. 334–352.

[46] G. Matloff and H. Gerrish. «Chapter 3 - The scale of the problem: Interstellar distances, time, and energy considerations». *Interstellar Travel*. Ed. by L. Johnson and K. Roy. Elsevier, 2023, pp. 51–82.

[47] P. J. Turchi. «Fusion Propulsion: Field of the Future». *IEEE Transactions on Plasma Science* **51** (2023), pp. 953–964.

[48] K. F. Long. «The Application of Inertial Confinement Fusion Physics to Advanced Spacecraft Propulsion for Deep Space Missions». PhD thesis. University of Warwick, 2023.

[49] L. R. Shepherd. «Interstellar Flight». *Journal of the British Interplanetary Society* **11**.4 (1952), pp. 149–167.

[50] G. H. Miley, X. Yang, and K. A. Flippo. «Inertial Confinement Fusion Propulsion for Deep Space Missions Revisited». *46th AIAA/ASME/SAE Joint Propulsion Conference & Exhibit*. AIAA 2010-6576. AIAA. Nashville, TN, 2010.

[51] K. F. Long. «Interstellar Propulsion using Laser Driven Inertial Confinement Fusion Physics». *Elsevier Universe* **8**.8 (2022), p. 421.

[52] K. F. Long. «Operational Performance Parameter Range in ICF Propulsion Theory». *Acta Astronautica* **210** (2023), pp. 303–310.

[53] R. M. Freeland. «Plasma Dynamics in Firefly's Z-pinch Fusion Engine». *Journal of the British Interplanetary Society* **71** (2018), pp. 288–293.

[54] G. Dyson. *Project ORION: The true story of the atomic spaceship*. Henry Holt and Co., 2002.

[55] C. R. McInnes and M. P. Cartmell. «Orbital Mechanics of Propellantless Propulsion Systems». *Modern Astrodynamics*. Ed. by P. Gurfil. Vol. 1. Elsevier Astrodynamics Series. Butterworth-Heinemann, 2006, pp. 189–235.

[56] J. M. Longuski and S. N. Williams. «Automated Design of Gravity-Assist Trajectories to Mars and the Outer Planets». *Celestial Mechanics and Dynamical Astronomy* **52** (1991), pp. 207–220.

[57] F. Peralta and S. Flanagan. «Cassini Interplanetary Trajectory Design». *Control Engineering Practice* **3** (1995), pp. 1603–1610.

[58] C. R. McInnes. *Solar Sailing: Technology, Dynamics and Mission Applications*. Springer-Praxis, 1999.

[59] R. Zubrin and D. G. Andrews. «Magnetic Sails and Interstellar Travel». *Journal of Spacecraft and Rockets* **28** (1991), pp. 197–203.

[60] R. Zubrin. «The magnetic sail: An advanced Propulsion Concept». *Journal of the British Interplanetary Society* **44** (1991), pp. 31–34.

[61] P. Janhunen. «Electric Sail for Spacecraft Propulsion». *Journal of Propulsion and Power* **20** (2004), pp. 763–764.

[62] P. Janhunen, P. Toivanen, et al. «Electric Solar Wind Sail: Toward Test Missions». *Review of Scientific Instruments* **81** (2010), p. 111301.

[63] G. Marx. «Interstellar Vehicle Propelled by Terrestrial Laser Beam». *Nature* **211** (1966), pp. 22–23.

[64] R. L. Forward. «Photon Sail Spacecraft for Interstellar Flight». *Journal of Spacecraft and Rockets* **21** (1984), pp. 187–195.

[65] G. L. Matloff. «Interstellar Probe Propulsion by Solar-Photon Pressure». *Journal of the British Interplanetary Society* **41** (1988), pp. 163–166.

[66] J. R. Sanmartin, M. Martínez-Sánchez, and E. Ahedo. «Bare Wire Anodes for Electrodynamic Tethers». *Journal of Propulsion and Power* **9** (1993), pp. 353–360.

[67] R. Hoyt and R. L. Forward. «The Terminator Tether: Autonomous Deorbit of LEO Spacecraft for Space Debris Mitigation». *AIAA/USU Conference on Small Satellites*. 2001.

[68] G. A. Landis and D. G. Andrews. «Lorentz-Force Spacecraft Propulsion by Interaction with the Magnetic Field of the Sun». *Acta Astronautica* **60** (2007), pp. 906–913.

[69] R. L. Forward. «Propulsion Using the Interaction of a Moving Magnetic Field and a Stationary Plasma». *Journal of Spacecraft and Rockets* **13** (1976), pp. 282–284.

[70] V. Aslanov, S. Bilén, et al. «Tethers in Space». *Acta Astronautica* **177** (2020), p. 749.

[71] J. Longuski, R. Todd, and W. Koenig. «Survey of Nongravitational Forces and Space Environmental Torques - Applied to the Galileo». *Journal of Guidance Control Dynamics* **15** (1992), pp. 545–553.

[72] B. Fu, E. Sperber, and F. Eke. «Solar Sail Technology—A state of the Art Review». *Progress in Aerospace Sciences* **86** (2016), pp. 1–19.

[73] M. Ceriotti and C. R. McInnes. «Hybrid solar sail and solar electric propulsion for novel Earth observation missions». *Acta Astronautica* **69**.9 (2011), pp. 809–821.

[74] F. A. Tsander. *From a Scientific Heritage: Selected Works of F. A. Tsander*. NASA Technical Translation, 1969.

[75] G. Vulpetti, L. Johnson, and G. L. Matloff. *Solar Sails - A Novel Approach to Interplanetary Travel*. Copernicus Books, 2008.

[76] J. C. Maxwell. «A dynamical theory of the electromagnetic field». *Royal Soc. Trans.* (1865), p. 459.

[77] J. C. Maxwell. *A Treatise on Electricity and Magnetism*. Oxford University Press, Oxford, 1873.

[78] P. N. Lebedev. «First experimental evidence for pressure of the light on the solid bodies». *Annalen der Physik* **6** (1899), pp. 433–458.

[79] R. F. Nichols and G. F. Hull. «Pressure due to radiation». *Physical Review (Series I)* **XVII** (1903), pp. 26–50.

[80] Y. M. Perelman. *Mezhplanetnie puteshestvia - Interplanetary Journeys*. P.P. Soykin, Peterburg, 1915.

[81] K. E. Tsiolkovsky. «Extension of man into outer space». *Proceedings of the Symposium on Jet Propulsion, vol. 2. United Scientific and Technical Presses (NIT)* (1936).

[82] R. L. Garwin. «Solar sailing - a Practical Method of Propulsion Within the solar system». *Jet Propulsion* **28** (1958), pp. 188–190.

[83] Y. Tsuda, O. Mori, et al. «Flight Status of IKAROS Deep Space Solar Sail Demonstrator». *Acta Astronautica* **69** (2011), pp. 833–840.

[84] R. Ya. Kezerashvili. «Solar Sailing: Concepts, Technology, and Missions». *Advances in Space Research* **48** (2011), pp. 1683–1686.

[85] Y. Tsuda, O. Mori, et al. «Achievement of IKAROS — Japanese Deep Space Solar Sail Demonstration Mission». *Acta Astronautica* **82** (2013), pp. 183–188.

[86] L. Johnson, M. Whorton, et al. «NanoSail-D: A Solar Sail Demonstration Mission». *Acta Astronautica* **68** (2011), pp. 571–575.

[87] C. Biddy and T. Svitek. «LightSail-1 Solar Sail Design and Qualification». *Proceedings of the 41st Aerospace Mechanisms Symposium*. Jet Propulsion Laboratory, National Aeronautics and Space Administration, Pasadena, CA, USA, May 16–18, 2012, pp. 451–463.

[88] D. Spencer, B. Betts, et al. «The LightSail 2 Solar Sailing Technology Demonstration». *Advances in Space Research* **67** (2021), pp. 2878–2889.

[89] R. Ya. Kezerashvili and B. Dachwald. «Preface: Solar sailing: Concepts, Technology, and Missions II». *Advances in Space Research* **67** (2021), pp. 2559–2560.

[90] S. Gong and M. Macdonald. «Review on Solar Sail Technology». *Astrodynamics* **3** (2019), pp. 93–125.

[91] P. Zhao, C. Wu, and Y. Li. «Design and Application of Solar Sailing: A Review on Key Technologies». *Chinese Journal of Aeronautics* **36** (2023), pp. 125–144.

[92] Satnews. *Gama's revolutionary propulsion Gama Alpha Solar Sail mission launches*. (accessed 03.11.24). Jan. 4, 2023. URL: https://news.satnews.com/2023/01/04/gamas-revolutionary-propulsion-gama-alpha-solar-sail-mission-launches/.

[93] Spaceref. *Europe's First Solar Sail Mission 'Alpha' Launched*. (accessed 03.11.24). Jan. 6, 2023. URL: https://spaceref.com/newspace-and-tech/europes-first-solar-sail-mission-alpha-launched/.

[94] Sailworld. *Gama launches its Gama Alpha solar sail mission*. (accessed 03.11.24). Jan. 3, 2023. URL: https://www.sail-world.com/news/257330/Gama-launches-its-Gama-Alpha-solar-sail-mission.

[95] W. K. Wilkie. «Overview of the NASA Advanced Composite Solar Sail System (ACS3) Technology Demonstration Project». *AIAA Scitech 2021 Forum*. Vol. 1, Part F. AIAA 2021-1260. American Institute of Aeronautics and Astronautics, 2021.

[96] Satnews. *NASA's ACS3 satellite, Built by NanoAvionics, Successfully Deploys Solar Sail*. (accessed 20.09.24). Sept. 19, 2024. URL: https://news.satnews.com/2024/09/19/nasas-acs3-satellite-built-by-nanoavionics-successfully-deploys-solar-sail/.

[97] O. Eldad and G. Lightsey. «Attitude Control of the Sunjammer Solar Sail Mission». *Proceedings from The Small Satellite Conference*. 2014.

[98] N. Barnes, W. Derbes, et al. «Sunjammer: A Solar Sail Demonstration». Springer, Berlin, Heidelberg, 2014, pp. 115–126.

[99] U. Geppert, B. Biering, et al. «The 3-Step DLR–ESA Gossamer Road to Solar Sailing». *Advances in Space Research* **48** (2011), pp. 1695–1701.

[100] T. Lockett, J. Castillo-Rogez, et al. «Near-Earth Asteroid Scout Flight Mission». *IEEE Aerospace and Electronic Systems Magazine* **35** (2020), pp. 20–29.

[101] J. Pezent, R. Sood, et al. «Preliminary Trajectory Design for NASA's Solar Cruiser: A Technology Demonstration Mission». *Acta Astronautica* **183** (2021), pp. 134–140.

[102] NASA Science. *Solar Cruiser: Enabling New Vistas for Heliophysics Science*. (accessed 01.11.24). 2022. URL: `https://science.nasa.gov/heliophysics/programs/technology/solar-cruiser/`.

[103] L. Johnson, A. Takroori, and L. McNutt. «Solar Sail Propulsion – Ready for Mission Implementation». *Proceedings of 75th International Astronautical Congress (IAC 2024)*. Milan, Italy, 2024, Paper IAC–24, C4, 9, 7, x81466.

[104] M. Leipold, M. Eiden, et al. «Solar Sail Technology Development and Demonstration». *Acta Astronautica* **52** (2003), pp. 317–326.

[105] D. Spencer, L. Johnson, and A. Long. «Solar sailing technology challenges». *Aerospace Science and Technology* **93** (2019), p. 105276.

[106] C. Bianchi, L. Niccolai, et al. «Preliminary Design of a Space Debris Removal Mission in LEO using a Solar Sail». *Advances in Space Research* **73** (2024), pp. 4254–4268.

[107] L. Arnouts, M. Killian, et al. «ADEO – Aerodynamic Deorbit System for Satellites». *Proceedings of 75th International Astronautical Congress (IAC 2024)*. Milan, Italy, 2024, Paper IAC–24, A6, 5, 10, x86837.

[108] W. Seboldt and B. Dachwald. «Solar Sails for near-term advanced scientific deep space missions». *Proceedings of the 8th International Workshop on Combustion and Propulsion, Italy, 16-21 June, Paper 49, Pozzuoli (Ed.)* (2002).

[109] J. Benford and G. Benford. «Flight of Microwave Driven Sails: Experiments and Applications». *AIP Conference Proceedings* **664** (2003), pp. 303–312.

[110] H. Ulbricht, R. Zacharia, et al. «Thermal desorption of gases and solvents from graphite and carbon nanotube surfaces». *Carbon* **44** (2006), pp. 2931–2942.

[111] P. A. Redhead. «Thermal desorption of gases». *Vacuum* **12** (1962), pp. 203–211.

[112] J. L. Beeby. «A Theory of desorption and surface processes - I. General formulation». *Surface Science* **114** (1982), pp. 118–136.

[113] K. A. Fichthorn and R. A. Miron. «Thermal desorption of large molecules from solid surfaces». *Physical Review Letters* **89**.19 (2002), p. 196103.

[114] S. Holloway, P. Jewsbury, and J. L. Beeby. «Theoretical analysis of desorption from surfaces». *Surface Science* **63** (1977), pp. 339–347.

[115] A. Redondo, Y. Zeiri, and W. A. Goddard. «Rates of Desorption from solid surfaces: coverage dependence». *Surface Science* **136** (1984), pp. 41–58.

[116] G. Benford and P. Nissenson. «Reducing solar sail escape times from Earth orbit using beamed energy». *Acta Astronautica* **58** (2006), pp. 175–184.

[117] R. Ya. Kezerashvili. «Space Exploration with a Solar Sail Coated by Materials that Undergo Thermal Desorption». *Acta Astronautica* **117** (2015), pp. 231–237.

[118] R. L. Forward. «Starwisp: An Ultra-Light Interstellar Probe». *J. Spacecraft* **22** (1985), p. 345.

[119] R. L. Forward. «Roundtrip Interstellar Travel Using Laser Pushed Light Sails». *Journal of Spacecraft and Rockets* **21** (1984), pp. 187–195.

[120] R. Y. Kezerashvili. «Thickness requirement for solar sail foils». *Acta Astronautica* **65** (2009), pp. 507–518.

[121] H. Ulbricht, G. Moos, and T. Hertel. «Interaction of C60 with Carbon Nanotubes and Graphite». *Physical Review Letters* **90**.9 (2003), pp. 095501–4.

[122] R. Zacharia, H. Ulbricht, and T. Hertel. «The Interlayer Cohesive Energy of Graphite from Thermal Desorption of Polyaromatic Hydrocarbons». *Physical Review B* **69** (2004).

[123] M. Oba, H. Mita, and A. Shimoyama. «Determination of activation energy and pre-exponential factor for individual compounds on release from kerogen by a laboratory heating experiment». *Geochemical Journal* **36** (2002), pp. 51–60.

[124] M. Yu, Z. Li, et al. «Desorption activation energy of dibenzothiophene on the activated carbons modified by different metal salt solutions». *Chemical Engineering Journal* **132** (2007), pp. 233–239.

[125] E. Ancona and R. Ya. Kezerashvili. «Temperature Restrictions for Materials used in Aerospace Industry for the Near-Sun Orbits». *Acta Astronautica* **140** (2017), pp. 565–569.

[126] S. D'Auria. *Introduction to Nuclear and Particle Physics*. Springer, 2018.

[127] J. Freidberg. *Plasma Physics and Fusion Energy*. Cambridge University Press, 2007.

[128] F. Elio, Fr. Elio, et al. «Technical Report: The Polomac Approach to Fusion Energy». *The Journal of Technological and Space Plasmas* (2024), pp. 172–180.

[129] R. Kennedy. «The interstellar fusion fuel resource base of our solar system». *Journal of the British Interplanetary Society* **71** (2018), pp. 298–305.

[130] T. Simko and M. Gray. «Lunar Helium-3 Fuel for Nuclear Fusion: Technology, Economics, and Resources». *World Future Review* **6** (July 2014), pp. 158–171.

[131] S. Cohen and A. Glasser. «Ion Heating in the Field-Reversed Configuration by Rotating Magnetic Fields near the Ion-Cyclotron Resonance». *Physical Review Letters* **85** (2000), pp. 5114–5117.

[132] S. Cohen and R. Milroy. «Maintaining the Closed Magnetic-Field-Line topology of a Field-Reversed Configuration with the Addition of Static Transverse Magnetic Fields». *Physics of Plasmas* **7** (2000), pp. 2539–2545.

[133] W. J. E. Jr. «Principles of Nuclear Rocket Propulsion». Butterworth-Heinemann, 2023.

[134] W. Commons. *Field Reversed Configuration (FRC)*. (accessed 08.11.24). Sept. 21, 2020. URL: `https://commons.wikimedia.org/wiki/File:Field-Reversed_Configuration.svg`.

[135] A. Galia. «A Dynamic Homogenization Method for Nuclear Reactor Core Calculations. Modeling and Simulation». PhD thesis. Université Paris-Saclay, 2020.

[136] M. Rosenbluth and M. Bussac. «MHD Stability of Spheromak». *Nuclear Fusion* **19** (1979), p. 489.

[137] Y. Jain and P. D. Kakade. «Analyzing the Engineering Feasibility of the Direct Fusion Drive». *Acta Astronautica* **206** (2023), pp. 57–71.

[138] M. Gajeri, P. Aime, and R. Ya. Kezerashvili. «A Titan Mission Using the Direct Fusion Drive». *Acta Astronautica* **180** (2021), pp. 429–438.

[139] P. Aime, M. Gajeri, and R. Ya. Kezerashvili. «Exploration of Trans-Neptunian Objects Using the Direct Fusion Drive». *Acta Astronautica* **178** (2021), pp. 257–264.

[140] R. Ya. Kezerashvili. «Exploration of the Solar System and Beyond Using a Thermonuclear Fusion Drive». *GLEX-2021,6,1,5,x62072, The Global Space Exploration Conference 2021*. St. Petersburg, Russian Federation, June 14–18, 2021.

[141] F. F. Chen and J. P. Chang. *Lecture Notes on Principles of Plasma Processing*. New York: Springer Science & Business Media, 2012.

[142] F. F. Chen. *Introduction to Plasma Physics and Controlled Fusion*. Vol. 1. New York: Plenum Press, 1984, pp. 19–51.

[143] L. P. Pitaevskii and E. M. Lifshitz. *Physical Kinetics: Volume 10*. Butterworth-Heinemann, 2012.

[144] R. Hemsworth, D. Boilson, et al. «Overview of the design of the ITER heating neutral beam injectors». *New Journal of Physics* **19**.2 (2017), p. 025005.

[145] D. Tereshonok, T. Chernyshev, et al. «Two-term Boltzmann approximation versus Monte-Carlo simulation: effect of magnetic field». *Physica Scripta* **99**.6 (2024), p. 065603.

[146] T. Dias, C. Pintassilgo, and V. Guerra. «Effect of the magnetic field on the electron kinetics under AC/DC electric fields: benchmark calculations and electron cyclotron resonance». *Plasma Sources Science and Technology* **32** (2023).

[147] M. Rondanini, C. Cavallotti, et al. «An experimental and theoretical investigation of a magnetically confined DC plasma discharge». *Journal of Applied Physics* **104** (2008).

[148] H.-Y. Wang, P. Sun, et al. «Implicit electrostatic Particle-In-Cell/Monte Carlo simulation for the magnetized plasma: Algorithms and application in gas-inductive breakdown». *Chinese Physics B* **24** (2015).

[149] R. Barni, S. Caldirola, et al. «Tomography of a simply magnetized toroidal plasma». *Plasma Science and Technology* **20** (2018), p. 025102.

[150] D. Eremin, D. Engel, et al. «Electron dynamics in planar radio frequency magnetron plasmas: I. The mechanism of Hall heating and the μ-mode». *Plasma Sources Science and Technology* **32**.4 (2023), p. 045007.

[151] T. Tsankov, P. Chabert, and U. Czarnetzki. «Foundations of magnetized radio-frequency discharges». *Plasma Sources Science and Technology* **31**.8 (2022), p. 084007.

[152] V. Toigo, S. Dal Bello, et al. «Progress in the ITER neutral beam test facility». *Nuclear fusion* **59**.8 (2019), p. 086058.

[153] M. Capitelli, M. Cacciatore, et al. «Vibrational kinetics, electron dynamics and elementary processes in H_2 and D_2 plasmas for negative ion production: modelling aspects». *Nuclear fusion* **46**.6 (2006), p. 260.

[154] G. Serianni, V. Toigo, et al. «First operation in SPIDER and the path to complete MITICA». *Review of Scientific Instruments* **91**.2 (2020), p. 023510.

[155] C. Hopf, G. Starnella, et al. «Neutral beam injection for fusion reactors: technological constraints versus functional requirements». *Nuclear fusion* **61**.10 (2021), p. 106032.

[156] F. Cichocki, P. Innocente, et al. «Kinetic modeling of the plasma–wall interaction in the DTT divertor region». *Plasma Physics and Controlled Fusion* **66**.2 (2024), p. 025015.

[157] S. Longo, P. Diomede, and M. Capitelli. «Multispecies particle simulation of the hydrogen plasma sheath region». *Contributions to Plasma Physics* **46**.7 (2006), pp. 763–768.

[158] B. Lipschultz, X. Bonnin, et al. «Plasma–surface interaction, scrape-off layer and divertor physics: implications for ITER». *Nuclear fusion* **47**.9 (2007), p. 1189.

[159] R. Churchill, J. Canik, et al. «Kinetic simulations of scrape-off layer physics in the DIII-D tokamak». *Nucl. Mater. Energy* **12** (2017). Proceedings of the 22nd International Conference on Plasma Surface Interactions 2016, 22nd PSI, pp. 978–983.

[160] R. Gabrielli and G. Herdrich. «Review of Nuclear Thermal Propulsion Systems». *Prog. Aerosp. Sci.* **79** (2015), pp. 92–113.

[161] J. Gudmundsson. «Physics and Technology of Magnetron Sputtering Discharges». *Plasma Sources Science and Technology* **29**.11 (2020), p. 113001.

[162] T. Makabe and Z. Petrović. *Plasma electronics: applications in microelectronic device fabrication*. CRC Press, 2014.

[163] S. Dujko, Z. M. Raspopović, and Z. L. Petrović. «Monte Carlo studies of electron transport in crossed electric and magnetic fields in CF_4». *Journal of Physics D: Applied Physics* **38**.16 (2005), p. 2952.

[164] S. Longo. «Monte Carlo models of electron and ion transport in non-equilibrium plasmas». *Plasma Sources Science and Technology* **9**.4 (2000), pp. 468–476.

[165] T. Dias, A. Tejero-del-Caz, et al. «The LisbOn KInetics Monte Carlo solver». *Computer Physics Communications* **282** (2023), p. 108554.

[166] C. K. Birdsall and A. B. Langdon. *Plasma physics via computer simulation*. CRC Press, 2018.

[167] T. Tajima. *Computational plasma physics: with applications to fusion and astrophysics*. CRC Press, 2018.

[168] Z. Donkó, A. Derzsi, et al. «eduPIC: an introductory particle based code for radio-frequency plasma simulation». *Plasma Sources Science and Technology* **30**.9 (2021), p. 095017.

[169] G. Hagelaar and L. Pitchford. «Solving the Boltzmann equation to obtain electron transport coefficients and rate coefficients for fluid models». *Plasma Sources Science and Technology* **14** (2005), pp. 722–733.

[170] A. Tejero-del-Caz, V. Guerra, et al. «The LisbOn KInetics Boltzmann solver». *Plasma Sources Science and Technology* **28**.043001 (2019).

[171] J. Stephens. «A multi-term Boltzmann equation benchmark of electron-argon cross-sections for use in low temperature plasma models». *Journal of Physics D: Applied Physics* **51**.12 (2018), p. 125203.

[172] D. Loffhagen, R. Winkler, and Z. Donkó. «Boltzmann Equation and Monte Carlo Analysis of the Spatiotemporal Electron Relaxation in Nonisothermal Plasmas». *The European Physical Journal Applied Physics* **18**.3 (2002), pp. 189–200.

[173] N. Dyatko, I. Kochetov, et al. «EEDF: The software package for calculations of Electron Energy Distribution Function». *Availabel online: https://fr. lxcat. net/download/EEDF (accessed on 1 February 2024)* (2015).

[174] S. Dujko, R. D. White, et al. «A multi-term solution of the nonconservative Boltzmann equation for the analysis of temporal and spatial non-local effects in charged-particle swarms in electric and magnetic fields». *Plasma Sources Science and Technology* **20**.024013 (2011).

[175] J. Lynch, T. Sippel, and S. Subramaniam. «An efficient solution of the multi-term multi-harmonic electron Boltzmann equation for use in global models». *Computer Physics Communications* **299** (2024), p. 109156.

[176] R. White, R. Robson, et al. «Is the classical two-term approximation of electron kinetic theory satisfactory for swarms and plasmas?» *Journal of Physics D: Applied Physics* **36**.24 (2003), pp. 3125–3131.

[177] R. Pawula. «Approximation of the linear Boltzmann equation by the Fokker-Planck equation». *Physical Review* **162**.1 (1967), p. 186.

[178] G. Schaefer and P. Hui. «The Monte Carlo flux method». *Journal of Computational Physics* **89**.1 (1990), pp. 1–30.

[179] L. Vialetto, S. Longo, and P. Diomede. «Benchmark calculations for electron velocity distribution function obtained with Monte Carlo Flux simulations». *Plasma Sources Science and Technology* **28**.11 (2019), p. 115015.

[180] L. Vialetto, P. Viegas, et al. «Benchmarking of Monte Carlo Flux simulations of electrons in CO_2». *Plasma Sources Science and Technology* **29**.11 (2020), p. 115006.

[181] L. Vialetto, H. Sugawara, and S. Longo. «Particle Propagation and Electron Transport in Gases». *Plasma* **7**.1 (2024), pp. 121–145.

[182] G. I. Bell and S. Glasstone. *Nuclear Reactor Theory*. Van Nostrand Reinhold Company, 1970.

[183] A. Hébert. *Applied Reactor Physics*. Presses Internationales Polytechnique, 2009.

[184] P. Viegas, L. Vialetto, et al. «Insight into contraction dynamics of microwave plasmas for CO_2 conversion from plasma chemistry modelling». *Plasma Sources Science and Technology* **29**.10 (2020), p. 105014.

[185] P. Viegas, L. Vialetto, et al. «Resolving discharge parameters from atomic oxygen emission». *Plasma Sources Science and Technology* **30**.6 (2021), p. 065022.

[186] L. Vialetto, A. van de Steeg, et al. «Charged particle kinetics and gas heating in CO_2 microwave plasma contraction: comparisons of simulations and experiments». *Plasma Sources Science and Technology* **31**.5 (2022), p. 055005.

[187] N. G. Van Kampen. *Stochastic processes in physics and chemistry*. Vol. 1. Elsevier, 1992.

[188] R. Robson. *Introductory Transport Theory for Charged Particles in Gases*. World Scientific Publishing Company, 2006.

[189] A. M. Howatson. *An introduction to gas discharges: Pergamon international library of science, technology, engineering and social studies*. Elsevier, 2013.

[190] J. Boris and R. Shanny. *Proceedings of The 4th Conference on Numerical Simulation of Plasmas*. Naval Research Laboratory, 1972.

[191] C. M. Ferreira and J. Loureiro. «Electron kinetics in atomic and molecular plasmas». *Plasma Sources Science and Technology* **9**.4 (2000), p. 528.

[192] Biagi database. www.lxcat.net, last access September 15, 2024.

[193] P. Diomede, M. Sanden, and S. Longo. «Insight into CO_2 Dissociation in Plasma from Numerical Solution of a Vibrational Diffusion Equation». *The Journal of Physical Chemistry C* **121**.36 (2017), pp. 19568–19576.

[194] R. Chandra, H. Blank, P. Diomede, et al. «B2.5-Eunomia simulations of Magnum-PSI detachment experiments: I. Quantitative comparisons with experimental measurements». *Plasma Physics and Controlled Fusion* **63** (2021).

[195] P. Ricci, B. Rogers, and S. Brunner. «High-and low-confinement modes in simple magnetized toroidal plasmas». *Physical Review Letters* **100**.22 (2008), p. 225002.

[196] A. Phelps. «Cross Sections and Swarm Coefficients for H^+, H_2^+, H_3^+, H, H_2, and H^- in H_2 for Energies from 0.1 eV to 10 keV». *The Journal of Physical and Chemical Reference Data* **19**.3 (1990), pp. 653–675.

[197] T. Šimko. «Modélisation du transport ionique et électronique dans un gaz soumis à un champ électrique. Comparaison modèle-expérience pour l'hydrogène». PhD thesis. Université de Paris-Sud, 1997.

[198] J. Trieschmann, L. Vialetto, and T. Gergs. «Machine learning for advancing low-temperature plasma modeling and simulation». *Journal of Micro / Nanopatterning, Materials, and Metrology* **22**.4 (2023), pp. 041504–041504.

[199] B. A. Conway. *Spacecraft Trajectory Optimization*. Cambridge University Press, 2010.

[200] Ieva, S., Dotto, E., et al. «Low delta-V near-Earth asteroids: A survey of suitable targets for space missions». *Astronomy & Astrophysics* **569** (2014), A59.

[201] A. Peloni and M. Ceriotti. «Solar-Sail Trajectory Design for a Multiple Near-Earth-Asteroid Rendezvous Mission». *Journal of Guidance, Control, and Dynamics* **39** (2016).

[202] E. Ancona, R. Ya. Kezerashvili, and S. Longo. «Feasibility Study of a Mission to Sedna - Nuclear Propulsion and Advanced Solar Sailing Concepts». *Proceedings of 75th International Astronautical Congress (IAC 2024)*. Milan, Italy, 2024, Paper IAC–24, C4, 9, 6, x85994.

[203] G. Genta and P. Maffione. «IRMA: a Graphical Tool for Interplanetary Mission Design». *MATEC Web of Conferences* **210** (Jan. 2018), p. 02049.

[204] R. P. Russell and M. Lara. «On the design of an Enceladus science orbit». *Acta Astronautica* **65**.1 (2009), pp. 27–39.

[205] F. Salazar, A. Alkhaja, et al. «Science orbits in the Saturn–Enceladus circular restricted three-body problem with oblate primaries». *Acta Astronautica* **180** (2021), pp. 398–416.

[206] V. Zubko, A. Sukhanov, et al. «Analysis of Mission Opportunities to Sedna in 2029–2034». *Advances in Space Research* **68** (2021), pp. 2752–2775.

[207] V. Zubko, A. Sukhanov, et al. «Analysis of Optimal Flight Trajectories to the Trans-Neptunian Object (90377) Sedna». *Astronomy Letters* **47** (2021), p. 188.

[208] V. Zubko. «The Fastest Routes of Approach to Dwarf Planet Sedna for Study its Surface and Composition at the Close Range». *Acta Astronautica* **192** (2022), pp. 47–67.

[209] V. Ya. Kezerashvili, R. Ya. Kezerashvili, and O. Starinova. «Solar Sail with Inflatable Toroidal Shell». *Acta Astronautica* **202** (2023), pp. 17–25.

[210] R. Ya. Kezerashvili, O. L. Starinova, et al. «A Torus-Shaped Solar Sail Accelerated Via Thermal Desorption of Coating». *Advances in Space Research* **67** (2021), pp. 2577–2588.

[211] N. JPL. *NASA Horizons System Web App - ephemeris download*. (accessed 08.11.24). URL: `https://ssd.jpl.nasa.gov/horizons/app.html#/`.